
Mechanical and structural characterization of composite plates: from beams to TPMS

Auteur : Le, Maureen

Promoteur(s) : Ruffoni, Davide

Faculté : Faculté des Sciences appliquées

Diplôme : Master en ingénieur civil biomédical, à finalité spécialisée

Année académique : 2023-2024

URI/URL : <http://hdl.handle.net/2268.2/20868>

Avertissement à l'attention des usagers :

Tous les documents placés en accès ouvert sur le site le site MatheO sont protégés par le droit d'auteur. Conformément aux principes énoncés par la "Budapest Open Access Initiative"(BOAI, 2002), l'utilisateur du site peut lire, télécharger, copier, transmettre, imprimer, chercher ou faire un lien vers le texte intégral de ces documents, les disséquer pour les indexer, s'en servir de données pour un logiciel, ou s'en servir à toute autre fin légale (ou prévue par la réglementation relative au droit d'auteur). Toute utilisation du document à des fins commerciales est strictement interdite.

Par ailleurs, l'utilisateur s'engage à respecter les droits moraux de l'auteur, principalement le droit à l'intégrité de l'oeuvre et le droit de paternité et ce dans toute utilisation que l'utilisateur entreprend. Ainsi, à titre d'exemple, lorsqu'il reproduira un document par extrait ou dans son intégralité, l'utilisateur citera de manière complète les sources telles que mentionnées ci-dessus. Toute utilisation non explicitement autorisée ci-avant (telle que par exemple, la modification du document ou son résumé) nécessite l'autorisation préalable et expresse des auteurs ou de leurs ayants droit.

UNIVERSITY OF LIÈGE
FACULTY OF APPLIED SCIENCES

Mechanical and structural characterization of composite plates: from beams to TPMS

Master Thesis conducted by

MAUREEN LÊ

with the aim of obtaining the degree of Master in Biomedical Engineering

SUPERVISORS:

Davide RUFFONI
Pasquale VENA

PhD STUDENTS SUPERVISORS:

Quentin GROSSMAN
Luca D'ANDREA

ACADEMIC YEAR 2023-2024

Abstract

Advanced engineering demands materials that are stronger, tougher, and lighter, exceeding the capabilities of conventional materials. This has led to the exploration of innovative design approaches, particularly through the use of cellular solids. These materials achieve a desirable balance of strength and lightness through intricate lattice designs composed of solid struts forming the edges or faces of individual cells. Lattice structure, a prominent subset of cellular solids, feature repeating and interconnected structures which can be inspired by the strategic porosity found in biological materials. This engineered porosity significantly enhances their mechanical properties. A key application of lattice structure, relevant to this research, is in tissue engineering scaffolds, where open-cell lattice structures promote cell infiltration and migration, crucial for effective tissue regeneration.

The advancement of additive manufacturing techniques, such as PolyJet 3D printing, has enabled the creation of architected materials. These materials integrate individual constituents with varying mechanical properties at the mesoscale into spatial arrangements optimized for mechanical performance. Drawing inspiration from the evolutionary design principles found in biological tissue, these architected structures often exhibit superior properties compared to their individual components.

In this study, we utilize multimaterial PolyJet 3D printing to fabricate cellular solids with beams featuring a hybrid sandwich-like design to enhance mechanical efficiency and, more specifically, energy absorption. We investigate the flexural behavior of these struts in two configurations: core-shell (C-S) and core-interface-shell (C-I-S), using 3-point bending tests combined with Digital Image Correlation (DIC). The core is composed of a rubbery material (Shore95, Young's modulus ~ 100 [MPa]), while the faces are made from a rigid glassy material (VeroWhitePlus, Young's modulus ~ 2 [GPa]), and the interface are made of a softer material (TangoBlackPlus, Young's modulus ~ 1 [MPa]). Additionally, we examine how the printing orientation influences the behavior of the composites due to differences in the interface connecting two materials: when printed horizontally bimaterial interfaces are sharp (i.e. less than $20\text{ }\mu\text{m}$ in width), whereas printed vertically, internal interfaces are rather blurred (i.e. around $150\text{ }\mu\text{m}$ in width).

Our findings indicate a 30% increase in energy absorption for small core-to-strut thickness ratios compared to monolithic beams. Different core-to-strut thickness ratios result in varying failure modes, including complete brittle failure or delamination. The addition of an interface slightly decreases performance, except at an intermediate ratio of $c/t = 0.2$, where blurred interfaces reduce delamination and enhance flexural strength. For thicker soft layers, a blurred interface achieved by vertical printing is advantageous, while for thinner layers, a sharp interface achieved by horizontal printing is preferable.

The study further explores the energy absorption capacity of 3D-printed triply periodic minimal surface (TPMS) gyroid lattices with composite cell walls, designed based on results of the first part of the thesis, under in-plane compression. Results reveal that the composite TPMS gyroid retains the performance characteristics of its individual stiff material but also demonstrates improved deformation recovery compared to the individual stiff constituent.

Acknowledgments

Completing this master's thesis has been a challenging and rewarding journey, made possible through the support and guidance of many individuals. Immersing myself in the world of research has been an invaluable experience, filled with challenges, joy, stress, and excitement. I have been fortunate to share these moments with remarkable individuals, to whom I owe a deep debt of gratitude. I extend my heartfelt thanks to all who have contributed to this achievement.

Firstly, I would like to express my profound gratitude to my supervisor, Professor Davide Ruffoni, for providing me with the opportunity to work on such an intriguing project in his laboratory. His unwavering support, insightful guidance, and encouragement have been immensely motivating throughout the course of this thesis. His expertise and dedication have been instrumental in the successful completion of this research. I also extend my thanks to my co-supervisor in Milan, Professor Pasquale Vena, for his time and support and for giving me the chance to collaborate with him and the University of Politecnico di Milano. His expert advice and constructive feedback were invaluable, and I am grateful for the project I undertook in his laboratory, which contributed to the understanding of my thesis.

I am deeply grateful to Quentin Grossman for his unwavering support throughout the entirety of this thesis. His invaluable assistance during the experiments, analysis of results, and the writing process has been indispensable. Quentin's willingness to assist, prompt problem-solving abilities, and profound expertise in my subject matter, as well as the printing and testing machinery, were invaluable to this thesis and provided me with inestimable learning experiences. Furthermore, I would like to extend my sincere thanks to Luca d'Andrea for his significant contributions to my project in Milan. His expert advice and assistance with the TPMS structure part of my research have been incredibly helpful and are greatly appreciated.

I am also grateful to the members of my jury for dedicating their time to thoroughly review this thesis and participate in my defense.

Lastly, I am deeply thankful to my family, without whom I would not have reached this milestone. Their steadfast support throughout this thesis and my academic journey has been incredibly meaningful. They have stood by me through both the challenges and successes, offering remarkable moral support, and I am profoundly thankful for their belief in me.

I also wish to express my appreciation to my friends for their support during challenging times and for the moments of relaxation and companionship that provided much-needed breaks. Your presence has truly made these years more meaningful.

Contents

Introduction	1
1 Background	2
1.1 Recent advances in lattice materials	2
1.2 Challenges in achieving balanced mechanical properties	4
1.3 Inspiration from natural materials	5
1.4 Architected multi-materials	6
1.5 Multi-material additive manufacturing	8
1.5.1 Stratasys PolyJet printer	9
1.6 Application in tissue engineering scaffolds	12
1.6.1 Bone scaffolds	13
1.6.2 Materials used in bone scaffolds	13
1.6.3 Additive Manufacturing	13
1.6.4 Application of TPMS scaffolds	14
1.7 Aim of the thesis	16
2 Single Rectangular Beam Structure	17
2.1 Methods and Materials	17
2.1.1 Materials	17
2.1.2 Sample design and dimensions	19
2.1.3 Sample 3D printing	21
2.1.4 Sample testing: 3 point bending test	22
2.1.5 Digital Image Correlation (DIC)	25
2.2 Results and Discussion	31
2.2.1 Statistical variability between samples	31
2.2.2 Core-Shell configuration	31
2.2.3 Core-Shell configuration vs Core-Interface-Shell configuration	35
2.2.4 Printing orientation	44
2.3 Conclusion	49
2.3.1 Limitations	51
2.3.2 Perspective	52
3 Triply Periodic Minimal Surface Structure	53
3.1 Methods and Materials	53
3.1.1 Materials	53
3.1.2 Methods	53
3.2 Results and Discussion	58
3.3 Conclusion	61
3.3.1 Limitations	61
3.3.2 Perspective	62
Appendix	67

3.4	Load-Displacement curves of samples printed horizontally (along xy)	67
3.4.1	VeroWhite and Shore95	67
3.4.2	Core-Shell configuration	67
3.5	Core - Interface - Shell configuration	68
3.6	Stress-strain curves of samples printed vertically (along xz)	69
3.6.1	VeroWhite and Shore95	69
3.6.2	Core-Shell configuration	70
3.7	Load-Displacement curves with point where DIC was performed	71
3.8	MatLab Code for TPMS generation	71
Bibliography		78

Introduction

Since many years, there has been a significant push towards developing structures and materials with exceptional properties and enhanced mechanical performance. This drive has stimulated advancements in various fields, particularly in the realm of cellular solids. These structures exhibit hybrid characteristics that balance flexibility, hardness, and lightweight design principles, making them increasingly attractive for diverse applications.

Among cellular solids, lattice structures stand out due to their periodic arrangement of interconnected cells, drawing inspiration from natural tissues. This category of structures holds particular promise for improving bone scaffolds, crucial for effective integration within the human body. The challenge lies in optimizing these structures to achieve a delicate balance between strength and flexibility, essential for biomedical applications.

Recent studies have laid the groundwork for exploring architectural materials, a novel class facilitated by advances in additive manufacturing. These materials represent a paradigm shift in material design, offering intricate geometries and tailored mechanical properties.

This thesis investigates the mechanical performance of multi-layered structures featuring a soft core and a hard shell, arranged in a sandwich configuration inspired by natural bone structure. Utilizing PolyJet multi-material printing, these multi-material lattices were developed to allow mechanical tuning by varying the core-to-strut thickness ratio. The flexural behavior was assessed through three-point bending tests to evaluate their mechanical performance. The study also explores the impact of incorporating a soft interface within these structures, which has been shown to enhance energy absorption. Additionally, it examines how different printing orientations affect the behavior of these multi-layered struts, considering the influence of printing direction on the interface.

The research extends to the study of Triply Periodic Minimal Surface (TPMS) cellular solids, integrating the multi-layered lattices created using additive manufacturing. These complex structures have potential applications in biomedical engineering, particularly as scaffolds for bone regeneration and tissue engineering.

In summary, this thesis aims to advance the field of architected materials by investigating the ability to tune their mechanical properties, specifically their energy absorption capacity, through the adjustment of constituent characteristics. The ultimate goal is to advance research in various applications, including those in biomedicine.

Chapter 1

Background

1.1 Recent advances in lattice materials

Advanced engineering demands materials that are not only stronger and tougher but also lighter. Yet, conventional materials fall short in pushing the boundaries of existing material properties. Stepping into the realm of material innovation, cellular solids emerge as captivating hybrid high-performance structures, balancing strength and lightness through their intricate designs. As shown in Figure 1.1, cellular structures can be classified based on the arrangement of their unit cells (periodic or non-periodic) and their morphology (open-cell or closed-cell). Their design comprises a network of solid struts that interconnect to form the edges or faces of individual cells [1].

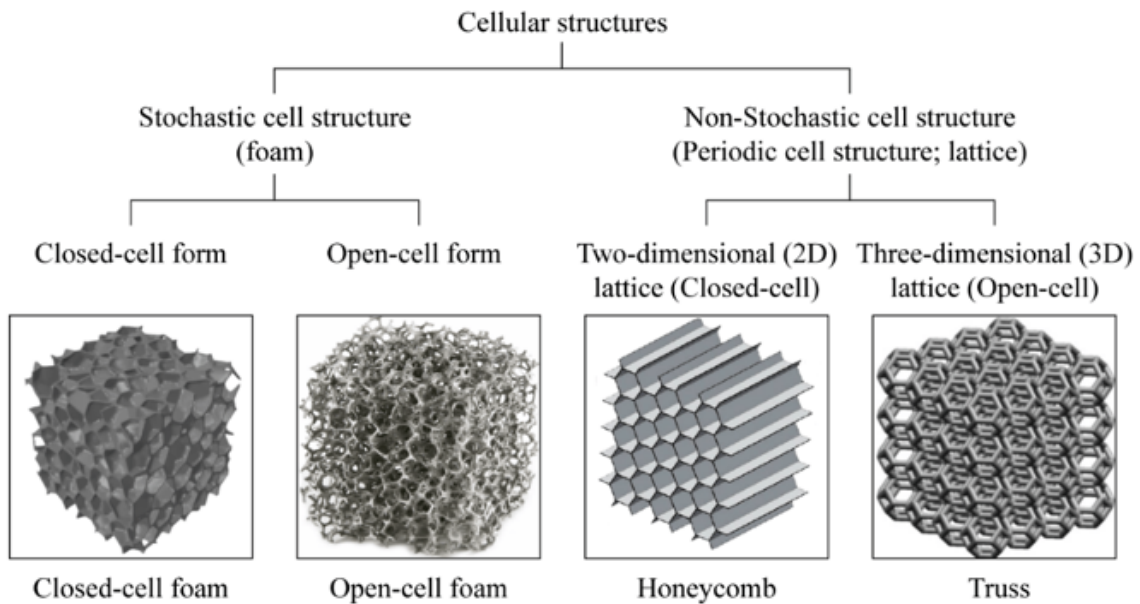


Figure 1.1 – The different types of cellular structures. [2]

These structures manifest both in natural phenomena and engineered creations. Examples of cellular solids in nature encompass wood, sponge, and trabecular bone. Conversely, engineered varieties, such as honeycombs and foams, are crafted from a diverse array of materials including polymers, metals, ceramics. Those cellular structures are illustrated in Figures 1.2 and 1.3.

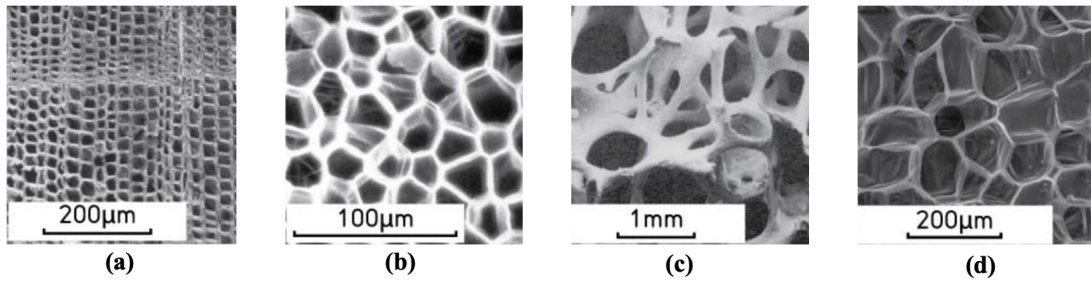


Figure 1.2 – Cellular solids in nature: (a) Wood; (b) Sponge; (c) Trabecular bone; (d) Carrot. [1]

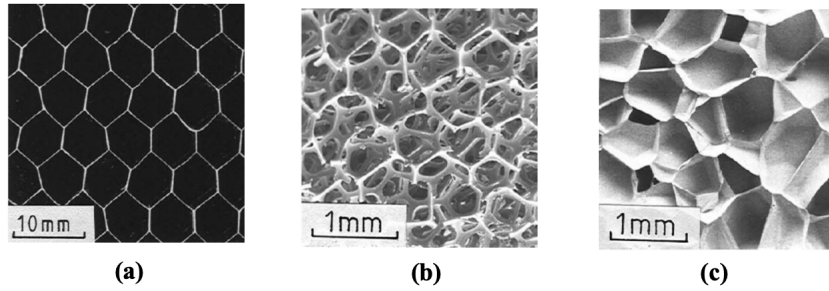


Figure 1.3 – Engineered cellular solids: (a) Honeycomb; (b) Open-cell foam; (c) Closed-cell foam. [1]

Thanks to their cellular architecture, they are attributed remarkable properties including lightweight, a high strength-to-weight ratio, elevated stiffness, exceptional permeability, and energy absorption capabilities. These properties find application across diverse fields shown in Figure 1.4, such as sandwich panel cores, benefiting from their lightweight nature [3], energy absorption devices like helmets and automobile bumpers, leveraging their superior impact-absorbing capabilities [4], as well as in thermal and acoustic insulation [1]. Furthermore, their potential extends to the aerospace industry, where they hold promise for revolutionizing systems and capabilities [5].

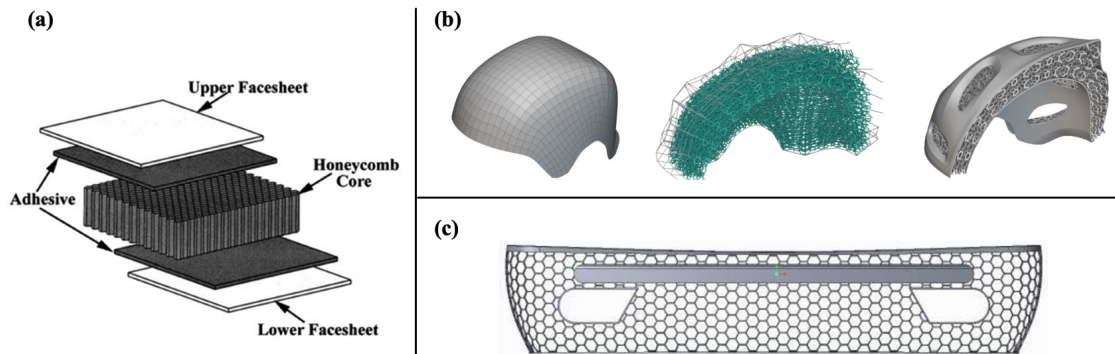


Figure 1.4 – Applications of cellular solids: (a) Sandwich panel core [6]; (b) High-performance energy absorption helmet [7] and (c) Automobile bumper based on honeycomb structure [8].

Lattice materials represent a specialized category within cellular engineered materials, characterized by their repeating and interconnected lattice structure. These materials are meticulously crafted with a focus on arranging and shaping interconnected struts or beams, resulting in a lightweight yet mechanically resilient material. In broad terms, we define lattice materials as cellular, reticulated, truss, or lattice structures composed of numerous uniform lattice elements, such as slender beams or rods. These structures are generated by tessellating a unit cell—comprising only a few lattice elements—in a periodic or random way throughout space to form a cellular network. Examples of lattices structures from their unit cell to the cellular network are illustrated in Figure 1.5. Various forms of lattice structures exist, including honeycombs, woodpiles and octet trusses [9].

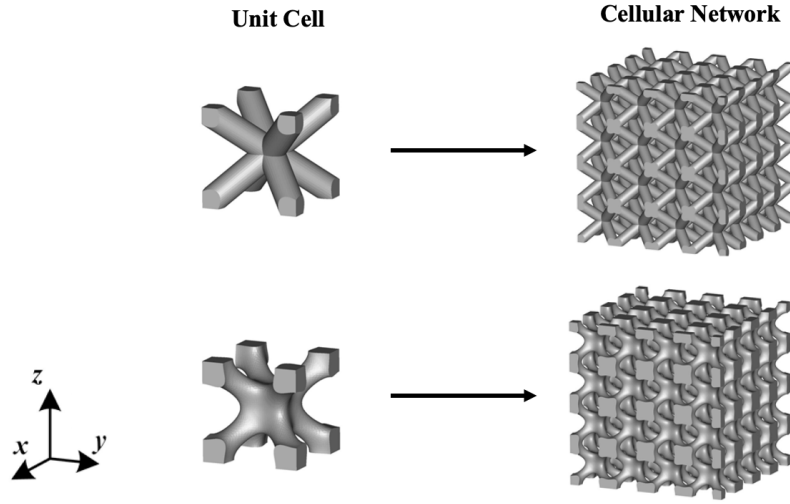


Figure 1.5 – Examples of lattice structures from unit cell to cellular network[10]

The concept of lattice materials draws inspiration from biological materials, where the distribution of porosity is strategically engineered to enhance mechanical properties. The traditional dense counterparts of lattice solids typically cannot match the exceptional properties and attributes conferred by their customized porosity. While lattice materials have been subject to extensive study over the past decade, recent advancements in additive manufacturing techniques have propelled them into the spotlight. One compelling application of lattice materials, particularly relevant to this thesis, is their use in tissue engineering scaffolds. Porous scaffolds utilized in tissue engineering essentially embody an open-cell lattice structure, wherein interconnected porosity plays a pivotal role in facilitating cell infiltration and migration through the scaffold [1].

1.2 Challenges in achieving balanced mechanical properties

One of today's primary objectives, and indeed a significant challenge, lies in continually enhancing the microstructure and mechanical properties of bone scaffolds and lattice cellular structures across various applications. Despite the remarkable properties exhibited by cellular materials and recent advancements in lightweight material design and fabrication [11, 12, 13], achieving architectures that combine high stiffness and toughness remains a challenging objective. These properties are often mutually exclusive, which complicates their simultaneous attainment [14].

Stiffness refers to a material's resistance to deformation, measuring the force needed to stretch or bend the material. On the other hand, toughness denotes a material's capacity to absorb energy prior to failure, indicating the extent of deformation it can endure before fracturing. It's important to note that a material may exhibit stiffness without toughness, as seen in glass, or toughness without stiffness, as exemplified by rubber [15, 16]. These concepts are closely linked to ductility and brittleness. Ductility refers to a material's ability to deform without fracturing, contributing to toughness by allowing significant energy absorption before failure. Conversely, brittleness denotes a material's tendency to fracture under stress without much plastic deformation. Brittle materials are typically stiff, exhibiting high Young's modulus values, which amplifies their propensity to fracture abruptly.

Numerous efforts have been made to develop lattice materials aiming for superior specific strength and toughness [11, 17]. These lattices have predominantly been constructed using either solid or hollow struts, composed of a singular material phase such as polymers, metals, or ceramics. The mechanical performance of these lattice materials has varied, with some emphasizing high strength or stiffness, while others prioritize ductility or energy absorption. For instance, ceramic-based lattices have demonstrated exceptional stiffness and strength but limited ductility due to their inherently brittle nature [11], whereas polymeric lattices have shown remarkable ductility but comparatively lower strength [17]. Hence, the persistent obstacle involves attaining a harmonious blend of varied mechanical characteristics within single-phase lattice materials.

1.3 Inspiration from natural materials

In recent years, scientists and engineers have tried to overcome this limitation by imitating nature. Drawing inspiration from nature, researchers seek to create architected structures boasting exceptional mechanical characteristics. Mimicking nature's design principles allows for the development of composites that exhibit remarkable strength, toughness, and resilience, paving the way for innovative solutions in various fields of engineering and materials science. Over millions of years of evolution, biological tissue structures have adapted to diverse and challenging environments exhibiting remarkable resilience to shock and damage, as well as a simultaneous enhancement of strength and toughness [18].

For example, Y. Wei and his colleagues [19] drew inspiration from sponges, which exhibit a microscale layered structure alternating between soft and hard materials, enhancing toughness. At the macroscale, these fibers are arranged in a cross-network configuration, providing high specific strength. They introduced a novel multi-bionic mechanical metamaterial that combines the bone structure's concentric circle microstructure—enhancing the balance between energy absorption and toughness—with a face-centered cubic (FCC) arrangement of metal atoms, which increases specific strength. The design strategy is illustrated below in Figure 1.6. By incorporating bionic microstructures into lattice structures, they effectively mitigated catastrophic fractures. This innovative approach not only enhances the strength of the lattice structure but also endows it with exceptional energy absorption capabilities.

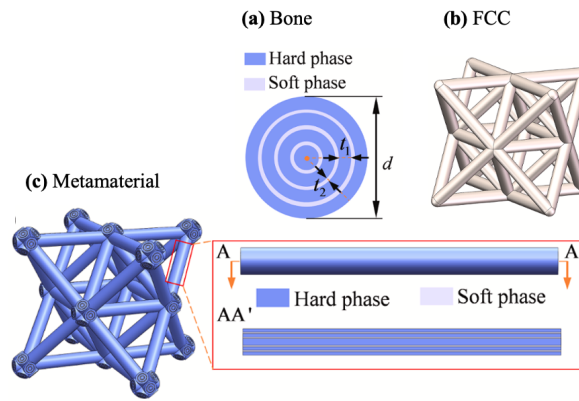


Figure 1.6 – Design strategy for the multi-bionic metamaterial: (a) Concentric circle pattern inspired by bone structure; (b) FCC lattice arrangement; (c) Metamaterial featuring concentric rods alternating between soft and hard materials [19].

Among the other biological structures, bone and nacre structures, illustrated in Figure 1.7 stand out as exemplary natural materials [20] that seamlessly combine strength with toughness, rendering them exceptionally damage tolerant. They overcome the challenge of simultaneously possessing high strength and toughness thanks to their combination of stiff and soft components within hierarchical architectures. To enhance their resistance to failure, their toughening mechanisms primarily leverage microstructural features to impede crack formation and propagation by controlling the unraveling of the soft phase during fracture [21].

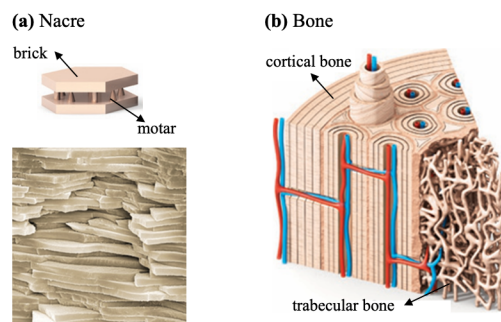


Figure 1.7 – (a) Nacre and (b) Bone structure[24].

Nacre, the inner layer of shells, serves as an exceptional model for combining high strength and toughness in a lightweight manner. Its brick-and-mortar architecture features a high fracture toughness, achieved by deflecting cracks around rigid aragonite 'bricks' while bridging them with thin, compliant organic 'mortar'[22]. Chen et al.[23] provide a remarkable demonstration of effective biomimetic design by fabricating a composite paper composed of graphene oxide (GO) and sodium alginate (SA) building blocks, mirroring the hybrid structure of natural nacre. By enhancing the hydrogen bond formation between these materials, they achieved an optimal blend of high strength and toughness, surpassing the properties of natural nacre and similar composites. However, implementing such mechanisms into lattice architectures presents challenges, as constructing complex struts proves to be difficult [24].

The significant enhancement in toughness observed in bone is primarily attributed to its structural organization and characteristic fracture mechanisms at each hierarchical level. Bones comprise two main components: cortical bone, forming the dense outer layer, and trabecular bone, composing the inner spongy structure. This arrangement resembles a sandwich panel geometry, with cortical bone serving as the tough outer layer and trabecular bone providing internal support. Together, they offer an exceptional combination of strength and toughness. The denser and stiffer cortical bone provides structural support and shields the bone from fractures. In contrast, trabecular bone, with its porous and interconnected network of struts, enhances the bone's ability to absorb energy and resist fractures, thus augmenting its toughness. Crucial mechanisms, such as crack deflection, occur within the Haversian structure, characteristic of the microstructural level of cortical bone. Osteons, owing to their geometry and distinct properties from the matrix, promote stress delocalization, reducing local stresses at crack tips and providing crack shielding. Additionally, osteon outer boundaries, known as cement lines, are rich in microcracks, facilitating further energy dissipation[25]. Research has shown that energy dissipation resulting from bone heterogeneity yields biomechanical properties markedly different from those of uniform materials [26]. This phenomenon is common among various biological tissues and may serve as a design principle for biologically inspired composites utilizing multi-material technology.

1.4 Architected multi-materials

Architected cellular materials, drawing inspiration from natural structures, are meticulously engineered to exhibit desired mechanical properties through careful manipulation of their cellular architecture. In contrast to naturally existing cellular materials, the ones referred to as architected cellular materials are purposefully engineered to optimize properties such as stiffness, strength, and energy absorption. For example, Z. Hu et al. [27] developed methods to design and predict the performance of cellular structures in order to create ultralight and strong composites. Drawing inspiration from biomimicry, they introduced topological designs such as a 2D hexagonal honeycomb model and a 2D cuttlefish model. The results demonstrate that the 2D cuttlefish model exhibits higher planar stiffness, particularly in the vertical direction, thanks to the cuttlefish's evolutionary adaptations for withstanding high pressures in the open ocean.

In this thesis, a distinctive approach is adopted, inspired by biological marvels such as bone and nacre. This methodology involves the fusion of soft and hard constituents to create what we term "micro-architected multi-material structures," featuring a blend of two or more material phases within a singular microstructure having attributes not offered by either one alone.

Y. Wei et al. [19] proposition of a multi-bionic strategy, merging the FCC wire mesh's lightweight, high-specific strength with the bones' osteoid concentric structure's exceptional toughness is one example of micro-architected material. Their multi-bionic mechanical metamaterial combined soft and hard materials, showcasing multi-stage deformation and remarkable toughness in two-phase materials. For instance, a metamaterial with a 20% soft phase ratio could absorb 3.8 times more energy than its pure hard phase counterpart. Further simulations demonstrated that incorporating a soft phase layer significantly enhances metamaterial toughness by restraining crack propagation.

Two other studies, conducted by Mueller et al. and Yavas et al., which will serve as inspiration for this thesis, investigated the behavior of multi-material structures configured with a soft core and a hard shell.

Specifically, they studied the influence of different ratios between the core and the shell on the mechanical properties.

Mueller et al. [28] manufactured orthotropic lattices with flexible epoxy core and brittle epoxy shell patterns, with (C-S) or without an elastomeric silicone interfacial layer (C-I-S), using a multicore-shell 3D printing technique illustrated in Figure 1.8.

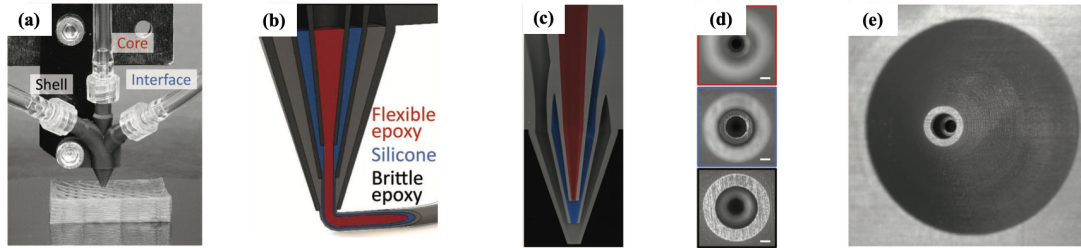


Figure 1.8 – a) Coaxial printhead with core, interface, and shell ink reservoirs. b) Cross-sectional view of the C-S printhead. c) False-colored image of the C-S nozzle showing coextruded inks (core: red, interface: blue, shell: gray). d,e) End-on views of C-S nozzles with high-resolution retracted inner channels.[28]

The cracking behavior of some Mueller's samples during testing is illustrated in Figure 1.9. It was observed that pure brittle epoxy samples ($d/D = 0$) failed completely under applied loading. In contrast, Core-Shell (C-S) samples exhibited different failure characteristics. The interface between the core (C) and the shell (S) was proposed to act as a diffusion zone, facilitating a continuous transition of mechanical properties. This transition could potentially decelerate or halt crack propagation while still allowing stress to be efficiently transferred from the shell to the core.

The introduction of the interface aimed to reduce the overall stiffness and provide structural stability. Post-test observations revealed that the flexible epoxy core remained intact, and two distinct patterns of cracking in the shell were noted. For a lower inner diameter-to-beam diameter ratio ($d/D = 0.4$), cracks in the brittle shell propagated in a straight line. Conversely, at a higher ratio of 0.85, the cracks exhibited deflection and bifurcation, resulting in a piecewise failure of the shell. This behavior created multiple new surfaces and effectively doubled the energy absorption capacity of the shell.

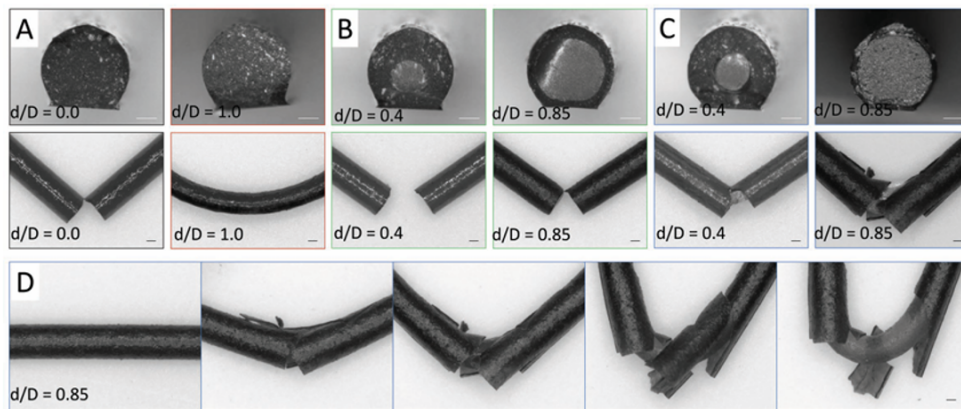


Figure 1.9 – Cracking behaviour of a) pure materials of shell and core beams, b) C-S beams, c) C-I-S beams and d) Sequence of crack propagation of C-I-S beam with increasing strain from left to right [28]

Yavas et al.'s study [29] introduced an extrusion-based 3D printing method to produce multi-material architected lattices with adjustable mechanical properties, such as stiffness and strength. Drawing inspiration from bone structures, the approach integrated flexible thermoplastic polymers in the core and rigid materials in the shell. Leveraging 3D printing technology with fusion of multi-material filaments enabled the fabrication of these structures. Figure 1.10 shows an overview of his work. The lattice truss elements adopted a sandwich configuration, with the shell providing rigidity and the core offering strength and energy absorption. This innovative design facilitated mechanical property tuning by varying the thickness ratio between

the core and the strut. Through 3-point bending tests, the bending behavior of these struts with different thickness ratios was examined.

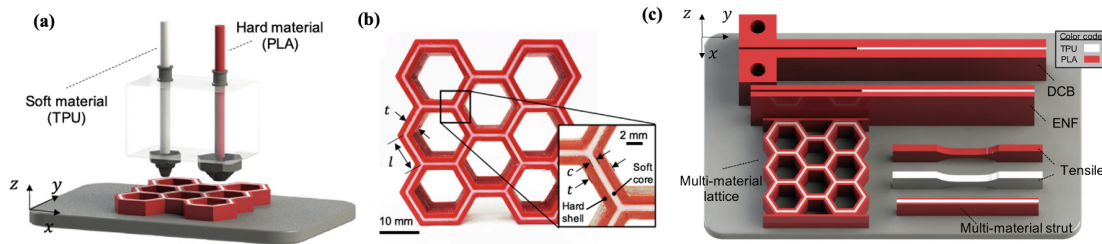


Figure 1.10 – a) 3D schematic of multi-material FFF honeycomb printing. b) FFF-printed honeycomb lattice ($c/t = 1/3$) showing cell wall details. c) Schematics showing sample orientation relative to the printing bed.[29]

Yavas's study reveals that the mechanical properties of multi-material struts, composed of TPU cores and PLA shells, decline as the core-to-strut thickness ratio increases, as illustrated in Figure 1.11. Analytical models tend to overestimate the flexural modulus. Up to a core-to-strut ratio of 0.2, these struts exhibit higher energy absorption compared to their individual components, with performance improvements linked to stronger PLA-TPU interface adhesion. Stronger interfaces lead to better flexural strength and strain energy density, while weaker interfaces result in earlier failure.

For multi-material lattices, similar trends are observed: varying the core-to-strut thickness adjusts the in-plane compression modulus and strength, echoing the flexural behavior of the struts. Enhanced adhesion between PLA and TPU significantly improves these properties. Multi-material lattices demonstrate approximately 2–3 times greater energy absorption than their individual materials, with a failure mode that allows for multiple stress peaks (shown in Figure 1.12), further increasing energy absorption during deformation.

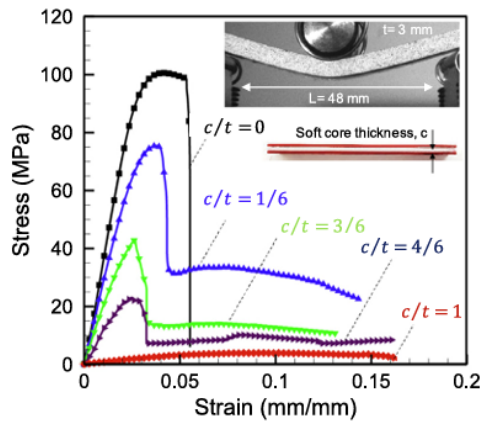


Figure 1.11 – Flexural stress–strain curves of multi-layer strut with varying core-to-strut thickness ratios [29].

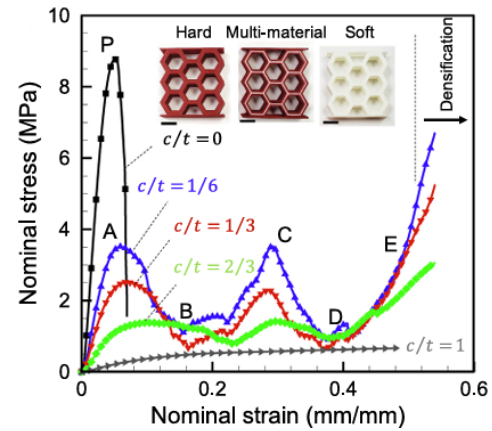


Figure 1.12 – Nominal stress–strain curves of the multi-material honeycomb lattices with different c/t ratios [29].

1.5 Multi-material additive manufacturing

Additive manufacturing, often referred to as 3D printing, is a technique used to fabricate diverse structures and intricate geometries based on three-dimensional model data. This innovative process entails the deposition of successive layers of materials, gradually building up the desired object. With its evolution over the years, 3D printing has become synonymous with versatility, offering a spectrum of methods, materials, and equipment tailored to various applications. The profound impact of additive manufacturing extends across multiple industries, revolutionizing manufacturing and logistics processes, from the construction sector to prototyping and biomechanics[31].

For instance, the company CERHUM, located in the scientific park of Sart-Tilman, utilizes 3D printing to

produce technical ceramics for medical applications, showcasing its potential in healthcare. On the other hand, Aerosint, based in Herstal, employs Selective Powder Deposition to craft multi-material prototypes in metal, demonstrating the versatility and adaptability of additive manufacturing in creating complex structures.

Additive manufacturing has undergone rapid development over recent decades to fulfill diverse functionality, complexity, and accuracy requirements. One notable advancement within this realm is multi-material additive manufacturing (MM-AM), which enables the simultaneous printing of multiple materials[32]. This capability represents a significant leap forward by transitioning from single-material products to multi-material components, promising innovation. Leveraging the advantages inherent in 3D printing—such as material and resource efficiency, production flexibility, and reduced lead times—MM-AM facilitates the creation of components with complex geometries and added functionalities. The key driver behind MM-AM processes is the incorporation of region-specific functionalities, allowing for the placement of diverse materials in user-defined locations to yield high-performance systems. This approach enables the construction of composite structures with graded or separate regions of differing materials in a single, continuous step using a single machine. As a result, composite parts can seamlessly progress from the design stage to the final product, streamlining the manufacturing process and unlocking new possibilities in product design and functionality [33].

1.5.1 Stratasys PolyJet printer

The PolyJet process, pioneered by Stratasys Ltd., stands out as a leading commercially available multi-material jetting technique [35]. Originally patented by Objet Geometries in the late 1990s, PolyJet is the proprietary name, while Material Jetting denotes its technical process[34].

Mechanism

PolyJet process is based on one of the pioneering and enduring technologies within MM-AM: material jetting, commonly known as inkjet 3D printing. This method facilitates seamless switching between multiple materials, including support material for overhanging features, utilizing jetting nozzles within the print head. The printer typically includes at least two print heads: one for jetting the material for the model and another for the support. In Figure 1.13, a schematic representation illustrates the process. Photosensitive polymer resin is extruded from a print head onto a surface and subsequently cured via UV light as the print head traverses along the x-direction. Meanwhile, rollers smooth out the deposited material, removing surplus material and achieving consistent layer thickness to prepare the surface for the next layer. Following a back-and-forth motion at the same y-coordinate, the print head shifts to the y-direction, systematically printing the succeeding portion of the ongoing layer until completion. Upon completion of a layer, the print tray descends by the height of one layer, initiating the repetition of the entire process for the subsequent layer[36]. This process allows for the formation of one layer at a time and is repeated until the desired height of the part is achieved. By enabling drops to be ejected on demand, this method ensures high resolution and, consequently, geometric accuracy [32]. It is also the only technology allowing for full color and multi-materials 3D printing simultaneously thanks to the multiple print heads [34].

Stratasys PolyJet technology offers remarkable precision, making it one of the most accurate 3D printing methods available, achieving resolutions of up to 16 microns and delivering exceptionally smooth finishes. However, compared to Fused Deposition Modeling (FDM), known for its affordability and accessibility, PolyJet is generally more expensive and industrial grade. Parts produced with PolyJet may exhibit lower strength over time compared to FDM-printed parts, which maintain their structural integrity. Despite these drawbacks, PolyJet excels in speed, material selection, color options, and scalability, making it a preferred choice for certain applications. While, PolyJet's solid supports result in higher material consumption, contributing to its overall cost, which can be significant, it minimizes warping or shrinkage during printing due to the absence of extreme heating, further enhancing its reputation for precision and superior surface finishes among 3D printing technologies [34].

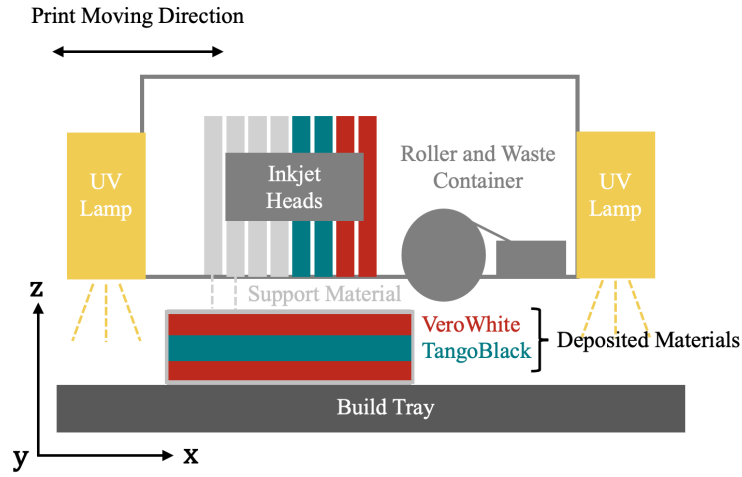


Figure 1.13 – Schematic of PolyJet printing process [37].

Specifications

The relevant specifications for this study include the printer's resolution across the different axes during multimaterial printing. This parameter is delineated by the printer as the Digital Material mode, dictating the resolution levels which are the following [35] :

$$\begin{aligned} x : 600 \text{ dpi} &= 42.5\mu\text{m} \\ y : 300 \text{ dpi} &= 85\mu\text{m} \\ z : 800 \text{ dpi} &= 31.875\mu\text{m} \end{aligned}$$

Materials

PolyJet printers utilize a singular category of material known as photopolymers. These polymers exhibit properties that undergo alteration upon exposure to light, a process known as photopolymerization illustrated in Figure 1.14. Initially in liquid form, these materials are deposited and subsequently cured through UV light exposure, a technique commonly referred to as UV curing. This curing process transforms the liquid resin into a solid state. Typically, ultraviolet (UV) rays serve as the light source in 3D printing, initiating reactions that reshape the structure of the photopolymer, thereby altering its chemical and mechanical characteristics.

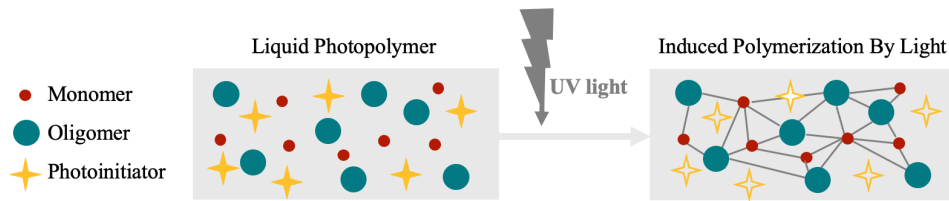


Figure 1.14 – Schematic of photopolymerization process induced by UV light.

The materials employed in PolyJet printing, termed Digital Materials, involve the deposition of up to seven distinct resins simultaneously, resulting in the creation of precisely engineered materials.

The support material used in this study is SUP705 proposed by Stratasys [35], an acrylic compound stored in a liquid state, exhibiting a yellowish hue. This support material can be easily removed, either manually by hand or through the utilization of a waterjet.

VeroWhitePlus (VW+) belongs to the Vero family of materials proposed by Stratasys and is characterized by its rigid, white polymer composition once printed. Table 1.1 provides pertinent details regarding this

material. In this study, VW+ will be employed and is regarded as the most rigid material among the printed samples utilized.[38]

TangoBlackPlus (TB+), also known as FLX980, belongs to the TangoTM family of materials proposed by Stratasys and is characterized by its elastomeric properties, rendering it like rubber. Once printed, TB+ manifests as a soft black polymer. Table 1.1 contains essential information regarding TangoBlackPlus properties. In this study, TB+ will be used and identified as the softest material among the printed samples.[39]

	VeroWhite +	TangoBlack +
Tensile Strength [MPa]	50-65	0.8-1.5
Elongation at break [%]	10-25	170-120
Shore hardness	83-86 (Scalde D)	26-28 (Scale A)
Modulus of elasticity [GPa]	2-3	0.001

Table 1.1 – Mechanical properties of VW + and TB +.

The Stratasys printer provides the distinctive capability to combine these two fundamental materials, enabling the production of twelve unique digital materials, each pre-configured by the manufacturer.

Printing orientation influence on multi-material interface

In the context of printing multi-layer digital materials with both compliant and stiff components, two distinct printing methods have been explored for constructing the sample layer by layer.

Laura Zorzetto's research [68] examined the impact of printing methods on the interfaces between compliant (TB+) and stiff (VW+) digital materials in multi-layer structures. Two printing scenarios were analyzed: one in which droplets of photopolymers mixed and formed an interface before curing, applicable to horizontally printed samples, and another in which mixing occurred after curing, relevant to vertically printed samples. The PolyJet printing process for bimaterial samples produced in either horizontal or vertical orientations is shown in Figure 1.15.

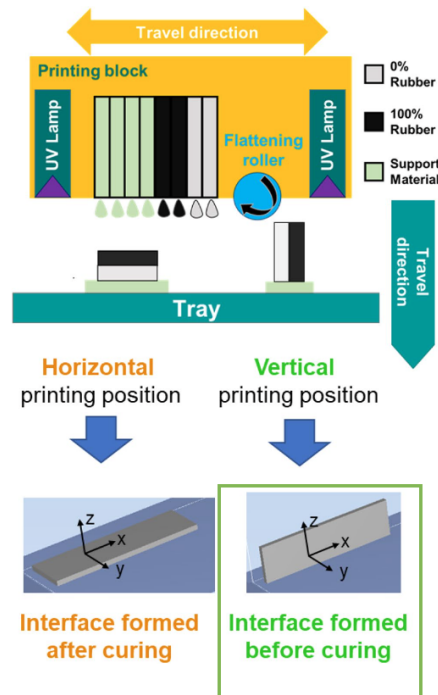


Figure 1.15 – Diagram illustrating the PolyJet printing process for bimaterial samples produced in either horizontal or vertical orientations. These two printing methods result in the bimaterial interface being created either before or after UV curing.

Nanoindentation revealed that interfaces formed after curing exhibited sharp transitions with minimal mixing between TB+ and VW+, with interface thicknesses smaller than 20 μm . Optical microscopy supported these findings, showing a sharp separation between the two materials with little blending. Results of the nanoindentation are illustrated in Figure 1.16.

In contrast, interfaces formed before curing showed a much broader transition, spanning approximately 120–140 μm , indicating significant inter-diffusion of the materials. This broader transition was attributed to the leveling of droplets and potential diffusion of chemical components before curing.

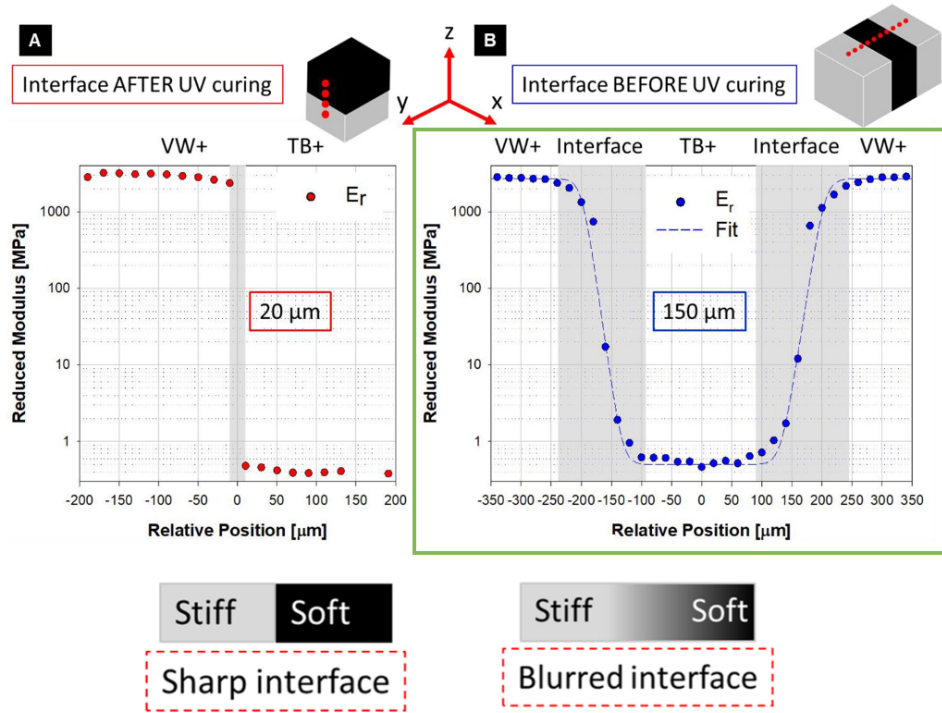


Figure 1.16 – Results from nanoindentation showing spatial variations in reduced elastic modulus across bimaterial interfaces. The data is presented for interfaces formed (A) after UV curing and (B) before UV curing.

The study also used finite element simulations to investigate how these interface characteristics affect the mechanical behavior of composites. It was found that interfaces influence shear mechanisms and load transfer in multilayer composites with alternating stiff and compliant layers.

1.6 Application in tissue engineering scaffolds

As previously stated, the primary objective of this thesis is to investigate the behavior of architected multi-material lattice structures to enhance the mechanical performance of bone scaffolds. Porous materials are essential in various regenerative medicine procedures due to their ability to create a suitable environment for cell attachment and colonization through their unique architecture. By analyzing these lattice structures, the goal is to enhance their ability to minimize the risk of scaffold fractures.

The effectiveness of lattice structures as bone scaffolds has been showed by several studies. Among them, Melchels et al. [45] investigated the impact of scaffold pore architecture on cell seeding and static culturing. Their research revealed that gyroid-type lattice structures have more than 10 times the permeability of salt leaching architectures due to their interconnected pores. This higher permeability facilitates homogeneous cell distribution and enhances cell seedability. Additionally, scaffolds coated with hydroxyapatite, which chemically and structurally resembles the mineral phase of natural bone, exhibit improved biological activity and can induce spontaneous bone formation [46].

1.6.1 Bone scaffolds

With global life expectancy on the rise and an aging population, there is an increasing incidence of orthopedic-related fractures and conditions such as osteoporosis, low-back pain, subchondral defects, and bone tumors. As a result, bone has become the second most commonly transplanted tissue worldwide. The complexity of treatment escalates with critical-sized or extensive bone defects caused by infections, malignancies, or trauma, necessitating robust and structurally sound interventions. While autografts from bones like the fibula, iliac crest, and ribs are adequate for small bone defects, larger voids pose significant challenges. These challenges drive extensive research in bone tissue engineering (BTE), which aims to develop innovative biomimetic scaffolds as alternatives to traditional bone grafts [47].

A bone scaffold functions as a three-dimensional framework that supports the attachment and proliferation of osteoinducible cells on its surfaces. To design effective bone scaffolds, the materials must be biocompatible, exhibit structural and mechanical properties similar to the bone they are intended to replace—particularly in terms of Young’s modulus—and retain biological activities that promote tissue ingrowth and optimal osseointegration [48]. Matching the scaffold’s stiffness to that of natural bone encourages tissue growth and prevents stress shielding, which can hinder bone formation if the scaffold is too rigid compared to the surrounding bone [49]. Given their lightweight and porous nature, lattice structures effectively meet these critical tissue engineering requirements.

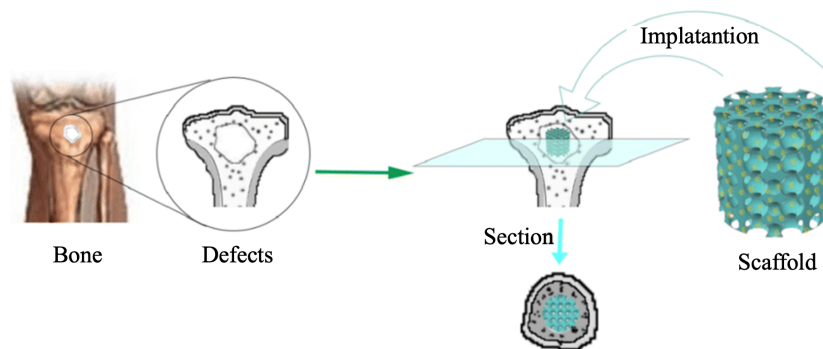


Figure 1.17 – Bone scaffolds use.

1.6.2 Materials used in bone scaffolds

The base materials used for bone tissue scaffolds include ceramics, metals, and polymers [50]. These materials must be non-toxic to cells and provide a surface conducive to cell attachment and proliferation. Ceramics and polymers typically have elastic moduli closer to that of trabecular bone, especially when adjusted for lattice porosity, whereas titanium’s elastic modulus is significantly higher. Among ceramics, hydroxyapatite (HAP) is notable for its mechanical properties comparable to natural bone, its similarity to bone mineral constituents, and its ability to promote osseointegration and biocompatibility [49].

Studies on using multi-materials for bone scaffolds have been introduced recently. For example, bioactive composite materials have been proposed by Wang and his colleagues [51] to leverage the benefits of multiple material types, such as metallic, ceramic, and polymeric components. However, the mechanical reinforcement of these composite scaffolds has yet to fully meet the demands of bone tissue in vivo [48].

1.6.3 Additive Manufacturing

Additive Manufacturing (AM) provides remarkable flexibility in creating lattice structures for tissue engineering. It allows for the implementation of complex unit cell designs and duplication patterns, producing high-precision lattice structures. This technology also addresses the critical concerns of biocompatibility and biodegradability in tissue engineering by offering a diverse selection of materials across different AM methods. Various 3D printing techniques, including extrusion, resin, and powder-based technologies, are employed to fabricate lattices. Each method brings distinct advantages in terms of feature detail and resolution, and can utilize a variety of materials. The resolution capabilities of these printing processes are

influenced by the materials used and their layer-by-layer construction approach, ensuring tailored and effective solutions for tissue engineering needs [49].

1.6.4 Application of TPMS scaffolds

Triply periodic minimal surfaces (TPMS) have attracted significant attention in recent years due to their exceptional attributes, including smooth surfaces, highly interconnected porous structures, and precisely controllable geometric features. The applications of TPMS span multiple disciplines [52], such as satellite technology, aerospace engineering, and electric vehicle design. More recently, TPMS has begun to be explored for use in bone tissue engineering [53].

The rising interest in TPMS for these applications can be attributed to its structural similarity to trabecular bone, particularly in terms of tortuosity, meaning porous network[54]. Additionally, TPMS structures are lightweight, which minimizes material usage, reduces costs, and shortens the degradation time of scaffolds in vivo. This combination of properties underscores the potential of TPMS as a transformative solution in various high-tech and biomedical fields. Bone regeneration, vascularization, and material absorption are also proven to be accelerated by the interconnectivity of pores [55] [56]. TPMS scaffolds provide sufficient mechanical strength to support bone formation while also replicating the characteristics of biological bone tissue. This ensures seamless integration with surrounding tissues and enhances cellular processes such as oxygen diffusion, ion exchange, and nutrient transport [53].

Triply periodic minimal surfaces have been a subject of differential geometry research for over 250 years. One of the early pioneers in this field was Lagrange, who proposed the existence of a minimal area surface bounded by a closed curve [57]. This implies that TPMS have zero mean curvature, meaning the sum of the principal curvatures at each point on the surface is zero. When a thickness is applied to these surfaces, they form unit cells with cubic symmetry. The periodic repetition of these unit cells in three independent directions creates a porous structure with interconnected pores. This entire geometry can be described through algebraic equations, simplified as $f(x, y, z) = C$, where C is a constant. Consequently, TPMS can also be referred to as isosurfaces. The algebraic formula for different types of TPMS are included in Figure 1.18 below. TPMS are particularly suitable for scaffold design due to their periodic implicit surface with zero mean curvature. The properties of these surfaces, such as porosity and volume-specific surface areas, can be directly controlled by adjusting the parameters of the defining function [52].

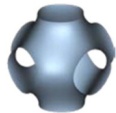
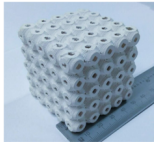

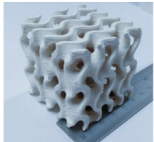
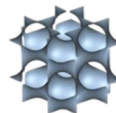
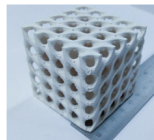
Name	Algebraic formula	3D unit cell	Printed TPMS model
P Primitive	$f(x, y, z) = \cos(\omega_x x) + \cos(\omega_y y) + \cos(\omega_z z) = C$		
G Gyroid	$f(x, y, z) = \sin(\omega_x x) \cos(\omega_y y) + \sin(\omega_z z) \cos(\omega_x x) + \sin(\omega_y y) \cos(\omega_z z) = C$		
D Diamond	$f(x, y, z) = \cos(\omega_x x) \cos(\omega_y y) \cos(\omega_z z) - \sin(\omega_x x) \sin(\omega_y y) \sin(\omega_z z) = C$		

Figure 1.18 – Equations, unit cells and models of TPMS-based structures. [52]

Using TPMS structures to create cellular materials offers a significant advantage over traditional truss/strut-based lattice structures, which are composed of struts and nodes [58]. One of the primary issues with

truss/strut structures is the stress concentrations that occur at the connections of the lattice struts, often leading to imperfections at these joints. These imperfections can cause the structure to collapse under lower applied loads.[59] For instance, Khaderi et al. [60] found that imperfections in Gyroid-lattice structures significantly degrade their elastic and plastic properties.

In contrast, TPMS structures are characterized by continuous surfaces with smooth joints, which result in fewer stress concentrations and superior mechanical properties. This smooth connectivity not only enhances the overall integrity of the structure but also improves cell adhesion and proliferation, promoting increased bone tissue ingrowth.[61] Unlike truss/strut-based cellular materials, TPMS cellular materials (TPMS-CMs) lack joints and struts, allowing for a smoother transfer of loads and better structural integrity. [59] This makes TPMS-CMs a more reliable option for applications requiring robust and efficient load distribution.

Several types of TPMS are known, but Gyroid, Diamond, and Primitive structures are the most frequently tested for bone tissue engineering. Gyroid scaffolds have higher permeability, aiding cell seeding, infiltration, differentiation, and new tissue formation. [62] Diamond structures offer higher interconnectivity, providing better mechanical stability and matching the properties of peripheral bone tissues to avoid stress shielding. [63] Diamond designs also exhibit the best strength [64], elasticity, and energy absorption, although Primitive lattices have a higher elastic modulus.[65]

Despite extensive testing, the optimal TPMS microarchitecture for bone tissue engineering remains unclear, with conflicting results on the influence of scaffold microarchitecture on cell growth. Diamond scaffolds are stiffer but have higher cell death levels [66], whereas Gyroid scaffolds show higher cell viability [54]. Diamond structures demonstrate good cytocompatibility [67], and Primitive microarchitectures enhance cell differentiation [63]. In summary, the best TPMS structure for cell proliferation and differentiation has yet to be determined.

By optimizing the physical properties of TPMS scaffolds, researchers can enhance their benefits and improve their ability to support bone regeneration. Numerous reviews have detailed methods for manufacturing TPMS scaffolds with varying properties, such as mechanical strength, permeability, and curvature [53]. Additionally, various structures have been designed, including graded, heterogeneous, multiscale TPMS, and TPMS with complex external shapes [52].

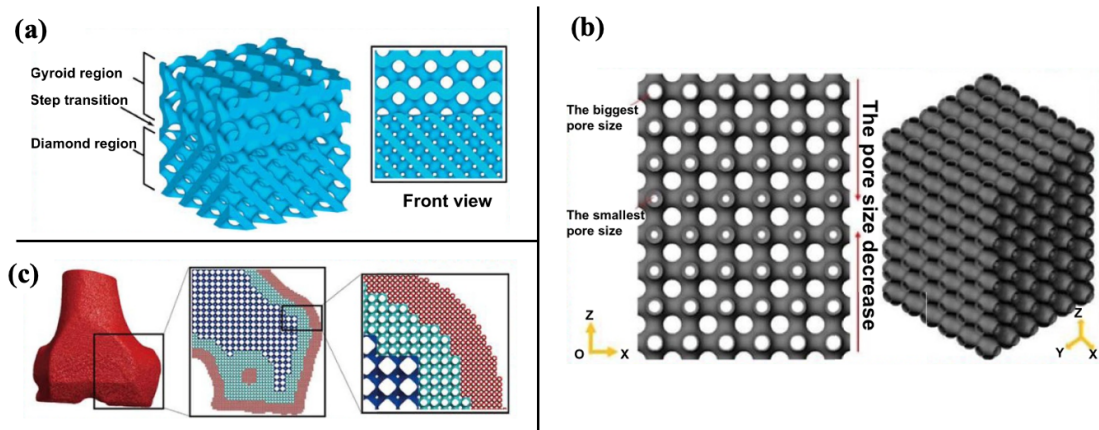


Figure 1.19 – Examples of (a) Graded, (b) Heterogeneous and (c) multiscale TPMS.[52]

1.7 Aim of the thesis

This thesis explores the mechanical performance of a multi-layer beam within a sandwich structure, featuring a soft interior core and a hard exterior shell. This approach is inspired by the work of Yavas et al. and seeks to leverage the strength of the hard outer shell while maintaining excellent toughness through the soft inner core, drawing parallels with the structural properties observed in natural tissues. Yavas and his colleagues introduced an extrusion-based 3D printing method to create multi-material lattices with adjustable mechanical properties. Inspired by bone structures, their approach utilized flexible thermoplastic polymers for the core and rigid materials for the shell. The lattice truss elements were configured in a sandwich structure, allowing mechanical tuning by varying the core-to-strut thickness ratio. They examined the bending behavior of these struts with different thickness ratios using 3-point bending tests, aiming to optimize energy absorption performance through variations in layer thickness ratios[29] .

Furthermore, this study explores the impact of incorporating a soft interface, inspired by findings from Mueller. Mueller's research involved the production of orthotropic lattices using a multicore-shell 3D printing technique, combining a flexible epoxy core with a brittle epoxy shell, with or without an elastomeric silicone interfacial layer. Their results demonstrated that lattices with a brittle shell and a flexible core-elastomer interface exhibited both high stiffness and toughness [28].

Additionally, it is known that the printing direction significantly influences the interface between constituents, impacting the mechanical behaviour of the sample, as demonstrated by Zorzetto et al. [68]. Since this study focuses on cellular solids, where constituent elements are inherently printed in all directions, a series of tests will be conducted to quantitatively assess the influence of these printing directions on the mechanical performance of the samples.

Beyond the analysis of individual beams, this research expands to investigate 3D-printed Triply Periodic Minimal Surface (TPMS) cellular solids. It examines the integration of multi-layer struts within these cellular structures to determine if their mechanical performance, particularly energy absorption, can be enhanced. This study introduces a novel degree of freedom by focusing on material properties rather than solely on microstructural design. The goal is to optimize the energy absorption characteristics of the composite beam by adjusting the material properties within a cellular solid framework.

In summary, this thesis aims to advance the field of architectural materials by thoroughly evaluating their mechanical behavior. Specifically, the objective is to identify and provide material combinations that enhance the design space of cellular solids, with a particular focus on improving energy absorption capabilities.

Chapter 2

Single Rectangular Beam Structure

2.1 Methods and Materials

The objective of this study is to optimize the mechanical properties of multi-material cellular TPMS scaffolds by varying the ratio of hard to soft materials within their wall struts. To assess these properties, the behavior of these lattice materials under compression is examined. The initial elastic response of cellular materials under compression is primarily governed by the bending behavior of the cell wall struts. Therefore, a thorough understanding of the flexural behavior of multi-material struts is essential for evaluating the in-plane compression performance of 3D-printed multi-material lattice TPMS structures. To investigate this, 3-point bending tests were conducted on 3D-printed rectangular beams representing lattice struts with varying core-to-strut thickness ratios.

Initially, these properties are assessed using simple rectangular beams with sandwich structure. The behavior of these beams is observed as the core-to-shell ratio is altered, and this is compared to a configuration that includes an interface between the soft core and the hard shell.

The sandwich beams without an interface are referred to as the C-S configuration, while those with an interface are referred to as the C-I-S configuration, as described in Mueller's article [28].

2.1.1 Materials

In this study, VeroWhitePlus (VW+) and TangoBlackPlus (TB+) were selected as base materials. VW+ is rigid, while TB+ is rubbery. Figure 2.1 provides an overview of these two base materials and their possible combinations, along with the qualitative stress-strain responses for VW+, RGD6, FLX6, and TB+.

Indeed, two categories of materials exist based on their combination and mechanical properties:

- Rigid materials (including VW and RGD1-6): Based on VW+ and TB+, they have their volume fraction mainly made of VW+ and are characterized by a high Young's modulus and ultimate tensile strength (UTS), but a low failure strain.
- Flexible materials (including TB and FLX1-6): Based on VW+ and TB, they have their volume fraction mainly made of TB+, featuring a lower Young's modulus and UTS, but a high failure strain.

Overall, there are 12 intermediate volumetric fractions with varying percentages of VW+ and TB+, resulting in different Young's moduli.

RGD6 (Grey60) and FLX6 (Shore95) are called digital materials, and other digital materials are omitted as their stress-strain curves are similar and fall between those of VW/RGD6 and TB/FLX6. [42] Both Grey60 and Shore95 are made by mixing VW+ and TB+. Grey60 (RGD6), is the most flexible material within the VeroWhite family containing 18% of TB, and Shore95 (FLX6) is the stiffest mixture within the TangoBlack family containing 64% of TB+.

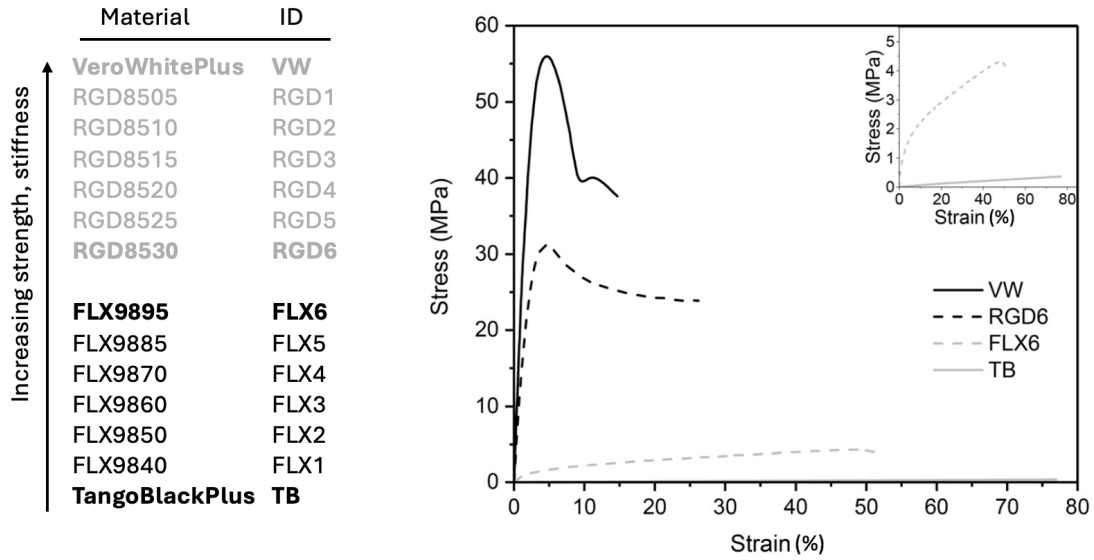


Figure 2.1 – Overview of the base materials VeroWhitePlus (VW) and TangoBlackPlus (TB), the printable digital materials from these using the Stratasys Connex3 Objet500, and their study IDs. [42]

	Mueller		Stratasys printer	
Hard shell	Brittle epoxy	E = 5 [GPa]	VeroWhite	E = 2 [GPa]
Interface	Silicone		TangoBlackPlus	E = 0.001 [GPa]
Soft core	Flexible epoxy	E = 1 [GPa]	Shore95	E = 0.3 [GPa]

Table 2.1 – Materials' properties.

To maintain coherence with Mueller's article and enable comparison with his results, materials were selected to match Mueller's properties as closely as possible, given the limited choice available with the Stratasys printer. Mueller utilized brittle epoxy (E = 5 GPa) for the hard shell, flexible epoxy (E = 1 GPa) for the soft core, and an elastomeric silicone for the interface.

In this study, VW+ was chosen as the stiffest available material, while TB+ was selected for its high flexibility, making them suitable for the hard shell and interface, respectively. For the core material, a mid-range stiffness was required. The options considered then, were Grey60 (RGD6) and Shore95 (FLX6).

The ratio of the Young's modulus between Mueller's brittle epoxy (E = 5 GPa) and flexible epoxy (E = 1 GPa), which is 5, was compared to the ratios between VW+ and the two candidate core materials to determine the closest match. Shore95, with a Young's modulus of 0.3 GPa, yields a ratio of 6.6 when compared to VeroWhite, while Grey60, with a Young's modulus of 1.1 GPa, yields a ratio of 1.8. Consequently, Shore95 was selected as the core material for this study due to its closer alignment with Mueller's material properties.

$$\frac{E_{\text{brittle epoxy}}}{E_{\text{flexible epoxy}}} = 5$$

$$\frac{E_{\text{VW}}}{E_{\text{Grey60}}} = 1.1 \quad \frac{E_{\text{VW}}}{E_{\text{Shore95}}} = 6.6$$

In summary, two groups of rectangular beam specimens were designed, using a sandwich configuration of two materials. The hard shell material consists of the base material VW+ with a flexural strength of 70-85 MPa, a flexural modulus of 2000-2500 MPa, and a failure strain of 5%-20% [38]. The soft core material is made of the digital material Shore95 with a strength of 8.5-10 MPa and a failure strain of 35%-45% [39]. Shore95 is composed of a mixture of VW+ and TB+.

The first group of specimens features a C-S (Core – Shell) configuration, without an interlayer of TB+. In this design, each VW+ specimen incorporates one layer of Shore95, resulting in two interfaces between Shore95 and VW+, as depicted in Figure 2.2.

The second group of specimens consists of a C-I-S (Core – Interface – Shell) configuration including two thin layers of TB+ as interfaces between the core and the shell, as shown in Figure 2.2.

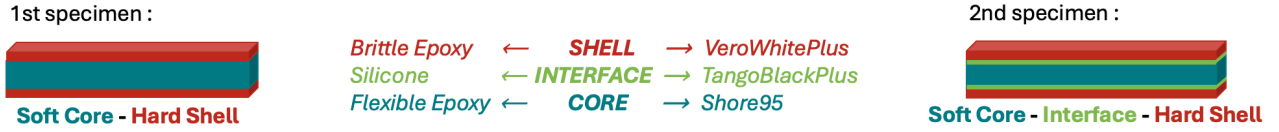


Figure 2.2 – Design and materials of the 2 groups of specimen.

2.1.2 Sample design and dimensions

To ensure the failure of the shell, specific beam dimensions were calculated based on the fracture strain of VeroWhitePlus. The strut deflection was fixed at $\delta = 9$ mm, and the following equation was used:

$$\epsilon = \frac{6\delta t}{L^2}$$

with t , the beam thickness and L , the span length.

This equation originates from the theory of linear elasticity and beam bending, specifically for 3-point bending tests. It relates the mid-span deflection to the surface strain in a beam and is applicable to small deflections in homogeneous, isotropic materials that follow Hooke's Law. This formula is commonly used to determine the flexural properties of materials in mechanical and structural testing.

As shown Figure 2.3, the fracture strain of VeroWhitePlus ranges from 10% to 20%. For calculations, a fracture strain of 20% was selected to ensure failure. Consequently we have:

$$\epsilon_f = \frac{6\delta t}{L^2} = 20\%$$

with a beam deflection of approximately $\delta = 9$ mm, a beam thickness fixed at $t = 6$ mm, a span length of $L = 40$ mm and a total beam length of 50 mm were found.

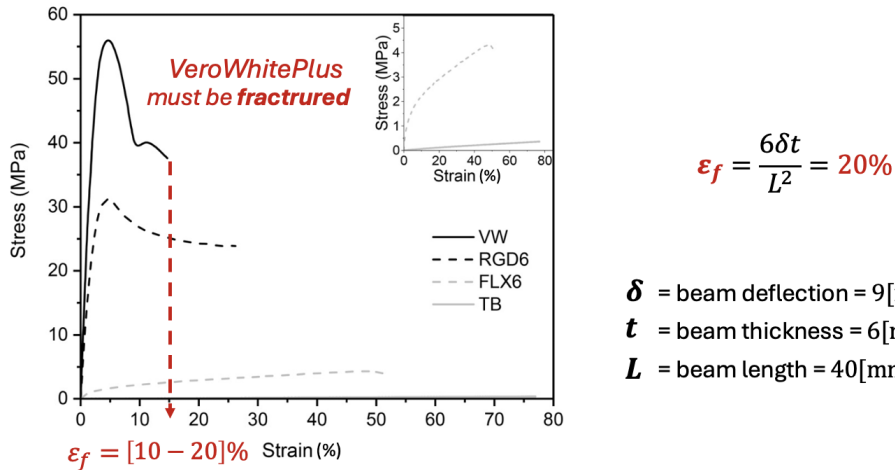


Figure 2.3 – Stress-strain-curve of VeroWhite and fracture strain (figure adapted from [42]).

Individual struts composed of a brittle shell and a flexible core were printed both with and without an elastomeric interlayer. The thickness of the interfacial layer was kept as thin as possible to ensure a reliable separation of the core and shell while being thick enough to maintain a pure TangoBlackPlus composition. Zorzetto et al. [68] demonstrated that material mixing occurs during deposition by the printer, hence a layer that is too thin cannot remain purely TB+. Given the printer's resolution along the z-axis is 0.03175 mm,

and the thickness is printed along this direction, the interface thickness was set to approximately 0.0635 mm, equivalent to two voxel sizes, to ensure purity and functionality. The dimensions and parameters of the singular beam are illustrated in Figure 2.4. In this context, d corresponds to the thickness of one layer of the shell, i to the thickness of the interlayer, and c to the core thickness.

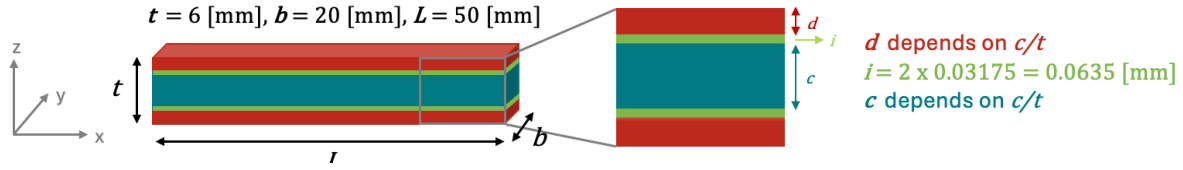


Figure 2.4 – Dimensions of the sample beam.

The thickness of the core and shell varied according to the ratios used to tune the mechanical properties for comparison purposes. The core-to-strut-thickness ratio was employed as a tool to assess the impact of thickness on the effective mechanical properties and evaluate the material's behavior. To ensure coherence and comparability, the same ratios used by Mueller [28] were chosen i.e. $c/t = 0, 0.05, 0.1, 0.2, 0.4, 0.6, 0.8$, and 1. A ratio of 0 corresponds to a pure VeroWhitePlus beam, while a ratio of 1 corresponds to a pure Shore95 beam.

For the first group of specimens with a C-S configuration, with a length of 50 mm and a thickness of 6 mm, the Shore95 thickness was set at 0.3, 0.6, 1.2, 2.4, 3.6, and 4.8 mm based on the different ratios. In the second group of specimens with a C-I-S configuration, the thickness of the TangoBlackPlus interface remained constant at 2 voxels (0.06 mm) for each specimen, as did the total thickness of the beam and the hard shell. Consequently, for the second configuration, the Shore95 thickness varied as follows: 0.18, 9.48, 1.08, 2.28, 3.48, and 4.68 mm. All of those values are summarized in Table 2.5.

	C-S (8x3 = 24 samples)			C-I-S (6x3 = 18 samples)			
	Ratio c/t	Hard Shell d [mm]	Soft Core c [mm]	Ratio c/t	Hard Shell d [mm]	Interface i [mm]	Soft Core c [mm]
Pure VW	0	3	0				
Ratio 1	0.05	2.85	0.3	0.05	2.85	0.06	0.18
Ratio 2	0.1	2.7	0.6	0.1	2.7	0.06	0.48
Ratio 3	0.2	2.4	1.2	0.2	2.4	0.06	1.08
Ratio 4	0.4	1.8	2.4	0.4	1.8	0.06	2.28
Ratio 5	0.6	1.2	3.6	0.6	1.2	0.06	3.48
Ratio 6	0.8	0.6	4.8	0.8	0.6	0.06	4.68
Pure Shore95	1	0	6				

Figure 2.5 – Beam dimensions.

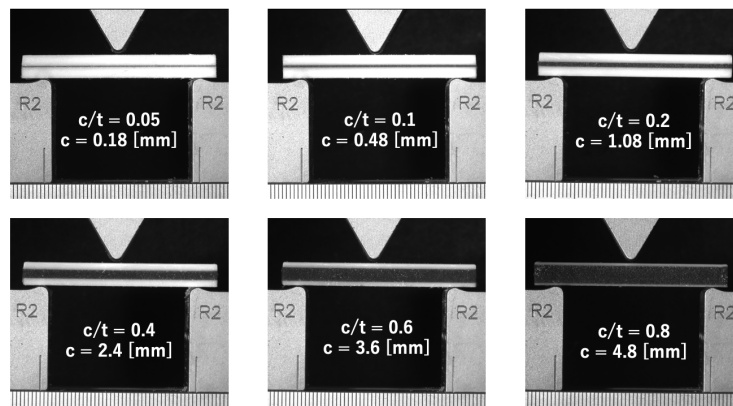


Figure 2.6 – Illustration of the samples for all ratios.

2.1.3 Sample 3D printing

All test specimens were fabricated using a Stratasys Objet260 Connex2 printer, which employs polyjet technology as previously described. The composite specimens were printed in digital material mode, allowing for the simultaneous use of multiple materials. Throughout the printing process, the printheads are precisely positioned according to the design specifications. They move back and forth along the X-direction, jetting liquid-like base materials from the nozzles. These materials are promptly cured by UV lights, ensuring accurate layer-by-layer construction. This careful process continues until the specimens achieve the specified design height.

Figure 2.7 shows a schematic illustrating the orientations of the samples relative to the printing bed. The strategic positioning of the samples on the build platform, as well as their arrangement in relation to one another, is critically important. The specimens were intentionally spaced apart to address a default behavior of the printer, which initially clusters all samples at the top left of the build area. This clustering can lead to performance inconsistencies, as the printer's head repeatedly returns to the origin for each X-layer, causing increased UV light exposure in this region.

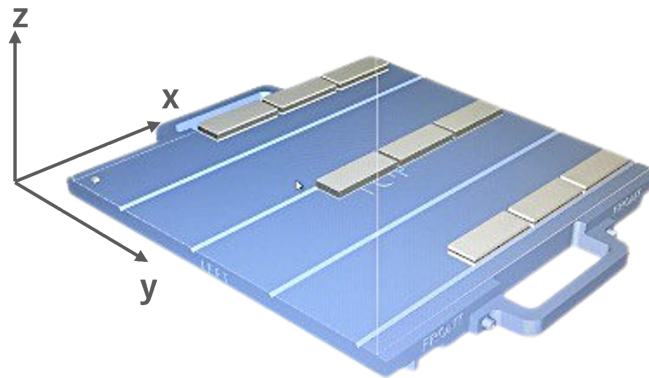


Figure 2.7 – Samples printing orientation.

To achieve a consistent and smooth surface finish while minimizing overcuring, all surfaces are initially covered in support material during printing. However, for subsequent prints (at ratios of 0.1 and 0.05, and for all future samples), the support material is applied only to the bottom of the samples. This adjustment is made to optimize printing time without sacrificing quality. After printing, the support material is removed manually using mechanical methods rather than water-jet or chemical processes. It is important to note that the support wax creates a slight asymmetry in surface finishes: the top surfaces of the samples are glossy and free of wax, while the bottom surfaces exhibit a matte finish due to the wax. From a rigorous testing perspective, this surface finish asymmetry could affect the appearance of cracks. Therefore, to account for this potential influence, the wax-coated bottom portion is positioned to face downwards, assuming it represents the initial point of crack formation. These careful considerations ensure methodological precision in the experimental setup.

To minimize side effects, the struts are tested within 24 hours of printing. The specimens are stored in an air-conditioned environment with a controlled room temperature of 23 °C. Consistent parameters are essential for reproducible results when comparing different parts or batches. This involves controlling storage time, environmental conditions, and positioning on the print table. Various studies have investigated the influence of printing process parameters on material properties [36, 41, 43, 44], consistently demonstrating their significant impact on aspects such as interface strength, fatigue behavior, and failure mechanisms. Understanding and controlling these parameters is critical for optimizing the performance and reliability of multi-material 3D printed structures.

To ensure the statistical significance of the results, each specimen was replicated three times. This replication enabled the estimation of experimental variability, reliability, and accuracy. Additionally, specimens were printed in two separate batches to further verify consistency across different print runs. All tests were

conducted on each of the three samples to assess statistical variability, with the reported properties representing the mean values derived from these samples. This approach ensured a thorough assessment of the mechanical properties and their variability, providing a reliable dataset for subsequent analysis.

To investigate the impact of interface characteristics dependent on printing orientation, all samples were printed under consistent conditions except for their orientation. Initially, samples were printed horizontally for all core-to-strut ratios, both with and without the softer interface. Subsequently, the samples were reprinted vertically but only without the softer layers. This change in orientation substantially affected the interface characteristics, as documented in the study by Laura Zorzetto [68]. This approach enabled the isolation and assessment of the effect of printing orientation on interface behavior, while ensuring that all other printing parameters remained uniform across the samples.

2.1.4 Sample testing: 3 point bending test

As said previously, three-point bending tests were performed on our 3D-printed rectangular beams with varying core-to-strut thickness ratios. These tests aimed to evaluate the flexural modulus, strength, and energy absorption capabilities of the multi-material beam. The results provide valuable insights into the mechanical performance of these struts under bending loads, contributing to a better understanding of their overall behavior in lattice structures.

Three-point bending tests were performed on all samples of multi-material core-shell struts (CS) with core-to-strut-thickness ratios (c/t) of 0, 0.05, 0.1 0.2, 0.4, 0.6, 0.8, and 1. Additionally, tests were conducted on multi-material core-interface-shell struts (C-I-S) with same core-to-strut-thickness ratios.

A three-point bending test with controlled displacement was conducted. In this test, the specimen, with known dimensions, is placed on two lower supports spaced a specific distance apart, referred to as the support span. A indenter or crosshead is positioned at the midpoint of the specimen's span. Initially, the specimen rest on the two supports, ensuring it is centered and properly aligned. The indenter is then lowered at a constant displacement rate, moving at a consistent speed rather than applying a constant load, hence the term "controlled displacement test." As the indenter descended, it applies a concentrated force at the midpoint of the specimen, causing it to bend. This bending deformation result in compression in the top fibers and tension in the bottom fibers of the specimen. All tests were halted when the crosshead displacement reached 20mm as a safety precaution. Beyond this point, the crosshead would risk contacting the bottom of the support part and potentially damaging the load cell.

The experiments were conducted using an MTS testing machine equipped with a 2.5 kN load cell and a three-point flexural test rig. The revolving roller diameters were 4 mm (R2), and the span length was set to 40 mm. The tests were performed at a constant crosshead speed of 5 mm/min, in accordance with the methodologies of Yavas [29] and Mueller [28]. A preload of 0.5 N was applied to detect contact and ensure the measurement commenced at zero. The experimental setup is illustrated in Figure 2.8, detailing the arrangement and parameters used for the tests.

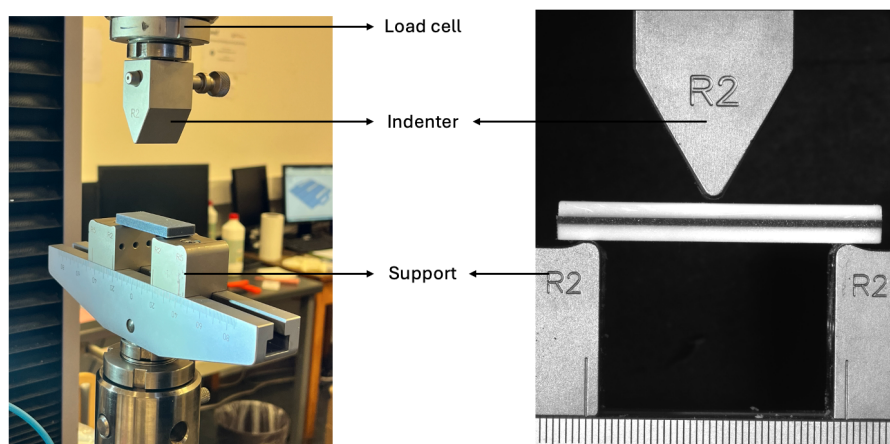


Figure 2.8 – Three-point bending test set up.

Stress-strain curves

During the test, both the crosshead displacement and the reaction force are accurately measured using a displacement transducer and a load cell, respectively. This data is then used to calculate the **flexural stress** (σ) and **strain** (ϵ) with the following equations:

$$\sigma = \frac{3PL}{2bt^2} \quad \text{and} \quad \epsilon = \frac{6\delta t}{L^2}$$

where

- P is the measured force i.e. the reaction load at the center
- δ is the mid-span deflection i.e. the displacement measured at the center
- t is the sample thickness, perpendicular to the reaction load.
- b is the sample width, perpendicular to the thickness.
- L is the support span length i.e. the distance between the two supports

These equations are fundamental for evaluating the flexural properties of materials and are derived from the simple beam theory. The first equation originates from the relationship between the bending moment and the section modulus of a rectangular cross-section, while the second equation pertains to the beam's curvature and its dimensions. Flexural stress (σ) is calculated by dividing the applied load by the original, undeformed cross-sectional area of the specimen. Flexural strain (ϵ) is determined by dividing the elongation of the specimen's narrow section by its original, undeformed length.

Those stress and strain formulas for homogeneous beams act as a standardizing tool, enabling effective comparison across various samples. These formulas are appropriate for comparative analysis, given that they are applied consistently under comparable conditions. This suitability arises from the fact that parameters such as length (L), width (b), and thickness (t) remain constant across all core-to-strut ratios in the study. By keeping these dimensions uniform, the normalization process ensures that observed differences in mechanical behavior are not influenced by variations in sample size, thus providing a clear basis for comparison.

Flexural modulus and Yield strength

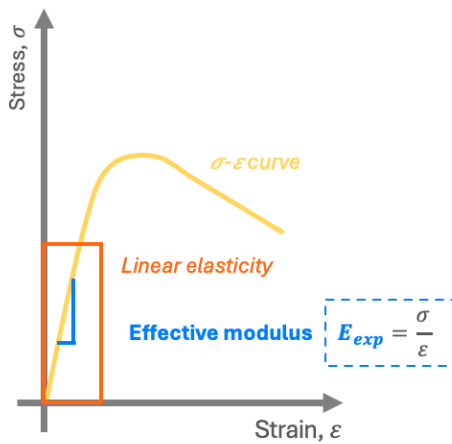


Figure 2.9 – Flexural Modulus computation.

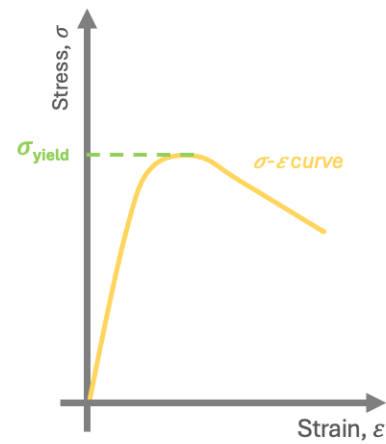


Figure 2.10 – Yield strength computation.

The slope of the initial linear portion of the stress-strain curve, illustrated in Figure 2.9, represents the elastic region where the material deforms but can return to its original shape when the load is removed. On this linear segment, the following linear relationship is applicable (Hooke's law):

$$\sigma = E \cdot \varepsilon$$

where σ is the stress, ε is the strain and E is the effective modulus.

The **effective flexural modulus** refers to the apparent stiffness or elasticity of a composite material, providing a single value that describes the overall elastic response under applied loads.

This experimentally measured effective flexural modulus of the 3D printed multi-material struts was then compared with analytical estimations. The effective flexural modulus was analytically estimated using the classical Euler-Bernoulli beam theory as presented by Yavas [29], represented by the following equation:

$$E = E_{core} \frac{I_{core}}{I} + E_{shell} \frac{I_{shell}}{I}$$

In this equation, E_{core} and E_{shell} denote the Young's moduli of the core and shell materials, which in this case are substituted by the elastic moduli of Shore95 and VeroWhitePlus, respectively. The term I represents the second moment of area of the entire cross-section, calculated as $I = \frac{1}{12}bt^3$. Additionally, I_{core} is the second moment of area of the core, given by $EI_{core} = \frac{1}{12}bc^3$, while I_{shell} is the second moment of area of the shell, which can be determined using the parallel axis theorem. Accordingly, the equation becomes

$$E = E_{Shore95} \left(\frac{c}{t}\right)^3 + E_{VW} + \frac{1}{4} \left(\frac{t-c}{t}\right)^3 + E_{VW} + \frac{3}{4} \frac{(t-c)(t+c)^2}{t^3}$$

The application of the parallel axis theorem allows for the calculation of the second moment of area of the shell, I_{shell} by considering the contributions of the shell sections about the centroid of the entire cross-section. Although more complex theories, such as the Timoshenko beam theory, could be utilized, the classical Euler-Bernoulli beam theory was deemed sufficient for a first-order approximation of the effective flexural modulus of the multi-material struts in this study.

The parameters involved in this analysis include the Young's moduli of the core and shell materials, which reflect their respective stiffness, and the second moment of area, which indicates the distribution of cross-sectional area relative to an axis, thereby affecting bending stiffness. The dimensions of the core and shell are crucial for determining the second moment of area using the parallel axis theorem.

By applying these principles, the effective flexural modulus of the multi-material struts was accurately estimated and subsequently validated against experimental measurements.

Another method for calculating the theoretical effective modulus is by using the Gibson and Ashby approach [1], as expressed by the following equations:

$$EI = \frac{b}{12} (t^3 - c^3) E_{VW} + \frac{bc^3}{12} E_{Shore95}$$

$$E = \frac{12EI}{bt^3}$$

Both formulas yield the same results.

Beyond the elastic limit, the material enters the plastic region where permanent deformation occurs, and the peak of the curve indicates the maximum load the material can withstand before it starts to deform plastically. This peak stress on the stress-strain curve, as shown in Figure 2.10, is considered as the **yield strength**.

Energy absorption and Energy absorption efficiency

The **energy absorption** measures the material's capacity to absorb energy from deformation before reaching failure. This energy (represented as strain energy density, W) is determined by integrating the area under the flexural stress–strain curves from $\varepsilon = 0$ to ε_f , the strain value before the slipping or the fracture of the sample.

$$W = \int_0^{\varepsilon_f} \sigma(\varepsilon) d\varepsilon$$

Energy absorption can be accurately assessed using stress-strain calculations, provided that the parameters remain constant across samples.

Depending on the ratio and the samples, the upper limit ε_f can vary significantly. Consequently, energy absorption was assessed in two ways. Initially, as illustrated in Figure 2.11 in pink, the energy absorption of all samples was calculated up to the deformation point where the first sample slipped, which occurred at a deformation of 27.5% for the 0.4 ratio sample. Subsequently, shown in purple, the energy absorbed up to the individual critical points for each sample was calculated. For fractured samples, energy was calculated up to the point of fracture; for slipped samples, up to their individual slip points. To determine these critical points, videos of the tests were reviewed to identify when each sample fractured or slipped. From these time values, the corresponding strain and stress values were obtained.

To better understand energy efficiency, the Energy Absorption Efficiency (EAE) was calculated. EAE represents the ratio between the energy actually absorbed (the yellow area in Figure 2.12) and the maximum energy that can be absorbed (the blue area in Figure 2.12). This ratio is also defined as the area under the stress-strain curve divided by the area of the rectangle bounded by the maximum stress and maximum strain. The formula is as follows:

$$EAE = \frac{E_{abs}}{E_{abs_{max}}}$$

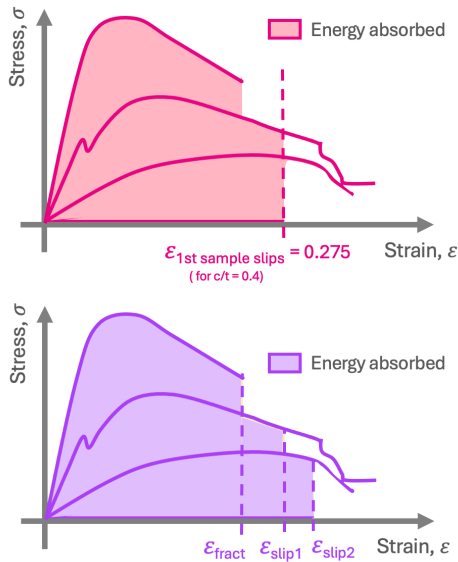


Figure 2.11 – Energy Absorption computation.

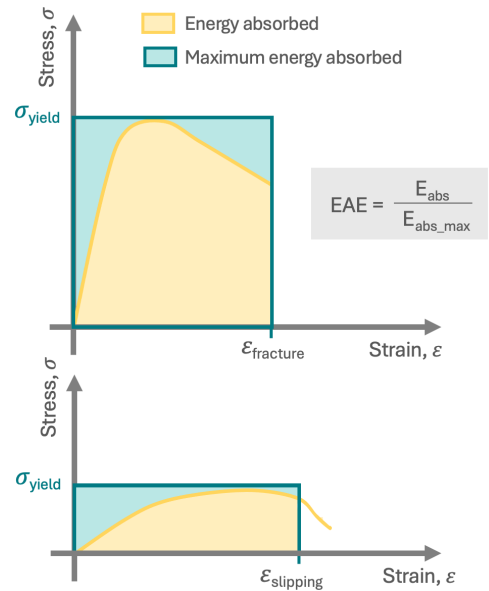


Figure 2.12 – Energy Absorption Efficiency computation.

2.1.5 Digital Image Correlation (DIC)

Digital Image Correlation (DIC) is a powerful optical method used to measure displacement and strain fields within a region of interest (ROI) during material deformation. This technique relies on capturing images of

a deforming sample and processing them to extract precise deformation data, employing image processing techniques, as illustrated in Figure 2.13.

The images collected were analyzed using the 2D DIC software Ncorr. Despite significant advancements in both experimental DIC methods and computational algorithms, there remains a gap in the availability of high-quality, free, and flexible DIC software that allows for customization. Addressing this need is the Ncorr software package, which integrates contemporary DIC algorithms with additional enhancements in an open-source framework [70].

Developed at the Georgia Institute of Technology by Antonia Antoniou's group, Ncorr operates within the MATLAB environment and excels at estimating displacement and strain fields from input speckle images[70]. To evaluate its performance, Harilal et al.[71] conducted a series of experiments comparing Ncorr's results with those from Vic 2D, a well-established commercial software from Correlated Solutions Inc., USA. The findings demonstrated a strong agreement between Ncorr and Vic 2D, highlighting the efficacy and value of this open-source, MATLAB-based DIC software in providing reliable and accurate measurements of material deformation.

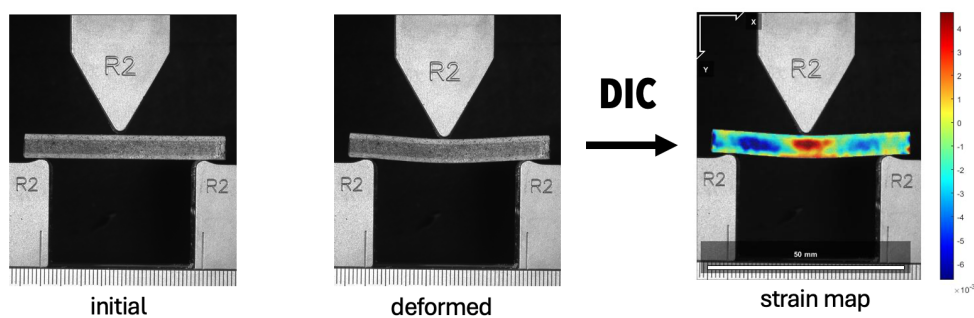


Figure 2.13 – Principle of Digital Image Correlation.

The Digital Image Correlation (DIC) analysis requires capturing images of a deforming sample and using these images to track the movement of specific points on the sample during deformation. For accurate point recognition, a pattern with high contrast is essential, as outlined on the Ncorr manual [69].

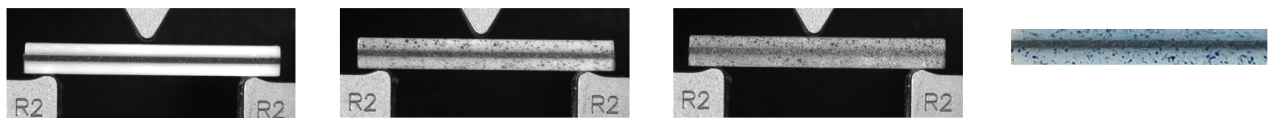


Figure 2.14 – 1st sample not painted and 2nd and 3rd samples painted with speckle pattern.

To achieve this, two of the three samples were painted with a speckle pattern, as shown in Figure 2.14. Optimal results were obtained by applying painted drops in a random arrangement, varying in size and color. Initially, grey drops were used to create a background speckle pattern, followed by blue drops applied on top to enhance contrast. Small, random, and non-uniform speckles were created using aerosol paint, sprayed from a certain distance to ensure variability. This approach improved the accuracy of the DIC analysis by providing a distinct and well-defined speckle pattern for precise tracking of deformation.

During the test, the applied crosshead displacement, reaction force, and digital images of the sample's side were recorded simultaneously. Optical images were captured using a Nikon AF Micro-Nikkor 60mm f/2.8D lens. To ensure high resolution and clarity, two unidirectional white lights were employed to provide diffuse, bi-directional lighting. The lighting and resolution of the images are critical parameters, as DIC relies on the contrast of the speckles in the samples. If the lighting is either too intense or insufficient, the contrast will be suboptimal, adversely affecting the DIC analysis.

Initially, an image acquisition rate of 2 Hz (2 images per second) was used for the first test (sample 1, specimen 1). However, due to the rapid progression of the test and the need for higher image precision

for Digital Image Correlation (DIC), the acquisition rate was increased to 4 Hz for all subsequent tests. Approximately 1000 images were captured in a single video of a sample undergoing loading. Videos were recorded until the crosshead distance reached 20 mm, at which point all samples had either slipped or fractured.

The entire process for conducting DIC is summarized in the following image 2.15.

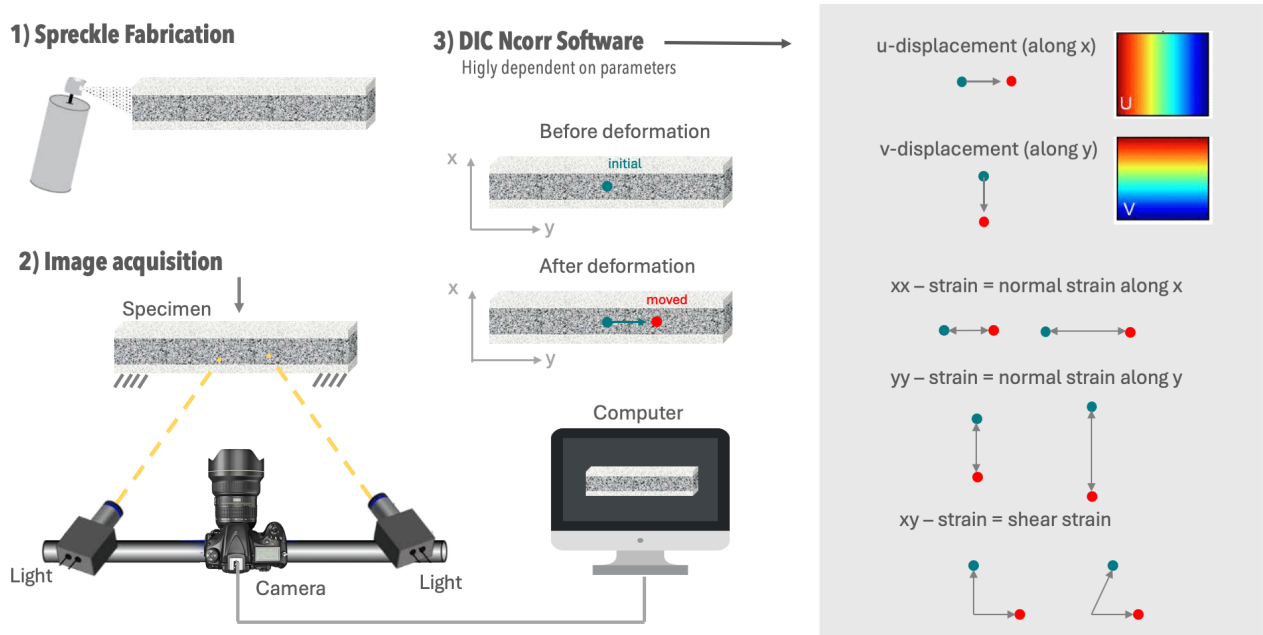


Figure 2.15 – Process of DIC.

The process involves establishing a correspondence between material points in the reference image, which represents the undeformed state of the sample, and the current images, which capture the sample's state at various stages of deformation under load. This correspondence is achieved by dividing the reference image into small, defined subsets, which are groups of coordinates as illustrated Figure 2.16. For each subset, displacement and strain information is determined by matching its location in the current images. This matching process is initially performed within a selected region of interest, allowing for detailed analysis of how each subset has moved and deformed.

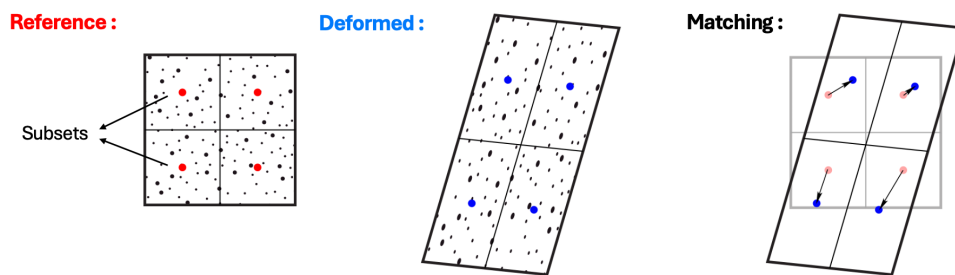


Figure 2.16 – DIC subsets theory (adapted from [72]).

The quality of Digital Image Correlation (DIC) analysis is influenced by several factors and parameters, making it crucial to carefully consider and specify these variables to ensure accurate results. To achieve this, multiple current images were analyzed simultaneously using a sequence of images. It was essential to select images taken shortly after the reference image to avoid significant deformation that could obscure the area of interest. Current images were captured during the early stages of deformation, while the sample was still in the elastic region. DIC analysis was conducted on all samples in both configurations (C-S and C-I-S). Despite variations in scale across samples, the analysis focused on the color-coded areas. However, this approach was not entirely reliable, indicating potential areas for improvement in the analysis method.

A critical aspect of Digital Image Correlation (DIC) analysis is the choice of subset parameters, particularly subset size and spacing, illustrated in Figure 2.17. In this study, the spacing between subsets was maintained at the default value of 5 to achieve a balance between resolution and computational efficiency. Although reducing the spacing increases resolution, it must align with the speckle pattern on the sample to ensure accurate measurement. The subset radius, or size, is essential for precise analysis. While there are many guidelines in the literature for selecting subset sizes, these recommendations are often based on empirical data. The goal is to choose the smallest subset size that provides reliable displacement data without excessive noise, as larger subsets can smooth out important details. For this study, a subset size of 30 was selected. This parameter may need further adjustment to optimize results[69].

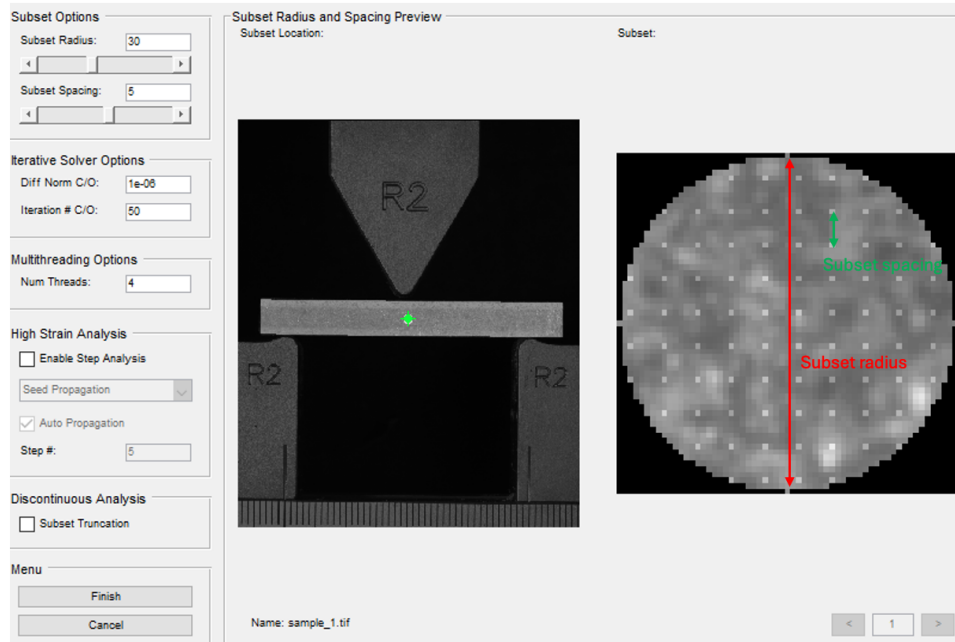


Figure 2.17 – DIC subsets option: subset radius and spacing.

Another important parameter is seed placement, which serves two main purposes: providing initial guesses for the DIC analysis and partitioning the region of interest (ROI). To ensure accurate analysis, seeds must remain within the field of view (FOV) during deformation and be evenly distributed to partition the ROI. Incorrect seed placement can result from convergence failures or seeds moving outside the current image during sample deformation. This issue illustrated in Figure 2.18 where the seed goes “out of the picture”, underscores why significant deformations between the reference and current images can cause poor analysis. Successful seed placement is indicated by a low number of iterations required for convergence and a low correlation coefficient. In this study, seeds were consistently placed in the same positions, as shown in Figure 2.18. This approach ensured evenly spaced partitions and maintained a low correlation coefficient less than 1, demonstrating effective seed placement. An incorrect seed placement usually means that one seed needs to be moved, or the ROI needs to be redrawn[69].

Then, the software computes displacement data, which is then interpolated to create a continuous displacement field using the reliability-guided method developed by Bing Pan, as detailed on the Ncorr website [69]. Displacements are calculated both along the x-axis (horizontal), denoted as u [mm], and along the y-axis (vertical), denoted as v [mm], resulting in a grid that represents displacement relative to the reference configuration. An example is illustrated in Figure 2.19 and 2.20. In this representation, red hues indicate positive displacements, corresponding to movements to the right along the x-axis and downward along the y-axis, while blue shades denote negative displacements, indicating movements to the left along the x-axis and upward along the y-axis.

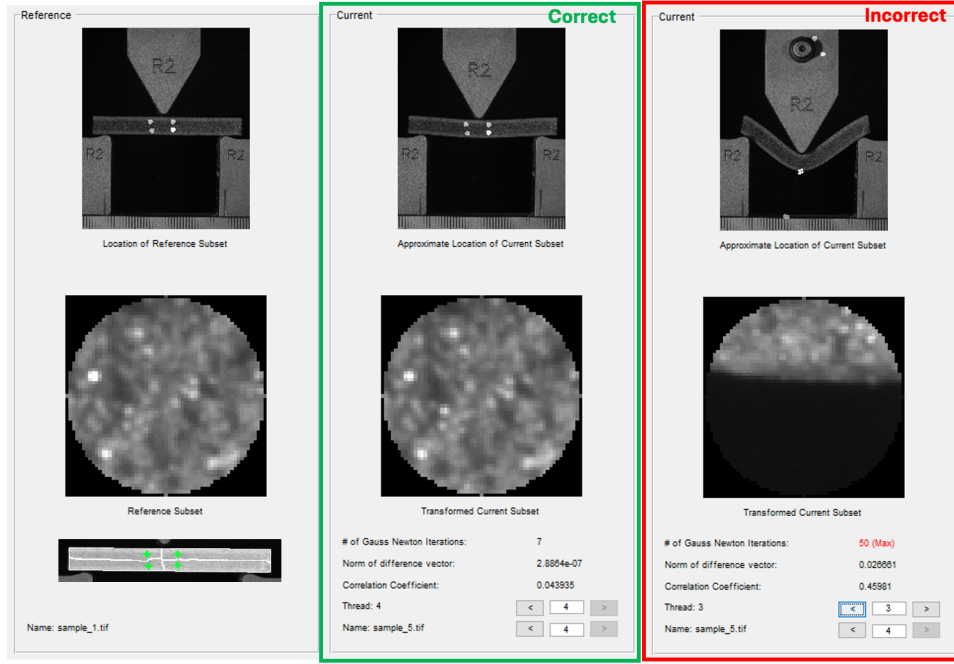


Figure 2.18 – DIC correct and incorrect seed placement procedure.

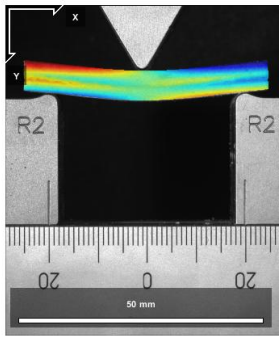


Figure 2.19 – u -displacement map for C-S sample with $c/t = 1$.

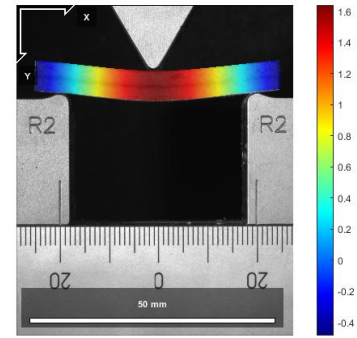


Figure 2.20 – v -displacement map for C-S sample with $c/t = 1$.

Using displacements data, strains, ϵ_{xx} , ϵ_{xy} and ϵ_{yy} are calculated using the four displacement gradients [69]:

$$\epsilon_{xx} = \frac{1}{2} \left(2 \frac{\partial u}{\partial x} \left(\frac{\partial u}{\partial x} \right)^2 + \left(\frac{\partial v}{\partial x} \right)^2 \right)$$

$$\epsilon_{xy} = \frac{1}{2} \left(\frac{\partial u}{\partial y} + \frac{\partial v}{\partial x} + \frac{\partial u}{\partial x} \frac{\partial u}{\partial y} + \frac{\partial v}{\partial x} \frac{\partial v}{\partial y} \right)$$

$$\epsilon_{yy} = \frac{1}{2} \left(2 \frac{\partial v}{\partial y} \left(\frac{\partial u}{\partial y} \right)^2 + \left(\frac{\partial v}{\partial y} \right)^2 \right)$$

Two types of strain can be calculated: Green-Lagrangian and Euler-Almansi strains. In this study, the Euler-Almansi strain is preferred over the Green-Lagrangian strain due to its suitability for analyzing deformation relative to the current, deformed state of the material. While the Green-Lagrangian strain measures deformation with respect to the original, undeformed configuration, the Euler-Almansi strain provides a direct assessment of changes based on the deformed state. This method offers a more accurate representation of the deformation occurring under load, thereby improving our ability to evaluate and interpret the material's behavior in significant strain conditions.

The Digital Image Correlation (DIC) technique generates a grid of strain information relative to the reference configuration, similar to the displacement fields. These strain fields are then interpolated to create continuous strain distributions. Examples of the 3 strains distribution calculated are shown in Figure 2.21.

- ϵ_{xx} [-] represents the normal strain along the x-axis, indicating changes in length in this direction. Positive values are depicted in red, corresponding to stretching of the material, while negative values are shown in blue, indicating compression.
- ϵ_{yy} [-] represents the normal strain along the y-axis, indicating changes in length in this direction. Positive values are depicted in red, corresponding to compression of the material, whereas negative values are shown in blue, indicating stretching.
- ϵ_{xy} denotes the shear strain, which represents changes in the angle.

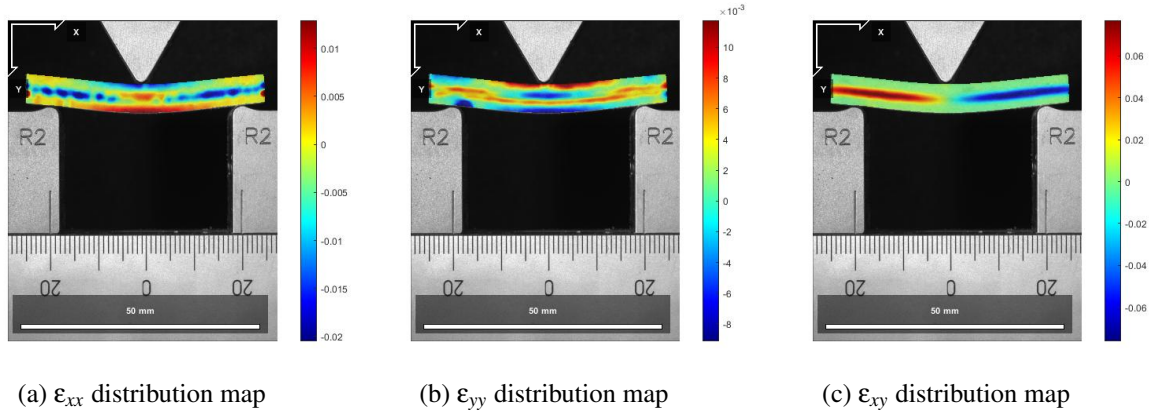


Figure 2.21 – Strains distribution map on a deformed C-S sample with ratio $c/t = 0.1$

As previously noted, it was crucial to select images taken shortly after the reference image to minimize significant deformation that could obscure the area of interest. Therefore, images were captured during the early stages of deformation while the sample remained in the elastic region. Figures 2.22 and 2.23 illustrate the stress and strain with the point value in strain where Digital Image Correlation (DIC) was conducted for C-S samples with core-to-strut ratios of 0.05 and 0.8, respectively. Other points for all other samples are shown in the appendix.

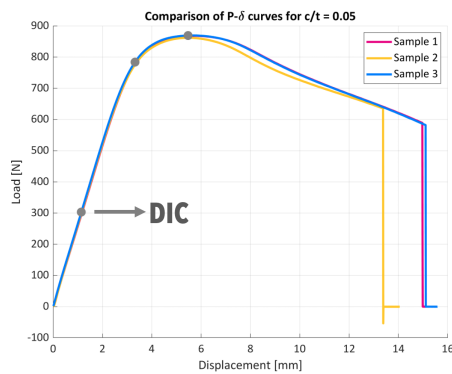


Figure 2.22 – Stress-strain curve for CS sample of ratio $c/t = 0.05$ with point indicating current image for DIC.

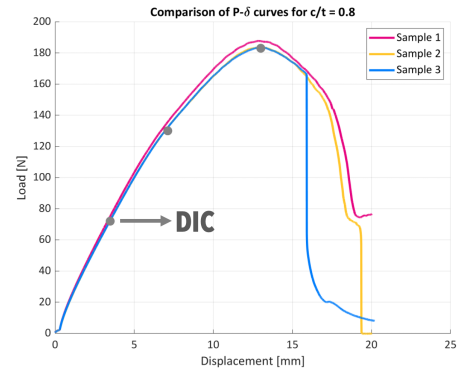


Figure 2.23 – Stress-strain curve for CS sample of ratio $c/t = 0.8$ with point indicating current image for DIC.

Given the substantial differences in sample behavior, DIC was performed at strategically chosen deformation points rather than at uniform strain values. This approach ensured that the samples were sufficiently deformed for analysis while maintaining accuracy. A total of five images were captured and loaded into the Ncorr software, representing various stages between the initial unloaded state and the final deformation point. However, only the final image, corresponding to the specific deformation point, was analyzed further in the thesis.

2.2 Results and Discussion

In this section, the range of mechanical properties from stiff to softer samples is investigated by varying the core thickness. The effect of adding a softer interface on mechanical performance is then examined, with reference to Mueller's study on round beams. Finally, the impact of printing orientation on the interface between the VeroWhite shell and the Shore95 core is studied.

2.2.1 Statistical variability between samples

The variations among the three samples for each model are minimal, indicating a high degree of reliability in the results. All samples exhibit nearly identical behavior until reaching a critical point, such as fracture or slipping. Notably, sample 1 consistently shows slightly higher values than samples 2 and 3. It is important to note that samples 2 and 3 were painted and thus subjected to more manipulation.

2.2.2 Core-Shell configuration

This section investigates the behavior of the first group of specimens, which consists of single rectangular beams with a soft core and a hard shell, without any interface. The objective is to determine whether the composite beam, depending on the core-to-strut thickness ratio, demonstrates superior mechanical performance compared to its individual components.

Stress-strain curves

The flexural stress–strain curve for a core-to-strut thickness ratio of $c/t = 0$, corresponding to pure VeroWhitePlus under loading and illustrated in Figure 2.24, demonstrates a linear deformation where the stress (force per unit area) increases with strain (deformation), indicative of elastic behavior. This linearity continues up to a critical stress level, or peak point, after which the stress decreases. This peak point represents the yield strength, measured at 79.92 [MPa], marking the transition to plastic deformation followed by a sudden force drop due to brittle fracture. Indeed, micro-cracks or voids may form and grow, reducing the effective cross-sectional area that can bear the load. This reduction in cross-sectional area results in a decrease in the material's ability to withstand force, even as elongation continues. The process eventually leads to material failure at approximately 55 [MPa]. Compared to existing studies, the experimental yield strength of VeroWhitePlus is notably higher. For example, Lumpe et al. [42] reported a yield strength of approximately 55 [MPa]. However, according to the VeroWhitePlus datasheet [38], the tensile strength is specified as ranging from 50 to 65 [MPa], which aligns with the observed fracture stress.

During the 3-point bending test on a pure VeroWhitePlus beam, theoretical predictions regarding the fracture behavior of the material were aimed to be validated. According to the calculations, the VeroWhitePlus was expected to fracture at 20% strain and a crosshead displacement of 9 [mm]. However, in the experimental trials, it is consistently observed that the VeroWhitePlus fractured at an average strain of 27% and a crosshead displacement of 12 [mm]. This observation indicates a 7% in absolute deviation from the theoretical predictions.

For the behavior of a beam of pure Shore95, the flexural stress–strain curve with a core-to-strut thickness ratio $c/t = 1$, illustrated in Figure 2.25, shows a rising trend up to nearly 25% strain without any indication of permanent deformation. The curve reaches a yield stress of approximately 2.8 [MPa], after which the stress decreases until slipping of the sample from the supports occurs. Post-slipping values are not reliable and thus are not considered. Given that Shore95 is a more rubber-like material, it can, as expected, withstand less force than VeroWhite before undergoing plastic deformation.

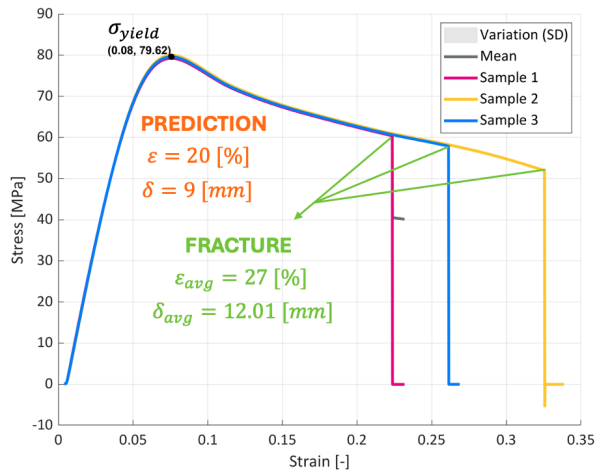


Figure 2.24 – Stress [MPa] vs Strain [-] for $c/t = 0.$

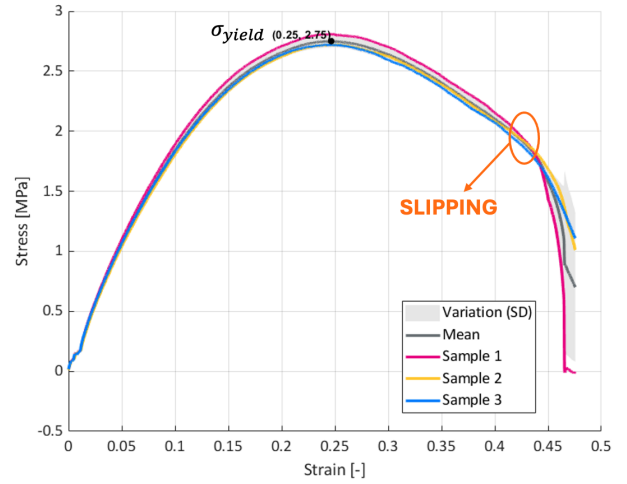


Figure 2.25 – Stress [MPa] vs Strain [-] for $c/t = 1.$

Figures 2.26 and 2.27 show the stress–strain curves of multi-material struts with $c/t = 0.05$ and $c/t = 0.1$, respectively. These samples have a larger shell layer, resulting in greater stiffness. Consequently, their stress–strain responses closely follow the behavior of VeroWhitePlus and have similar features.

Both core-to-thickness ratios, $c/t = 0.05$ and $c/t = 0.1$, initially exhibit a linear increase in stress up to their respective yield strengths of 72.20 [MPa] and 64.31 [MPa]. At these points, the outer VeroWhitePlus shell begins to yield under the applied tensile stress, resulting in a plateau in the stress–strain curve. Upon reaching a critical tensile stress level, a significant drop in the stress–strain curve is observed, indicating fracture occurring at approximately 30% strain for both ratios.

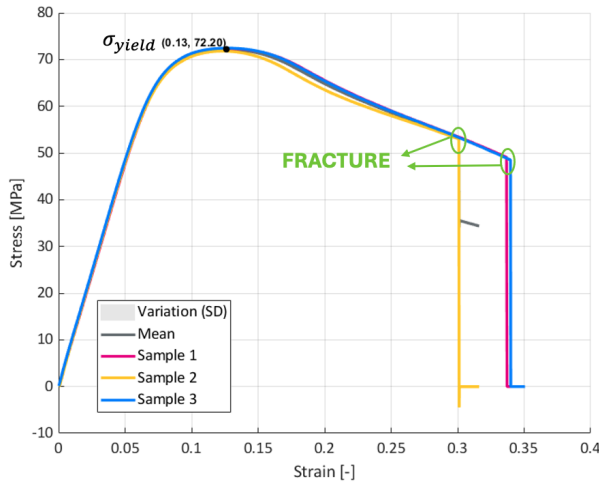


Figure 2.26 – Stress [MPa] vs Strain [-] for $c/t = 0.05.$

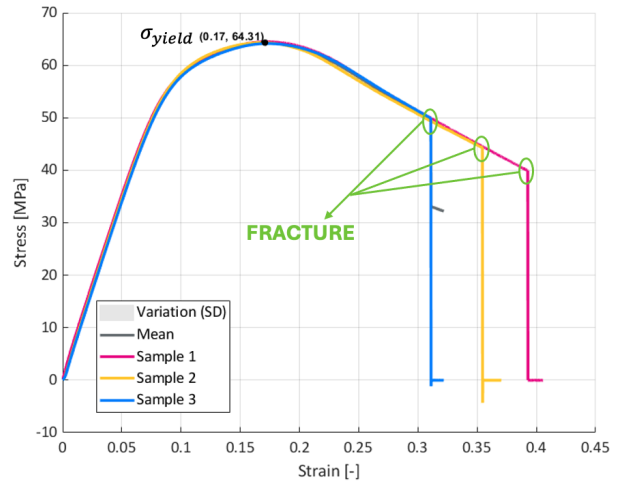


Figure 2.27 – Stress [MPa] vs Strain [-] for $c/t = 0.1.$

The videos reveal that both fractures are characterized by brittle failure, where both the shell and core fail completely, resulting in two distinct pieces. Pictures of both fractures are shown in Figure 2.28 and 2.29. Despite the similar failure behavior, the 0.05 ratio shows better yield strength and the same fracture strain, indicating superior mechanical performance compared to the 0.1 ratio.



Figure 2.28 – Sample 2 with $c/t = 0.05$ after fracture.

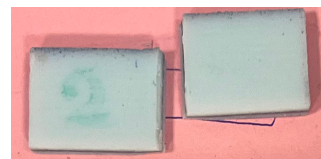


Figure 2.29 – Sample 2 with $c/t = 0.1$ after fracture.

For ratios $c/t = 0.2$ and $c/t = 0.4$, with intermediate size of soft core layer, the stress-strain curves, illustrated in Figure 2.30 and 2.31, exhibit a linear increase up to stress levels of 16.68 [MPa] and 14.17 [MPa] (point A), respectively. These values correspond to approximately 70% and 100% of the yield strength for the ratios of 0.2 and 0.4. Then, a sharp drop in stress is observed, indicating a significant loss in load-bearing capacity. Following this sudden drop, the stress-strain curve is shown to have a lower peak (point B), suggesting a partial recovery in the material's load-bearing ability. The curve then continues to increase until reaching the yield point (point C). For the ratio of 0.2, one sample experiences a second sudden drop (point D), while other samples with ratios of 0.2 and 0.4 exhibit a smoother drop. Another sample with a ratio of 0.2 then experiences an additional drop (point E).

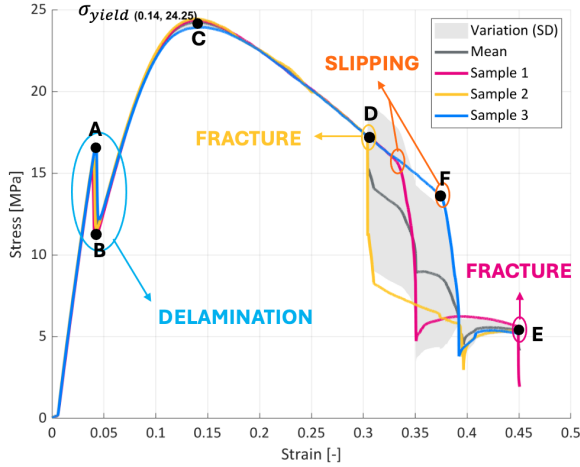


Figure 2.30 – Stress [MPa] vs Strain [-] for $c/t = 0.2$.

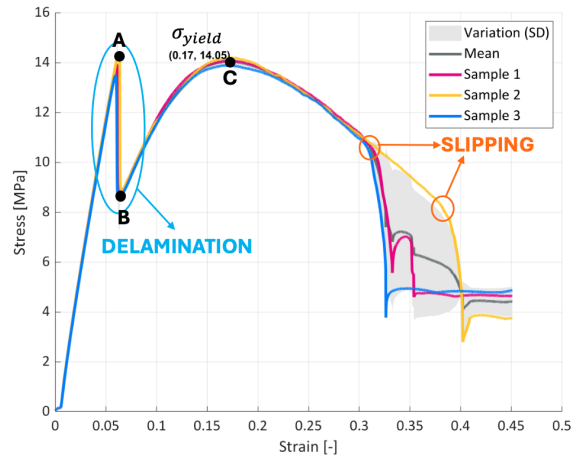


Figure 2.31 – Stress [MPa] vs Strain [-] for $c/t = 0.4$.

The initial drop in stress (point A) is attributed to delamination, a phenomenon involving interfacial cracking. Interfacial cracking occurs at the boundary between the hard shell and the soft core and is driven by shear stresses, characterized by fractures at the interface. These cracks propagate parallel to the sample's length, often caused by intrinsic incompatibilities between the layers, such as differences in mechanical behavior. Delamination typically initiates at the extremities of the sample due to compromised cohesive strength between the layers, which prevents the material from sustaining the same level of stress. It is also observed that the bottom layer of the shell disconnects from the core, while the bond between the top layer of the shell and the core remains intact. The partial recovery in load-bearing capacity after the initial stress drop (point B) is likely due to the redistribution of stresses within the remaining bonded regions or the core, which assumes more load as the outer layers delaminate. To address this issue, an alternative printing orientation is being investigated to minimize the incompatibilities that lead to delamination.

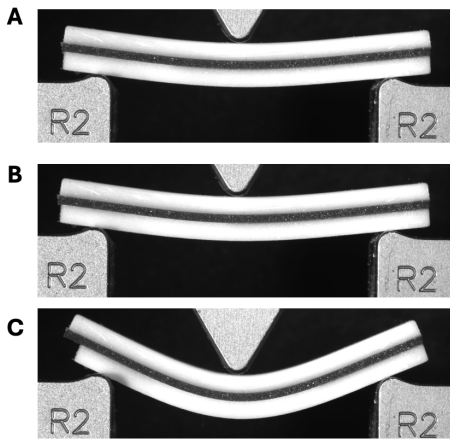


Figure 2.32 – Delamination progress at increasing strain for sample 1 with $c/t = 0.2$.

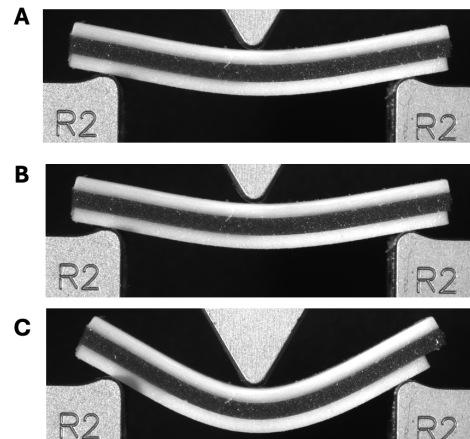


Figure 2.33 – Delamination progress at increasing strain for sample 1 with $c/t = 0.4$.

The second smooth stress drop (point F) observed is attributed to sample slipping, as confirmed by the videos. In this case, sample slipping always occurs at one of the extremities of the sample, as shown in Figure 2.34 (F). For the $c/t = 0.2$ ratio, two samples exhibit fractures (points D and E), marked by a sudden drop in stress, with one fracture occurring after slipping (point E). The fractures at points D and E are represented in Figure 2.34. Both fractures display similar behavior: the crack initiates from the bottom of the upper shell layer. It then propagates upward, perpendicular to the sample's length, through the top layer of the shell, and at the same time, propagates through the core which is no longer in contact with the bottom layer of the shell, leading to complete failure. Due to delamination, the bottom layer of the shell is no longer bonded to the core and does not support the load, it does not break.

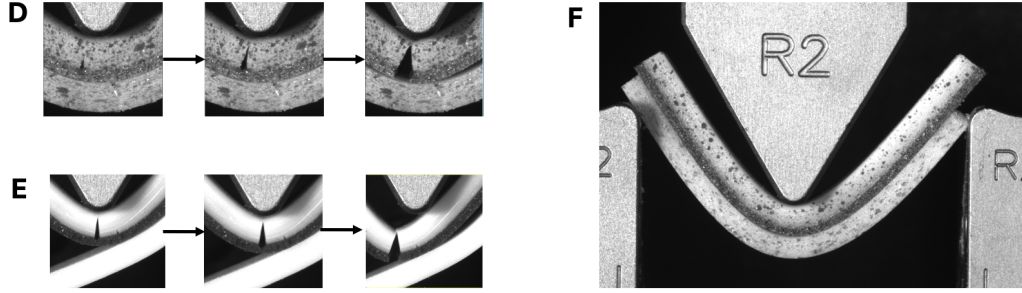


Figure 2.34 – Fracture progress at different increasing strain for sample 2 (E) and sample 1 (D) and slipping of sample 3 (F) with $c/t = 0.2$.

For the softer samples with ratios $c/t = 0.6$ and $c/t = 0.8$, the trends of the curves presented in Figures 2.35 and 2.36 are very similar to the curve of Shore95, but with higher yield strength and, consequently, better performance. This indicates that adding a thin outer layer of hard shell (VW+) enhances the mechanical performance compared to the monolithic material alone. Fracture occurs in only one sample with a ratio of $c/t = 0.8$, exhibiting the same characteristics as previous fractures seen for ratio $c/t = 0.2$, with crack propagation from the bottom of the sample to the top, perpendicular to the sample's length. However, compared to the failure behaviour of samples with a ratio of 0.05 and 0.1, which was completely brittle, in this case, the crack propagates slowly. The other samples with ratios of 0.6 and 0.8 all exhibit slipping.

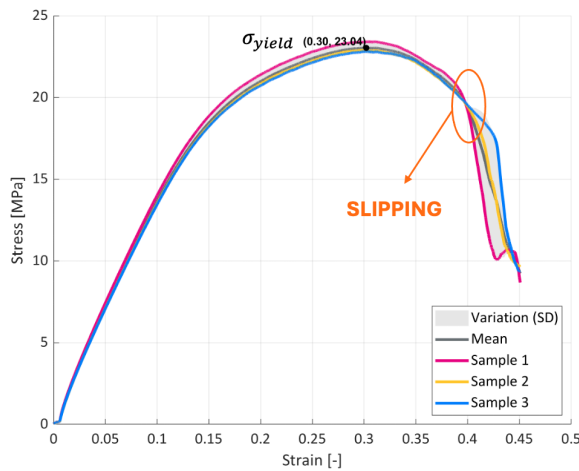


Figure 2.35 – Stress [MPa] vs Strain [-] for $c/t = 0.6$.

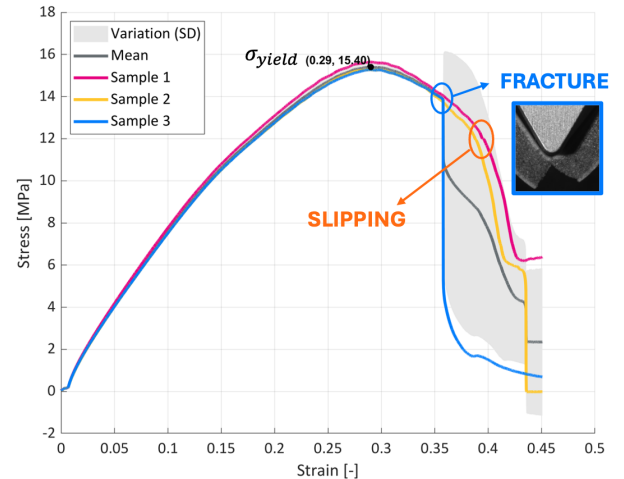


Figure 2.36 – Stress [MPa] vs Strain [-] for $c/t = 0.8$.

Figure 2.37 presents a summary of the stress-strain curves for all core-to-strut thickness ratios (c/t). The initial portion of the loading phase in these flexural stress-strain curves does not exhibit the same linear deformation. Upon exceeding the critical stress level (yield strength), the flexural stress decreases until either slipping or fracture occurs. The highest yield strength is observed for the ratio of 0.05, with a value of 72.20 [MPa], while the lowest yield strength is for the ratio of 0.4, with a value of 14.05 [MPa]. However, the sample with a ratio of 0.05 is also the first to fracture.

For core-to-strut thickness ratios above 0.4, catastrophic failure was not observed; instead, the struts exhibited slipping behavior. The tail end of the stress-strain curves for these ratios, featuring a plateau in stress, indicates that these struts have a higher energy absorption capacity under bending deformation.

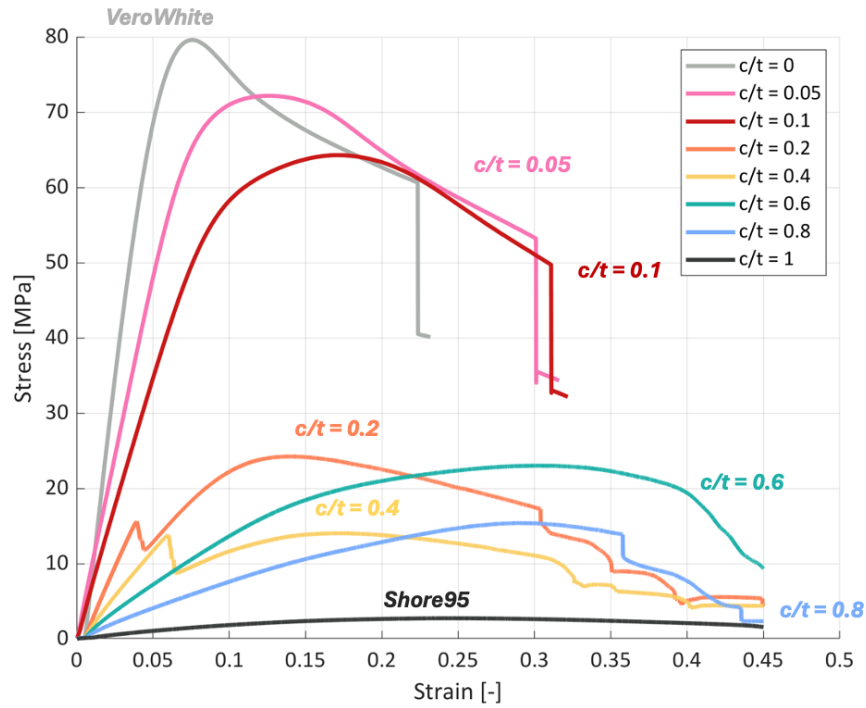


Figure 2.37 – Stress [MPa] vs Strain [-] for all ratios.

Two distinct failure modes are identified in the analysis of multi-layer materials: complete brittle failure and interfacial cracking. Complete brittle fracture occurs for ratios below 0.2 (specifically, 0.05 and 0.1), while interfacial cracking is observed for ratios of 0.2 and 0.4. Samples with a thinner soft core (ratios below 0.2) exhibit behavior similar to that of monolithic VeroWhitePlus, but their yield strength decreases as the core thickness increases. When the core thickness is further reduced, delamination occurs, leading to a significant drop in mechanical performance.

The stress-strain curves show a clear distinction between samples that experience fracture, which behave similarly to VeroWhitePlus, and those that experience delamination. The latter show much lower stress increases and have a plateau in their curves, which reflects a reduced capacity to bear load after initial delamination. This suggests that the mechanical performance of the struts decreases significantly once delamination initiates. In the initial portion of the curves, the stress gaps between different ratios are relatively uniform, but for samples that undergo delamination, the stress increase is notably lower compared to samples with ratios below 0.2.

2.2.3 Core-Shell configuration vs Core-Interface-Shell configuration

Mueller and his colleagues [28] demonstrated in their study on round beams that incorporating a softer interface between the core and the shell can enhance the mechanical performance of the sample. Specifically, they showed that for a large soft core with an inner diameter-to-beam diameter thickness ratio of 0.85, the shell fractures in a piecewise manner rather than in a brittle manner. Unlike lower ratios where cracks propagate straight through the shell, at this higher ratio, cracks are deflected and bifurcated. This deflection and bifurcation result in the formation of multiple new surfaces, allowing the shell to retain some stability and absorb more energy. Based on these findings, we investigated the addition of a soft interface made of TB, our softer material, across all ratios to determine if it produces a similar impact.

Stress-strain curves

The superimposed stress-strain curves shown in Figure 2.38, allow for a detailed comparison of the overall results across different configurations. Solid lines represent configurations without interfaces, while dashed lines indicate those with interfaces.

In both configurations, the addition of an interface does not significantly alter the overall shape of the stress-strain curves. Lower ratios still exhibit higher yield strengths. Intermediate ratios continue to show delamination, and higher ratios behave similarly to Shore95. It appears that adding an interface improves the yield strength, but this effect is observed only for a ratio of 0.2. For all other ratios, the curves show a decrease in yield strength when the softer layer is added.

Fracture is observed only for core-to-thickness ratios (c/t) of 0.2 and below, which contain a high proportion of brittle material. For ratios above 0.2, where the material becomes increasingly softer, progressive sliding of the sample occurs, sometimes preventing it from reaching the fracture point.

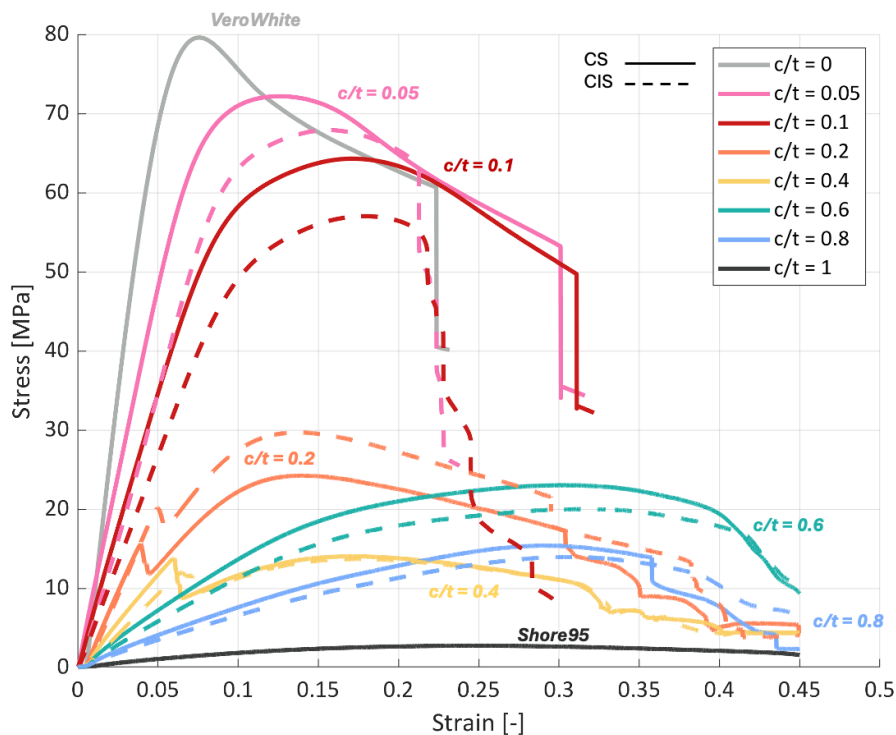


Figure 2.38 – Stress [MPa] vs Strain [-] for all ratios.

For both the 0.05 and 0.1 ratios, the addition of an interface layer reduces performances and slightly modifies the failure behavior. Indeed, the presence of the interface leads to a smoother and earlier drop in the stress-strain curve, indicating a less abrupt and earlier onset of failure. The stress drop after the failure strain is also less straight and sharp; instead, the decline resembles a wave-like curve with several minor fluctuations. Failure occurs at approximately 20% strain for both ratios, compared to 30% strain without the interface.

The failure phenomenon observed for both ratios is identical and is illustrated in Figure 2.39. Initially, the sample begins to delaminate as the load increases. At both extremities of the sample, the bottom layer of the shell starts to detach from the rest at the TB interface and tends to return to its original shape by shortening. Meanwhile, the upper part, with the core bonded to the upper shell layer, continues to elongate under the load. Subsequently, the bonded part starts to crack at the location of the unlinked section on the left, where the detachment becomes more pronounced. After fracture, the sample separates into two parts, as shown in Figure 2.41 and 2.40. The fracture is not a straight cut but rather a tear at the interface, with remnants of the interface material present on both sections.

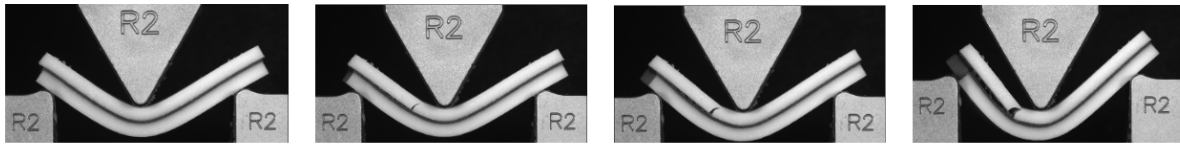


Figure 2.39 – Fracture progress at different increasing strain for sample with $c/t = 0.1$.

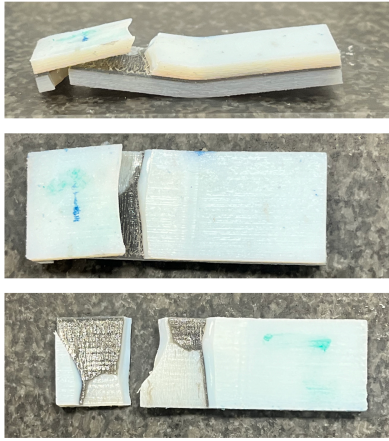


Figure 2.40 – Sample 1 with $c/t = 0.05$ after fracture.

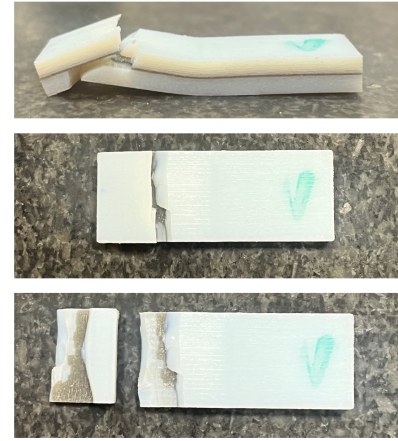


Figure 2.41 – Sample 1 with $c/t = 0.1$ after fracture.

For ratios of 0.2 and 0.4, the addition of a soft interface delays the onset of delamination, occurring slightly later, and improves performance after delamination for the 0.2 ratio and maintains similar performance for the 0.4 ratio. This indicates that the sample can support more load before delamination occurs. Without the soft layer, delamination occurs at 3.9% and 5.9% strain respectively for $c/t = 0.2$ and 0.4 versus 5% and 7% strain with interface. However, despite the delayed delamination, fracture of the sample occurs earlier for the 0.2 ratio. The failure mode is illustrated in Figure 2.42 and is similar to the failure observed in samples with a 0.2 ratio without the interface. The crack initiates from the bottom of the upper shell layer, propagates upward perpendicular to the sample's length through the top layer of the shell, and simultaneously progresses through the core, which is no longer in contact with the bottom layer of the shell, leading to complete failure. Due to delamination, the bottom layer of the shell is no longer bonded to the core, causing interfacial failure, and does not contribute to load support, it does not break. Therefore, unlike the smoother fracture behavior observed with the interface for ratios of 0.05 and 0.1, the failure phenomenon for the 0.2 ratio remains consistent with the behavior observed without the interface.

This suggests that while the addition of an interface can modify the fracture behavior, particularly by smoothing the failure process, it does not entirely prevent delamination or reduce the propensity for fracture in these multi-material struts.

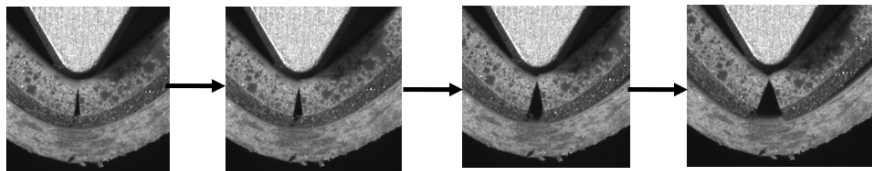


Figure 2.42 – Fracture progress at different increasing strain for sample with $c/t = 0.2$.

For samples with thicker layers of soft material, with ratios c/t of 0.6 and 0.8, the addition of a soft interface layer appears to slightly reduce performances. However, in contrast to the case without an interface, the sample with a ratio of 0.8 no longer exhibits failure. It is important to note that while only one sample did break, the curve represents the average of three curves, including the fracture data.

Effective Modulus

The experimental variation of the flexural modulus was compared to theoretical values as a function of the core-to-strut thickness ratio (c/t), following a method similar to that used by Yavas [29]. The results of Yavas are presented in Figure 2.43. The blue line represents analytical results calculated using the Euler-Bernoulli equation based on standard beam theory, as detailed in the Methods section. The green line represents the experimental data.

Our results are illustrated in Figure 2.44, solid points indicate samples without interfaces (C-S), while dashed points indicate those with interfaces (C-I-S). For the experimental results, the slope of the linear portion of each stress-strain curve, where Hooke's law is applicable, was used to determine the flexural modulus. The same formula used by Yavas was applied to calculate the theoretical values. It is also important to note that, in the theoretical formula, we used the experimental Young's moduli for Shore95 and VeroWhitePlus to achieve a more comparable and readable graph.

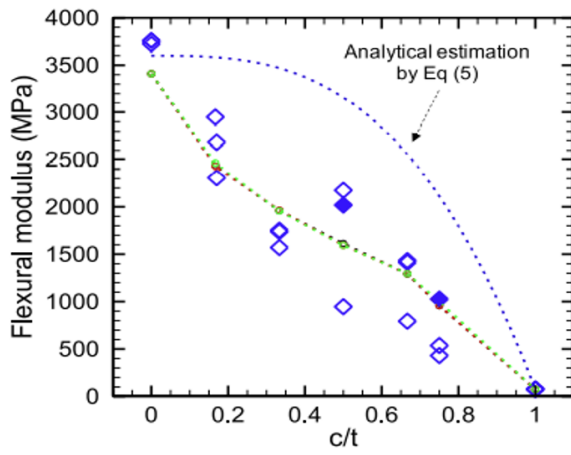


Figure 2.43 – Effective Modulus vs ratios from Yavas [29].

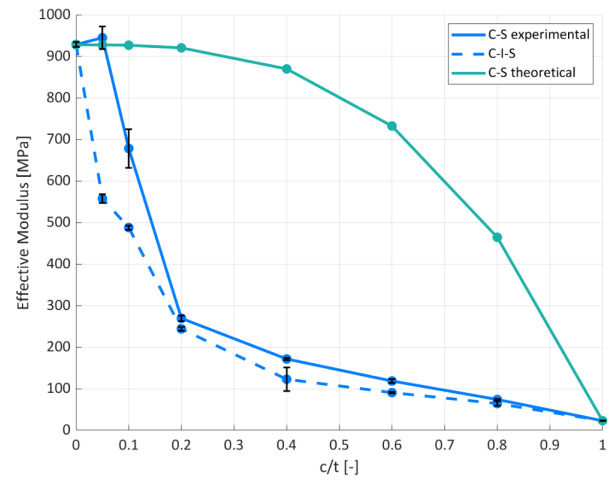


Figure 2.44 – Effective Modulus [MPa] vs ratios.

Although Yavas used different polymers in his experiments, making the absolute values not directly comparable, the trend of the curves is comparable. Our results show a trend similar to Yavas' findings.

As expected, the flexural modulus decreases gradually as the core-to-strut thickness ratio (c/t) increases. This decrease is due to the higher proportion of the more flexible core material, which reduces the overall stiffness of the structure. However, the experimentally observed decrease is significantly steeper than the variation predicted by the standard beam theory, indicating that the analytical estimates overestimates the flexural modulus of the multi-material struts, as Yavas also concluded.

Yavas et al. [29] proposed two plausible explanations for this discrepancy. First, standard beam theory assumes perfectly elastic behavior for both core and shell materials, which is not entirely accurate in this case. Shore95, being a rubber-like material, exhibits highly hyperelastic behavior, capable of undergoing large deformations. Second, the standard beam theory does not account for shear deformation's contribution to the measured stiffness, which is significant in our case. Additionally, the large modulus mismatch between the core and shell materials ($E_{VW}/E_{Shore95} = 43.75$) could further contribute to the observed discrepancy.

When comparing the experimental flexural modulus between C-S and C-I-S configurations, it is observed that for all c/t ratios, the modulus is consistently slightly higher in the absence of an interface, although both curves follow the same overall trend. An exception occurs at a ratio of 0.05 and 0.1, where a noticeable gap is observed. This gap correlates with the significant difference in slope in the initial linear portion of the stress-strain curves when an interface is present at this ratio. Notably, in the absence of an interface, the flexural modulus at a ratio of 0.05 slightly exceeds that of the monolithic VeroWhitePlus material, indicating superior performance compared to the monolithic structure.

Yield strength

Next, the yield strength for all ratios is plotted in the graph shown in Figure 2.45. The highest yield strength is achieved with a 0.05 ratio with or without interface. Material softening results in a decrease in yield strength, which reaches a minimum at a 0.4 ratio, regardless of the presence of an interface. Subsequently, yield strength peaks at a 0.6 ratio before declining once more. The percentages represent the percentage of improvement or decline of the sample without an interface compared to the sample with an interface. The introduction of a soft layer of TB+ enhances the yield force only at ratios of 0.2, with the yield strength improving the most, by up to 25% compared to a sample without an interface.

In contrast, Mueller's study [28] on round beams identified a more continuous decline in yield strength as core thickness increased. For small core-to-strut thickness ratios, the yield strengths of configurations with and without an interface were comparable, with the interface addition leading to slightly lower values. However, when the core-to-strut thickness ratio reached 0.5, the disparity between configurations became more pronounced. At this point, the presence of an interface significantly reduced performance.

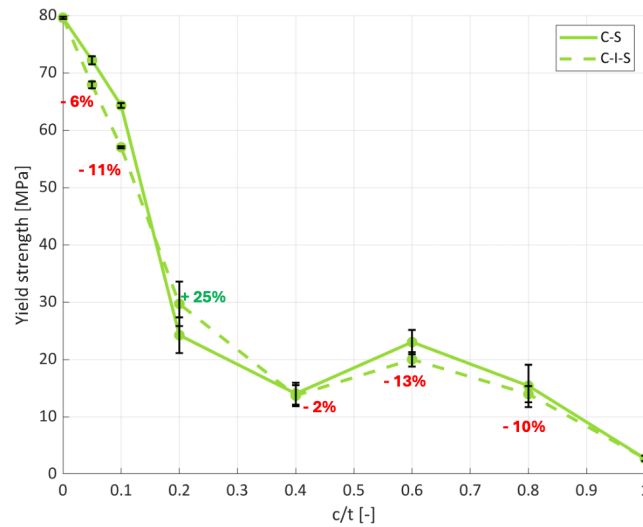


Figure 2.45 – Yield strength [MPa] vs ratios.

Energy Absorption

As previously noted in the Methods section, energy absorption was computed in two ways, represented in Figure 2.46: (1) up to the deformation point where the first sample slid (27.5% deformation for the 0.4 ratio sample), illustrated by the pink curve and (2) up to individual critical points for each sample, with energy calculated to fracture for fractured samples and to slip points for slipped samples, represented by the purple curve. Overall, both curves exhibit similar trends, so only one curve could be analyzed.

For lower ratios with thin soft cores, a substantial gap between the performance between C-S and C-I-S is observed. Without the interface, energy absorption increases by approximately 30% from pure VeroWhitePlus to the ratio of 0.05. In contrast, with the interface, starting from VeroWhitePlus, energy absorption decreases markedly but in a continuous manner. Regardless of the interface, the curve then, reaches a minimum at a ratio of 0.4, with a decrease of 70% compared to the pure monolithic VW+ beam. After that, it increases again until 0.6 and before decreasing.

Consequently, the greatest performance reductions are observed for thin soft cores, with reductions of 33% and 37% for ratios of 0.05 and 0.1, respectively, when the interface is added. This can be explained by the fact that, as previously observed, the addition of the interface leads to earlier interfacial failure due to delamination, even though the fracture process becomes smoother. Without the interface, the material absorbs energy more effectively because the fracture is more brittle and occurs after the material has reached its maximum potential for energy absorption. In contrast, with the interface, although the failure process is smoother and the material retains some surface area to absorb energy, delamination limits the material's

ability to utilize its full energy absorption potential. As a result, less energy is absorbed before fracture occurs, and the fracture happens earlier.

As the material is softened, the trend reverses, and performance improvement with the interface becomes evident only for a ratio of 0.2, showing a 17% increase in yield strength. This is because, at a ratio of 0.2, adding an interface does not alter the failure mode significantly and delays the onset of delamination. This delay allows more energy to be absorbed initially, leading to higher yield strength and energy absorption.

For ratios above 0.2, performance without the interface is slightly poorer, but the results remain comparable. Consequently, adding a soft layer to a material with a thicker soft core makes it more compliant, allowing it to support more load through increased deformation. However, this addition does not improve performance, as the material simply deforms more without enhancing its overall strength. This is also due to the fact that introducing the interface reduces the thickness of the shell, and consequently the amount of VeroWhitePlus material. This reduction in VeroWhitePlus decreases the contribution of its brittle properties to the overall performance.

Mueller's study on round beams [28] observed a similar pronounced gap, but this effect was not evident at lower ratios but higher ones. For ratios above 0.6, there was a divergent trend between configurations with and without an interface: a thick, soft core significantly reduced energy absorption, whereas the addition of an interface markedly improved it. At a ratio of 0.85, adding an interface considerably improves performances, doubling the energy absorption of the shell.

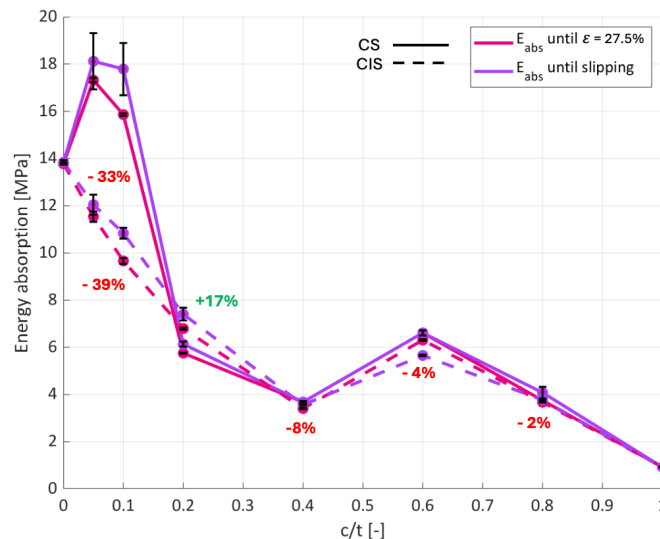


Figure 2.46 – Energy Absorption [-] vs ratios.

Energy Absorption Efficiency

To better understand the energy efficiency of each sample with different ratio, the energy absorption efficiency (EAE) was calculated and the curves obtained are illustrated in Figure 2.47.

The overall behavior with variations in the ratio appears somewhat inconsistent. However, the efficiency values are relatively close and high, ranging from 68% for the lowest efficiency to 80% for the highest. None of the samples achieved 100% efficiency.

A lower peak efficiency is observed for the softer multi-layer material for a ratio of 0.8, with a 12% decline compared to pure VW+ efficiency. Whereas the highest performance is achieved for a ratio of 0.4 but only with an increase of 2% compared to pure VW+. This indicates that the sample with a medium thickness of soft core is more effective at absorbing energy relative to its theoretical maximum potential compared to the other samples. In contrast, the sample with a ratio of $c/t = 0.8$ does not approach its maximum potential as closely.

Observations indicate that for high ratios, EAE is slightly improved with the addition of an interface. Con-

versely, for medium ratios, there is a slight decrease in efficiency. Therefore, adding a soft interface allows softer materials to approach their full energy absorption potential, thereby making them more efficient. For small ratios, significant differences remain evident with a maximum decrease of 7% compared to the case without interface for a ratio of 0.1, consistent with our previous observations.

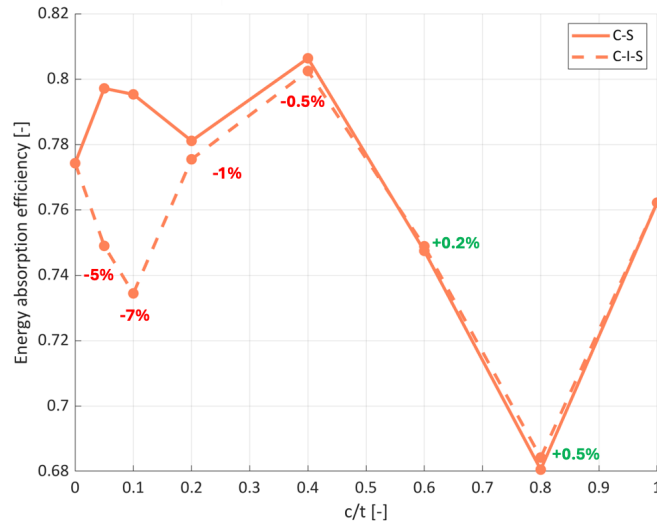


Figure 2.47 – Energy Absorption efficiency [-] vs ratios.

Digital Image Correlation

As detailed in the Methods section, Digital Image Correlation (DIC) was employed to analyze all C-S and C-I-S samples, providing comprehensive data on the displacement and strain distribution within the material during deformation. DIC was conducted on samples at a slight deformation beyond the initial state, specifically within the linear region of the deformation curve to ensure the accuracy of the results. This section presents the results for the three strain distributions observed. The displacement fields are not included in the thesis because the displacement fields exhibited consistent patterns across all samples, which did not add significant value to the analysis and thus, did not contribute meaningfully to the study's objectives. In each set of figures, panel (a) shows the results for the pure VeroWhitePlus beam, panels (b) and (d) present the results for all ratios in C-S configurations, panels (c) and (e) depict the results for all ratios in C-I-S configurations, and panel (f) illustrates the results for the pure Shore95 beam.

For ϵ_{xx} , results are shown in Figure 2.48 and 2.49. For the pure monolithic VW+ beam, significant stretching is observed in the top region, while maximum compression is concentrated at the bottom. This pattern is typical of bending behavior in homogeneous materials.

Introducing a Shore95 core notably alters the strain distribution. Although the strain distribution remains similar to that of the VW+ beam, it becomes localized to the shell region. Within the core, stretching is observed at the extremities, with nearly zero strains in the middle.

As the core-to-thickness ratio increases, the strain distribution across the beam's shell becomes more uniform. We observed that a softer core increasingly suppresses the hard shell's behavior, particularly at a ratio of 0.8. In the core, there is growing compression in the middle and stretching at the extremities, with these effects becoming more concentrated as the core-to-thickness ratio increases. Consequently, while the strain behavior within the core becomes more localized and concentrated, the strain distribution in the shell becomes more balanced. As the flexible interior layer's behavior becomes more dominant, the composite beam's overall response changes. The introduction of the Shore95 core increases compliance, balancing the strains along the shell while accentuating its own behavior. Compared to a pure Shore95 beam, the composite beam with a higher content of soft materials shows more pronounced strain within the core, rather than at the top and bottom faces. Thus, the presence of the shell maintains a stiffer exterior, while the core absorbs more of the deformation.

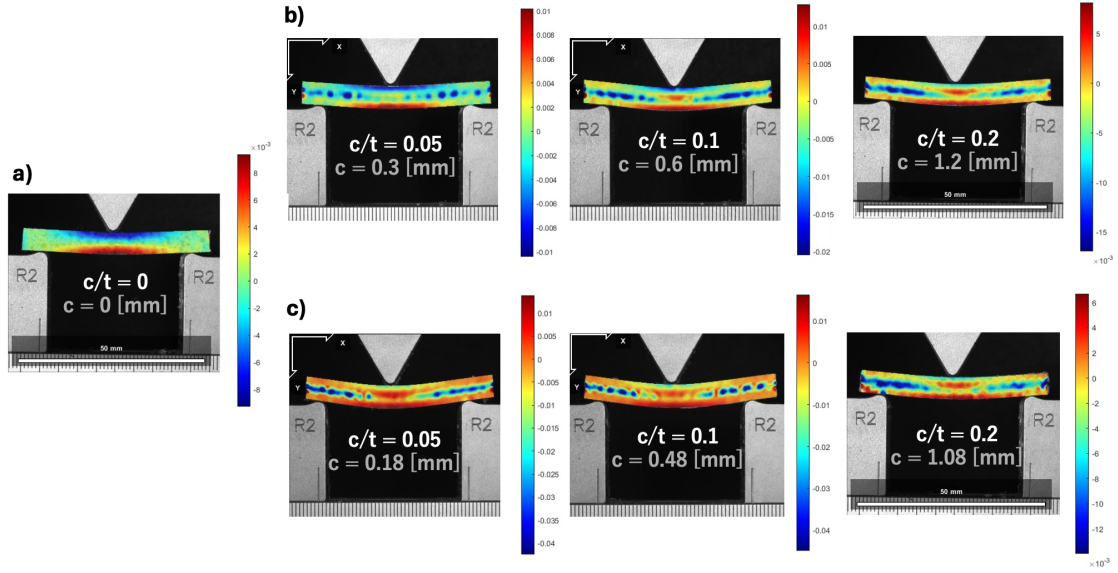


Figure 2.48 – ϵ_{xx} strain map for ratios a) $c/t = 0$, b) $c/t = 0.05, 0.1$ and 0.2 for C-S configuration and c) $c/t = 0.05, 0.1$ and 0.2 for C-I-S configuration.

The addition of an interface layer results in a less intense overall strain field. The stretching (red) becomes more evenly distributed, covering almost the entire shell region, while the compression at the bottom is significantly reduced, allowing more room for stretching.

Consequently, the introduction of the interface layer facilitates a smoother transition of strain between the core and shell, helping to distribute the tensile strain more effectively across the shell. Additionally, the compression is more efficiently managed by the combined action of the core and interface layer, leading to a more balanced strain distribution overall.

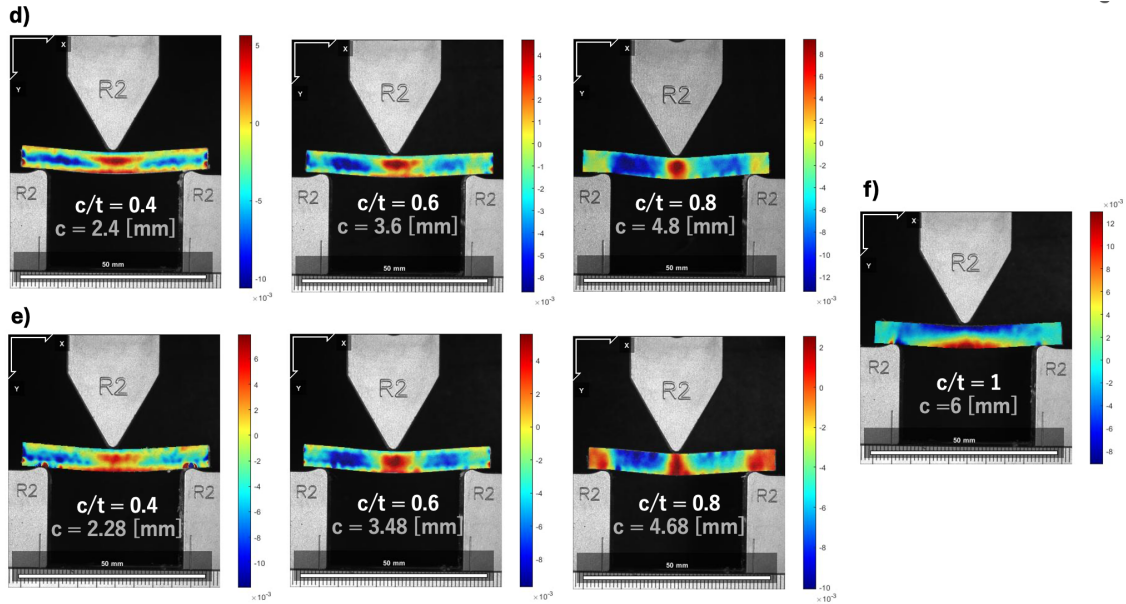


Figure 2.49 – ϵ_{xx} strain map for ratios d) $c/t = 0.4, 0.6$ and 0.8 for C-S configuration, e) $c/t = 0.4, 0.6$ and 0.8 for C-I-S configuration and f) $c/t = 1$

For ϵ_{xy} , results are shown in Figure 2.50 and 2.51. For the pure VW+ beam, shear strain is concentrated around the loading point and along the beam's thickness, exhibiting alternating regions of positive and negative strain. In contrast, in the composite beam, shear strain is predominantly localized within the core, with the VW+ hard shell experiencing almost no strain. As the soft core's thickness increases, the shear effect becomes more pronounced, though the same localized pattern is maintained. This concentration

of shear within the core sharply contrasts with the more distributed, less significant deformation typically observed in homogeneous materials.

This behavior suggests that the structure effectively isolates shear within the internal core, preventing significant transmission of shear forces to the outer shell. This isolation implies a higher degree of strain energy absorption within the core, which could be advantageous for applications requiring localized energy dissipation, such as impact mitigation. Additionally, the consistent deformation patterns indicate a robust design, ensuring the material's response remains stable even as the core thickness changes.

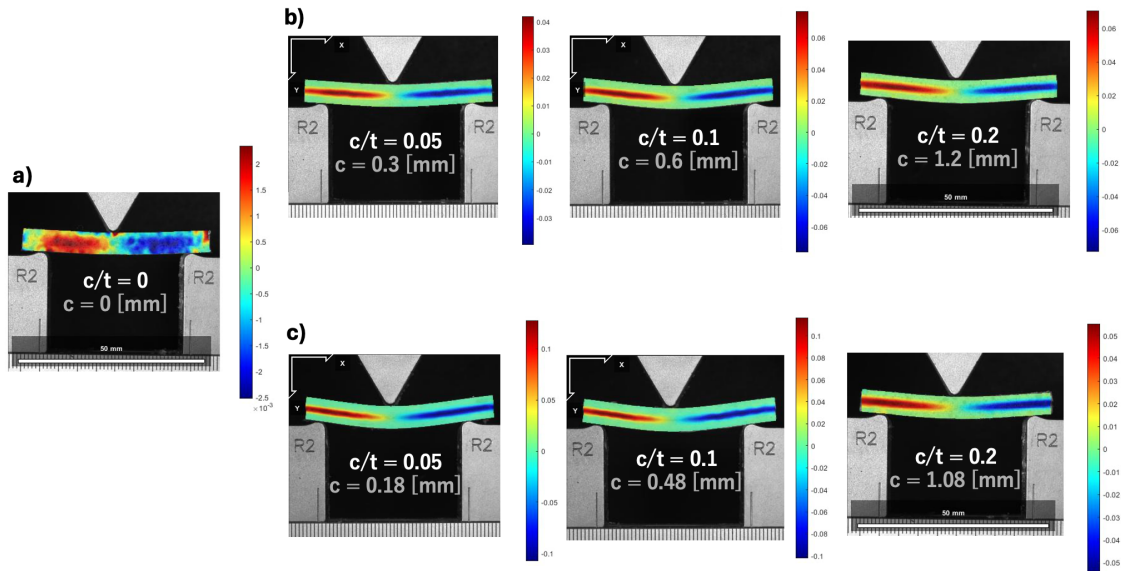


Figure 2.50 – ϵ_{xy} strain map for ratios a) $c/t = 0$, b) $c/t = 0.05, 0.1$ and 0.2 for C-S configuration and c) $c/t = 0.05, 0.1$ and 0.2 for C-I-S configuration.

The addition of an interface layer produces similar deformation patterns but increases the internal thickness due to the added layer of compliance. This added layer allows for smooth diffusion and transition of strain between the core and interface, resulting in a continuous and uniform strain distribution without significant differences. The interface thus enhances the material's ability to manage strain effectively, contributing to a more seamless and cohesive structural response.

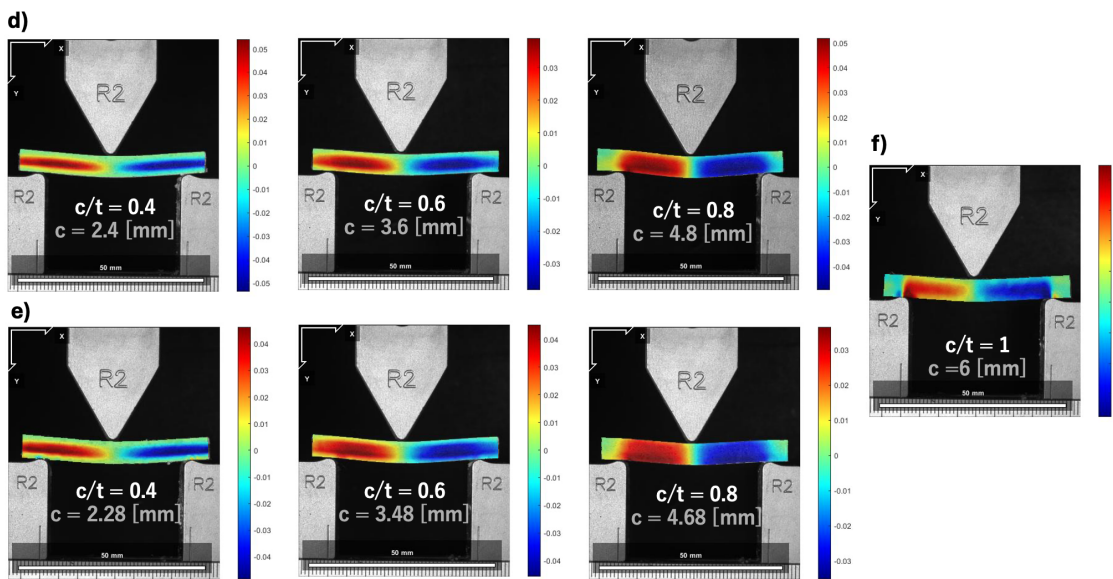


Figure 2.51 – ϵ_{xy} strain map for ratios d) $c/t = 0.4, 0.6$ and 0.8 for C-S configuration, e) $c/t = 0.4, 0.6$ and 0.8 for C-I-S configuration and f) $c/t = 1$

For ϵ_{yy} , results are shown in Figure 2.52 and 2.53. As the layer thickness increases, the addition of an interface leads to more pronounced stretching, as indicated by the blue regions. This is consistent with the introduction of a flexible layer, which enhances the material's ability to stretch. As the core-to-strut thickness ratio increases, the deformation distribution increasingly resembles that of Shore95, characterized predominantly by material compression.

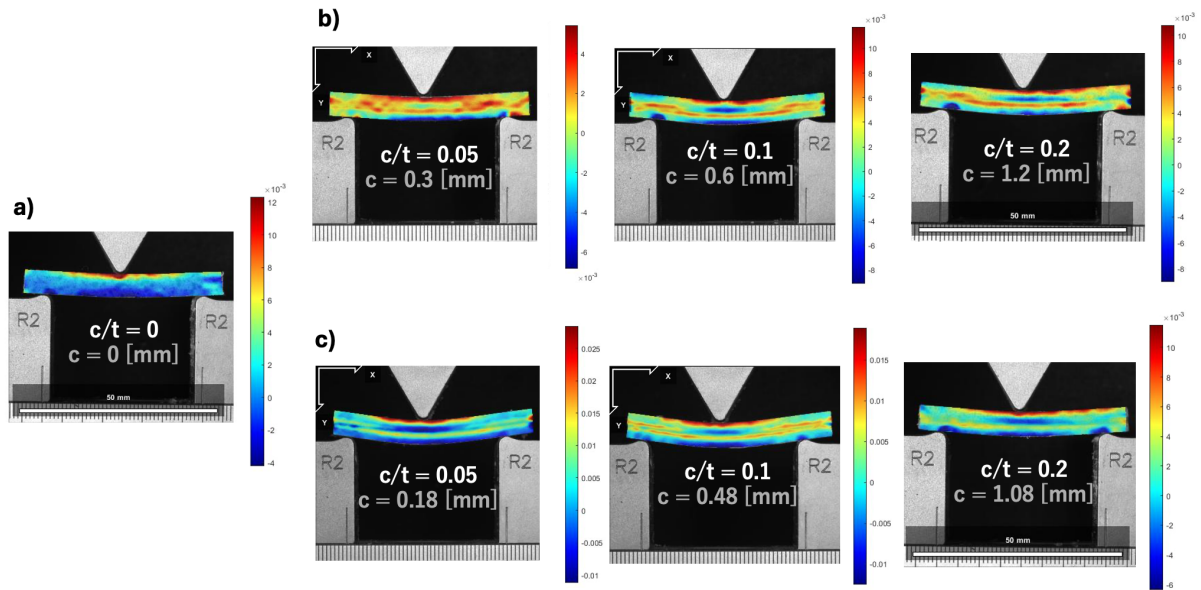


Figure 2.52 – ϵ_{yy} strain map for ratios a) $c/t = 0$, b) $c/t = 0.05, 0.1$ and 0.2 for C-S configuration and c) $c/t = 0.05, 0.1$ and 0.2 for C-I-S configuration.

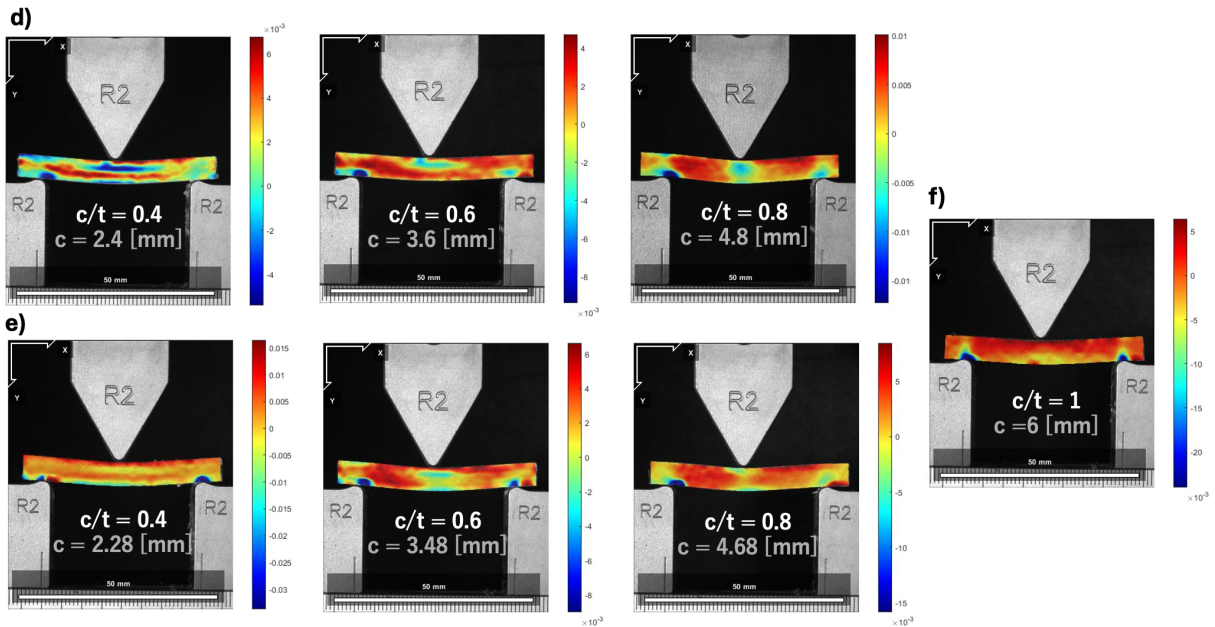


Figure 2.53 – ϵ_{yy} strain map for ratios d) $c/t = 0.4, 0.6$ and 0.8 for C-S configuration, e) $c/t = 0.4, 0.6$ and 0.8 for C-I-S configuration and f) $c/t = 1$

2.2.4 Printing orientation

The delamination observed at ratios of 0.2 and 0.4 significantly impaired performance, capturing considerable attention and curiosity. To address this issue, the potential influence of printing orientation on interface formation was investigated, following the approach studied by Laura Zorzetto. Her research demonstrated

that interfaces are sharp in horizontally printed samples and blurred in vertically printed samples. Additionally, her study reveals that it could introduce some shear stresses phenomenon, which is our case.

To further explore the impact of printing orientation, all samples with different ratios were reprinted in a vertical orientation and compared to those printed horizontally. Given that the inclusion of a soft interface consistently degraded mechanical properties, this layer was excluded from subsequent analyses. The remaining properties—stress-strain curves, yield strength, and energy absorption capacity—were evaluated. The minimal variation observed between samples affirmed the reliability of the results.

Stress-strain curves

First, stress-strain curves were computed. In all graphs, solid lines represent the behavior of samples printed horizontally (along xy), while dashed lines represent samples printed vertically (along xz).

To begin with, the stress-strain curves for the pure monolithic samples of VeroWhitePlus and Shore95, shown in Figure 2.54, reveal similar behaviors. For VeroWhitePlus, fracture onset occurs later when printed vertically, with approximately 5% more crosshead displacement before failure; however, the yield strength is slightly lower. For Shore95, both curves exhibit similar features across all parameters. This similarity in pure monolithic samples facilitates the comparison of the composite samples.

For lower ratios of $c/t = 0.05$ and 0.1 , shown in Figure 2.55 the observed behavior differs between the case printed horizontally and vertically. In both cases, failure occurs earlier, and the yield strength is lower when printed vertically. For the ratio of 0.1 , despite weaker performance, the curve follows the trend of VeroWhitePlus with the failure mode remaining a brittle fracture. In contrast, the sample with a ratio of 0.05 exhibits delamination as the failure mode, resulting in smooth degradation with multiple drops in the stress-strain curve whereas in the horizontal case, brittle fracture was observed. The final oscillations in the curve indicate sample slipping. Delamination, illustrated in Figure 2.56, significantly weakens the sample's performance. As with previous observations, delamination begins at the extremity (on the left) where the bottom layer of the shell starts detaching from the upper part.

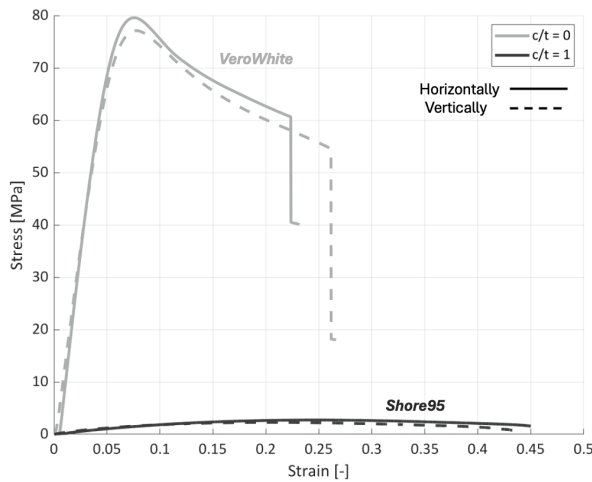


Figure 2.54 – Stress [MPa] vs Strain [-] curves for $c/t = 0$ and 1 .

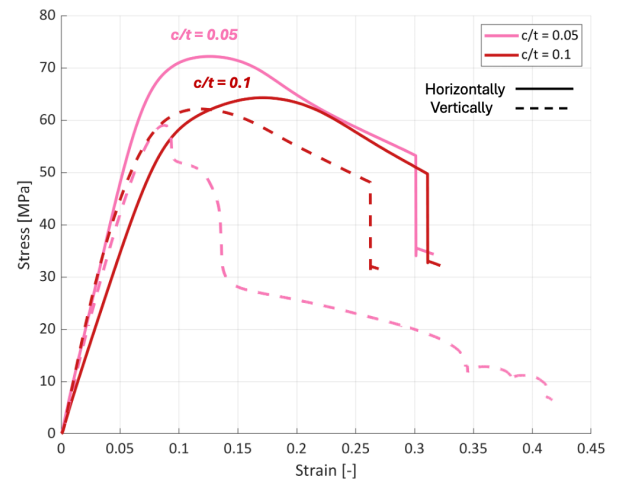


Figure 2.55 – Stress [MPa] vs Strain [-] curves for $c/t = 0.05$ and 0.1 .

However, it should be noted that the behavior of the stress-strain curve during delamination in this case differs from that observed for samples printed horizontally with a c/t ratio of 0.2 . In the latter case, the curve exhibited a slight drop in stress followed by a subsequent increase, suggesting a partial load recovery by the remaining bound material. In contrast, the current case does not show any such load recovery. Instead, the stress continuously decreases without rising, indicating that the remaining material is no longer capable of sustaining the applied load.

Despite a 0.05 ratio indicating a very thin Shore95 layer that should theoretically align closely with VeroWhitePlus, this is not observed. In the vertical orientation, the interface blends with the surround-

ing material, suggesting that the thin layer should integrate well with VeroWhitePlus compared to thicker layers. This behavior indicates the existence of a potential threshold effect, where adding a soft layer below a certain thickness significantly deteriorates the sample's properties. However, for both ratio, it is observed that printing the samples vertically decreases the mechanical performances.

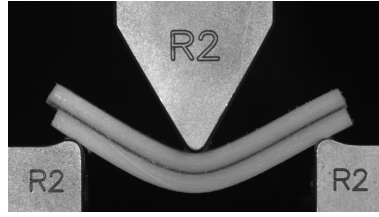


Figure 2.56 – Delamination for $c/t = 0.05$.

For intermediate ratios of $c/t = 0.2$ and 0.4 , as illustrated in Figure 2.57, no delamination is observed anymore. Additionally, the yield strength of these samples is significantly higher, with their stress-strain curves following a trend similar to that of more brittle materials, such as pure VeroWhite, resulting in a brittle fracture. Specifically, for the ratio of 0.2 , the fracture occurs later when the samples are printed vertically. In contrast, for the ratio of 0.4 , originally, no fracture was observed when the samples were printed horizontally. However, overall, it is observed that printing the samples vertically enhances their mechanical performance for both ratios.

For higher ratios of $c/t = 0.6$ and 0.8 , as illustrated in Figure 2.58, the stress-strain curves exhibit distinct differences depending on the printing orientation. When printed horizontally, the behavior of these samples is more similar to that of Shore95. However, when the orientation is changed, the behavior shifts closer to that of a brittle material, despite the higher content of soft material. Indeed, it is observed that both samples fractured, with the initial slope of the stress-strain curve being higher. For a c/t ratio of 0.6 , the difference between printing orientations is notably pronounced. Specifically, samples with a vertical printing orientation exhibit a higher yield strength, resulting in a stress-strain curve that is shifted upward and to the left. This shift indicates that the material behaves more brittly and can support a greater load before reaching its yield strength. In contrast, for a c/t ratio of 0.8 , the distinction between the orientations becomes less apparent. The samples display a blend of brittle and ductile characteristics. The yield strength is observed to be lower compared to the $c/t = 0.6$ samples, and there is a slight reduction in stress just prior to fracture.

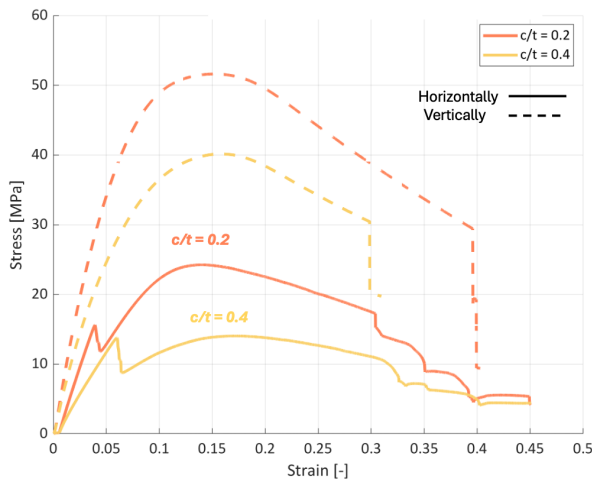


Figure 2.57 – Stress [MPa] vs Strain [-] curves for $c/t = 0.2$ and 0.4 .

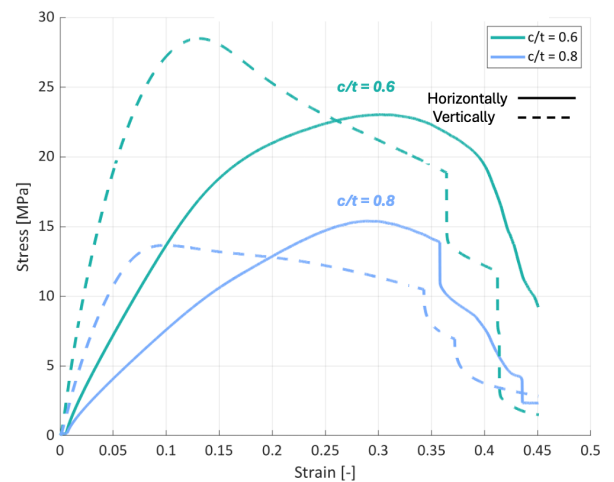


Figure 2.58 – Stress [MPa] vs Strain [-] curves for $c/t = 0.6$ and 0.8 .

In the following Figures, all stress-strain curves for the different c/t ratios are superimposed to facilitate a comparison of overall material behavior and to assess any improvements or degradations. Figure 2.59

illustrates the stress-strain behavior of samples printed horizontally, while Figure 2.60 presents the behavior of samples printed vertically.

Upon examining the general stress-strain curves for the xz orientation, it is observed that the decline between curves is smoother and more uniformly distributed. Initially, all curves exhibit similar behavior, characterized by a linear increase and following the VeroWhitePlus trend. However, there is a noticeable reduction in the initial slope as the content of the softer material increases. Following the yield strength, all curves, with the exception of the $c/t = 0.05$ ratio, show a stress drop before reaching fracture. A possible explanation is that, as the samples receive increased UV exposure and additional layers—given their vertical printing orientation—they tend to exhibit more brittle behavior, like VeroWhitePlus.

Notably, the behavior of the $c/t = 0.5$ ratio is distinct from the others, as it demonstrates delamination without fracture, unlike the other ratios which exhibit fracture. Additionally, the $c/t = 0.05$ ratio fails significantly earlier compared to the other ratios showing that delamination adversely affects its performance.

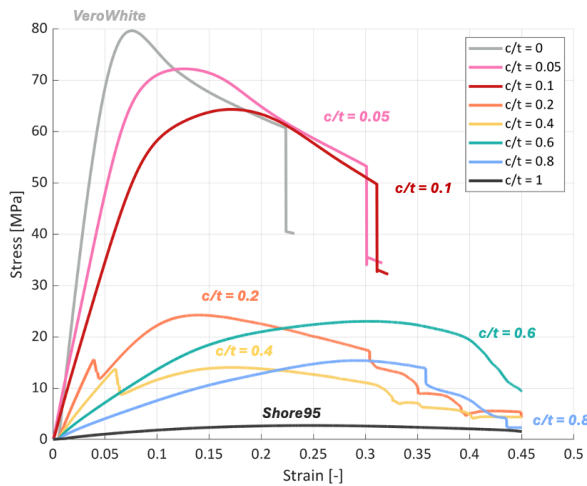


Figure 2.59 – Stress [MPa] vs Strain [-] curves for xy-oriented printed samples.

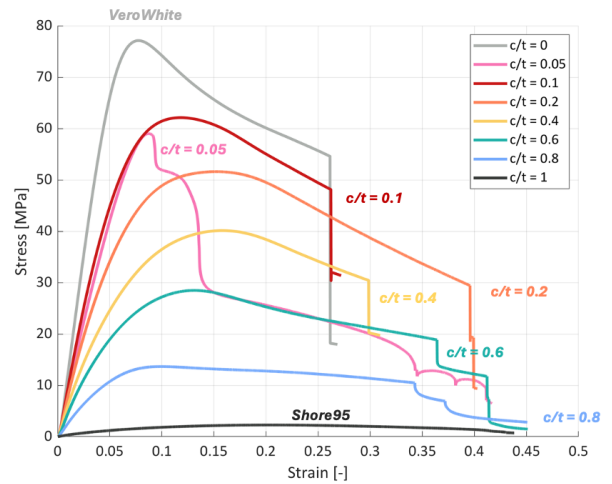


Figure 2.60 – Stress [MPa] vs Strain [-] curves for xz-oriented printed samples.

Yield Strength

The yield strength versus ratio data, presented in Figure 2.61, reveals that, despite a minimum peak observed at the thinner ratio, the curve trend remains notably continuous and linear for samples printed along the xz orientation. Fewer oscillations are observed in this case.

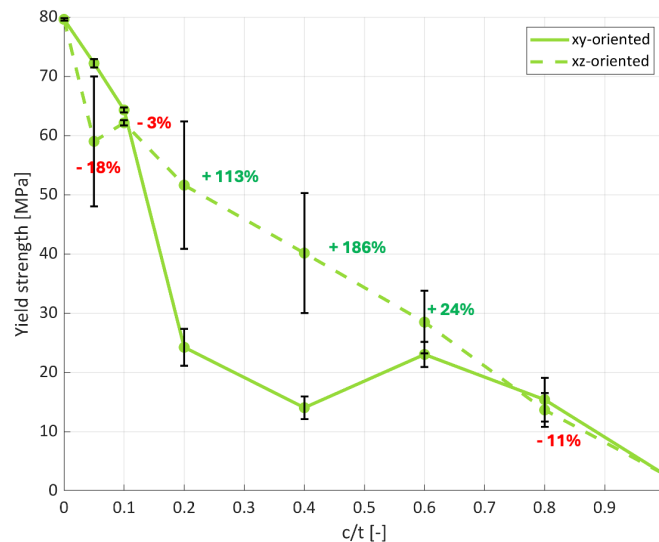


Figure 2.61 – Yield Strength [MPa] for all ratios.

Indeed, a maximum decline in performance of 18% is observed for a c/t ratio of 0.05 when printed vertically compared to horizontally. This percentage indicates the relative decline or improvement in yield strength of the vertically printed sample compared to the initially horizontally printed sample. Compared to the yield strength of the pure VW+ beam, there is a decrease of 33%. This observation is consistent with our previous findings, where delamination occurring at a c/t ratio of 0.05 was shown to reduce performance. For a c/t ratio of 0.1, although vertical printing still results in poorer performance, the decrease is minimal at 3%.

As the ratio increases, the yield strength improves when printed vertically, achieving a maximum enhancement of 186% for a c/t ratio of 0.4. Again, this observation aligns with the disappearance of the delamination phenomenon observed, enhancing material behavior.

Following this maximum, further enhancement is still observed with vertical printing for a c/t ratio of 0.6, although the percentage of enhancement is reduced. For a c/t ratio of 0.8, the trend reverses, showing a small improvement of 11% when printed horizontally.

Energy Absorption

Energy absorption was calculated as previously. The pink curves in Figure 2.62 represent the energy absorbed up to the point of initial slipping, while the purple curves illustrate the energy absorbed at each individual slipping point.

The results indicate that, for smaller ratios and thinner soft layers, a horizontal printing orientation is more advantageous. For a c/t ratio of 0.05, there is a substantial decrease in performance, with energy absorption dropping by nearly 50%. This significant decline is attributed to delamination, which detaches the lower shell layer, reducing the surface area available for energy absorption and leaving less material to support the load. Consequently, the material experiences a rapid delamination process, limiting its capacity to absorb energy. While we had an approximately 30% increase compare to the pure monolithic stiff material for the horizontally printed 0.05 ratio sample, here an approximate 35% decline is observed. In contrast, for a c/t ratio of 0.1, the material remains intact longer before complete failure, allowing it to utilize its full energy absorption potential and resulting in only a minimal decline of 7%, as previously observed for yield strength.

As the ratio increases, energy absorption performance improves with vertical printing, nearly doubling for a ratio of 0.4. This finding is consistent with observations regarding yield strength and highlights the significant performance enhancement achieved by eliminating delamination.

For higher ratios, while energy absorption remains better with vertical printing, the percentage of improvement decreases. This confirms that, although the influence of printing orientation on performance diminishes with increased ratio, it still provides a measurable benefit.

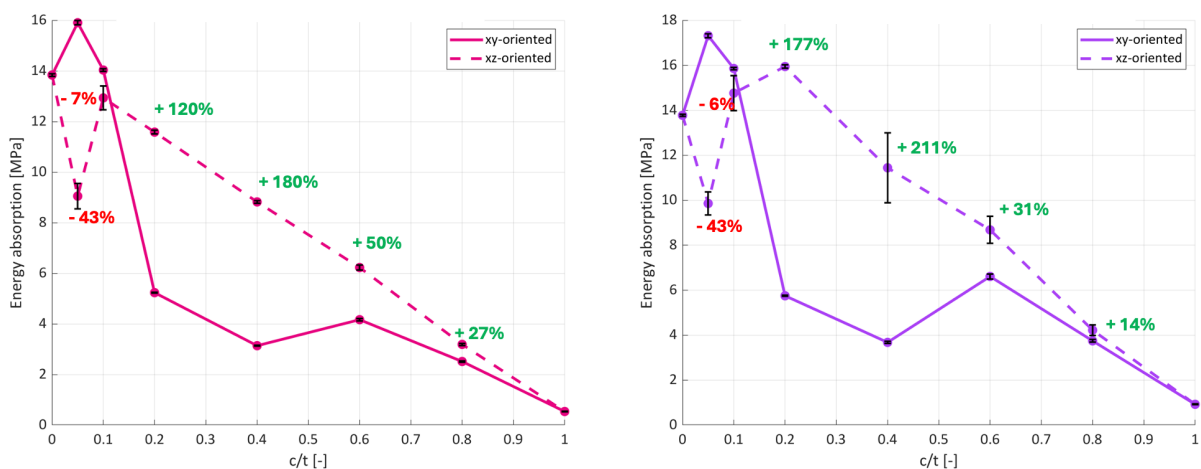


Figure 2.62 – Energy Absorption [MPa] for all ratios.

2.3 Conclusion

In summary, multi-layer beams configured as sandwich structures were designed and fabricated using PolyJet 3D printing. These beams consist of a rigid outer shell made of VeroWhitePlus and a compliant core material with a Shore95. The flexural behavior of these multi-material beams, with varying core-to-strut thickness ratios (c/t), was investigated through 3-point bending tests.

Initially, the study focused on the impact of varying the core-to-strut thickness ratio on mechanical performance, with a particular emphasis on energy absorption, to determine if it could outperform the individual constituents. Subsequently, the effect of introducing a softer material layer between the core and the shell—both on the upper and lower parts of the samples—was examined to assess potential enhancements compared to configurations without this interface. Finally, the influence of the interface nature between the core and the shell, considering different printing orientations and the absence of an interface, was investigated.

The key findings of this study are the following:

C-S configuration

Both the flexural modulus and strength of the multi-material beams decreased progressively with increasing core-to-strut thickness ratio with the maximum yield strength observed for $c/t = 0.05$ and the minimum for $c/t = 0.4$. The analytical estimates derived from beam bending theory consistently overestimated the flexural modulus for varying core-to-strut thickness ratios, corroborating the findings reported by Yavas [29].

The energy absorption capacity of the multi-material struts under bending was found to exceed by around 30% that of the individual components up to a core-to-strut thickness ratio (c/t) of 0.2, aligning with the results observed by Yavas[29].

To summarize, for C-S samples printed horizontally without any softer interface, three distinct behaviors are observed, classified based on their content of soft materials:

- Lower ratios ($c/t = 0.05$ and $c/t = 0.1$): Given their thinner layer of soft core, they exhibit behavior similar to that of VeroWhitePlus, with both demonstrating brittle complete failure characteristics. In terms of energy absorption, these composite beams outperform the monolithic VeroWhitePlus beam in both energy absorption and efficiency.
- Intermediate ratios ($c/t = 0.2$ and $c/t = 0.4$): Both ratios experience delamination, which leads to interfacial failure. This phenomenon significantly weakens the material properties, creating a substantial performance gap between the lower ratios and the intermediate ratios. As a result, energy absorption decreases considerably.
- Higher ratios ($c/t = 0.6$ and $c/t = 0.8$): They exhibit behavior similar to Shore95 and do not experience fracture. However, all samples displayed slipping. In terms of energy absorption, these composite beams outperform the monolithic Shore95 beam in both energy absorption and efficiency.

In terms of energy efficiency, samples presenting more soft material content are less efficient.

C-I-S configuration

For C-I-S samples, to which we add a thin soft interface of TB+, the following differences are observed compare to the original C-S configuration:

Overall, the material behavior was not significantly impacted.

- For lower core-to-strut thickness ratios, while the interface can improve the overall fracture behavior by smoothing the failure process, it also results in earlier onset of failure due to the interface-induced delamination.

- For intermediate core-to-strut thickness ratios, delamination was delayed, though the fracture behavior remained brittle. Although the soft interface mitigates the abruptness of the failure process, it does not entirely prevent delamination or diminish the propensity for fracture in these multi-material struts.
- For higher core-to-strut thickness ratios, adding additional soft material—despite the existing high proportion of soft material—resulted in reduced performance. This is attributed to the diminished contribution of the brittle material properties.

The addition of an interface enhances flexural strength and energy absorption primarily at a core-to-strut thickness ratio of 0.2. For ratios below this threshold, energy absorption significantly decreases, whereas for ratios above 0.2, it remains relatively stable but slightly lower. These findings diverge from Mueller's observations for round beams, where higher ratios led to increased energy absorption, attributed to the geometry that supports crack bifurcation of the shell thanks to the interface that does not fail. In contrast, the straight crack propagation in rectangular beams limits energy absorption improvements.

Consequently, the geometry of the beam plays a crucial role in determining the effectiveness of incorporating an interface layer between the core and the shell. In the case of a round beam, the interface layer completely encases the core, providing a uniform distribution of stress throughout the structure, reducing the likelihood of stress concentration at any single point. Consequently, the risk of crack initiation is minimized, as there are no highly localized points of load where failure is most likely to occur. In contrast, in a rectangular beam, the stresses are concentrated primarily at the point of contact and along the thickness of the beam. This results in a significant concentration of stress at the localized region where the indenter is applied, which can lead to a higher likelihood of crack initiation and propagation.

In terms of energy absorption efficiency (EAE), the interface does not play a significant role with really small enhancement and reductions. For high ratios, the addition of a softer interface can improve slightly (0.2 - 0.5 %) the energy absorption potential of the composite structure. Conversely, for medium ratios, the benefits of the interface are less pronounced. For lower ratios, significant reductions in efficiency (5 - 7 %) are observed.

DIC analysis demonstrates that overall, the addition of an interface layer improves the material's ability to manage strain by promoting smoother and more uniform strain distribution, leading to a more cohesive structural response.

Change in printing orientation

To address the delamination issue, samples were printed vertically. Specifically, the printing orientation influences the sharpness of the interfaces between the face and core materials. When printed horizontally, the interfaces tend to be sharp with a thickness of less than 20 μm . In contrast, vertical printing results in more blurred interfaces with a thickness greater than 150 μm .

As the samples receive increased UV exposure and additional layers—given their vertical printing orientation—they tend to exhibit more brittle behavior, like VeroWhitePlus.

For lower core-to-strut thickness ratios, particularly at 0.05, vertical printing results in decreased mechanical performance due to the occurrence of delamination. This phenomenon suggests the presence of a potential threshold effect, where the addition of a soft layer below a critical thickness can compromise the mechanical properties of the sample. For intermediate ratios, vertical printing successfully prevents delamination and improves mechanical performance, validating the effectiveness of the approach.

Regarding yield strength, the orientation is found to be insignificant for very thick layers. For intermediate ratios, a blurred interface is considered more advantageous. Conversely, a sharp interface is preferred for very thin layers. Regarding energy absorption, it is observed that changing the printing orientation significantly decreases the capacity for smaller ratios. For intermediate ratios, the trend is reversed, with energy absorption nearly doubling. For higher ratios, although energy absorption remains superior with vertical printing, the percentage of improvement is diminished.

We can conclude that the optimal approach depends on the layer thickness:

- Thicker Soft Layer: It is more advantageous to have a blurred surface, thus the sample should be printed vertically.
- Thinner Soft Layer: It is better to have a sharp interface, thus the sample should be printed horizontally.

Choice of the best ratio

Given that the addition of an interface does not significantly enhance the mechanical performance of the multi-layer struts and may even slightly reduce it, the use of an interface will be excluded from the next phase of this study, which will focus on TPMS (Triply Periodic Minimal Surfaces) lattice structures.

To further investigate the performance of TPMS lattice structures incorporating the multi-material beams, a single core-to-strut thickness ratio will be selected for printing and comparison with monolithic pure lattice samples made of VeroWhitePlus and Shore95. The decision to choose only one ratio is driven by constraints related to time and available materials. Ratio $c/t = 0.2$ has been identified as the optimal compromise among the ratios that show performance improvements when printed vertically. It provides the highest values for both energy absorption and yield strength.

2.3.1 Limitations

Printing conditions

In multi-material additive manufacturing, a pivotal issue is the interfacial compatibility of constituent materials. The mechanical properties of multi-material networks are significantly influenced by the interfacial microstructure and adhesion among the constituents, as stress propagation occurs across these interfaces. Various parameters associated with the printing process have been shown to influence the properties of this interface which could alter the behaviour of our samples. Mueller et al. [44] examined factors such as the position on the print table, the time interval between printing and testing, and the storage conditions. Their findings indicated that nearly all investigated factors exerted a statistically significant influence on the final material properties. Specifically, they highlighted a pronounced time dependency of material properties, particularly within the first 24 hours post-printing. Consequently, to ensure reproducible results, it is crucial to maintain consistent parameters when comparing different parts or batches.

In another study, Mueller [36] extended the investigation to the micro-scale examination of interfaces, focusing on interfaces between two base materials (VeroWhitePlus and TangoBlackPlus) and their mixes in different ratios. The study revealed that the mixing process did not produce a continuous blend of base polymers. Instead, it resulted in a composite embedding, where one base material served as a matrix with inclusions of the second base material, introducing local anisotropy at the micro-level.

On their side, Moore and Williams [43] explored tensile fatigue interface behavior under cyclic loading, testing combinations of materials at various pre-strains up to 1,000,000 cycles. They found that specimens with multi-material interfaces generally did not exhibit a reduced fatigue life compared to the base materials. However, erratic failures were more frequent. Specimens printed with the “glossy” option, where surfaces not covered in support material exhibited a shiny finish, showed increased interface strength. The premature failures were attributed to voids inherent in the printing process, which were more prominent at multi-material interfaces.

DIC parameters

As outlined in the Methods section, the accuracy of Digital Image Correlation (DIC) is highly dependent on the chosen parameters, which significantly influence the strain and displacement fields obtained. One notable limitation is that DIC software struggles with images exhibiting large deformations. In such cases, the tracking seed points may move out of the field of view, leading to inaccurate or incomplete data. Consequently, we were constrained to analyzing images captured at relatively low strain values to ensure reliable results.

Additionally, DIC is sensitive to scale variations between different analyses. These variations can cause significant discrepancies in the measured values, making it challenging to perform precise comparisons. The inability to adjust for scale differences further limits the ability to conduct detailed quantitative analyses, which is why our analysis focused on overall behavior, using qualitative assessments based on color hue variations.

The choice of pattern used for painting the samples plays a critical role in the quality of the DIC results. In this study, we followed the guidelines provided by Ncoor and achieved satisfactory image quality with clear DIC results. However, the accuracy of the measurements could potentially be improved by employing alternative methods for generating the speckled pattern.

Additionally, the setup of the experiment significantly impacts the quality of the images. Factors such as inadequate camera calibration and inconsistent lighting can undermine the accuracy of the data collected. These elements collectively influence the precision of DIC measurements, underscoring the importance of meticulous experimental design. Addressing these factors is essential for enhancing data reliability and achieving high-quality results.

2.3.2 Perspective

In this thesis, the flexural behavior of multi-material struts was assessed using three-point bending (3PB) tests, a method selected due to its established use in the literature, including the study by Yavas [29]. During our analysis, instances of delamination were observed in the samples, which may be linked to shear stresses potentially introduced by the 3PB test. These shear stresses arise from the concentration of load in the center of the beam, particularly at the supports and loading points. While it is possible that these stresses are a contributing factor to the observed delamination, it is important to consider that other factors might also be at play. To address these potential issues, future research could explore the use of four-point bending (4PB) tests. The 4PB setup offers a more balanced load distribution across the specimen, which could reduce shear stresses at the extremities and provide a more accurate assessment of the material's flexural performance. By implementing the 4PB method, the goal would be to achieve a more uniform stress distribution and gain a clearer understanding of the material's behavior under load. Although the connection between shear stresses and the three-point bending setup remains a consideration, the adoption of four-point bending tests in future studies may help clarify these effects and lead to more reliable data on the material's true performance. This approach would potentially enhance the accuracy of flexural evaluations and contribute to a better understanding of multi-material struts.

Additionally, further research should delve into the complexities of Shore95 material. Unlike pure materials such as TangoBlackPlus (TB) or VeroWhitePlus (VW), Shore95 is a composite digital material that combines elements of both. As a result, the thickness of the Shore95 layer may not accurately reflect its mechanical properties due to the blending of materials. Future investigations should focus on understanding how the mix of TangoBlack and VeroWhite influences the overall performance of Shore95, including its mechanical properties and how they compare to those of the individual components.

This line of inquiry could also provide insight into the delamination observed in samples with a core-to-thickness ratio (c/t) of 0.05, printed in a vertically orientation. The core dimension in this case is $300\text{ }\mu\text{m}$, with the interface exhibiting a blurred transition zone spanning $120\text{-}140\text{ }\mu\text{m}$ on either side of the core. As a result, the pure Shore95 core in this configuration is extremely thin, with a surface layer that may not exhibit homogeneous material properties due to the limited mixing of different voxels within such a narrow region. The non-uniformity in the Shore95 layer could contribute to weaknesses at the interface, thereby increasing the susceptibility to delamination under stress.

Chapter 3

Triply Periodic Minimal Surface Structure

3.1 Methods and Materials

Since all ratios were tested on singular beam structures, this section will extend the study by focusing on a complete TPMS lattice structure, incorporating those sandwich beams as cell wall struts.

3.1.1 Materials

To optimize time and material usage, we selected the best ratio and printed only one TPMS lattice with wall struts using this ratio, alongside one entirely VW+ and one entirely Shore95, to compare their mechanical performances. The optimal ratio identified was 0.2. Therefore, a TPMS lattice was constructed with a soft interior core and a hard shell, maintaining a core thickness to total thickness ratio (c/t) of 0.2.

3.1.2 Methods

Design and dimensions

The design and construction of the TPMS lattice structure required careful consideration of several key parameters to ensure the integrity and consistency of the results. The following parameters were identified as crucial and needed to be strictly adhered to and fixed:

- (a) **Ratio of Inner to Outer Structure:** The chosen ratio of 0.2 established between the inner and outer structures is critical for maintaining the desired mechanical properties and allowing comparison in our study.
- (b) **Number of Cells:** The lattice structure was designed with 5 cells along each dimension. This number was chosen to ensure convergence of the results and to mitigate edge effects. With only 3 cells, for example, only the middle cell would be surrounded by other cells, making it the only one that behaves homogeneously. By using 5 cells, the central cells are well surrounded, ensuring a more consistent and representative behavior throughout the lattice.
- (c) **Number of Pixels:** To accurately describe each unit cell, a minimum of 80 pixels is required, as established by previous research conducted by Luca d'Andrea. Fewer pixels would result in a pixelated cross-section rather than a smooth function. Initially, we aimed for 400 pixels per unit cell to ensure high resolution. However, due to printer limitations, we reduced this to 300 pixels while applying smoothing techniques to maintain the quality of the representation.
- (d) **Dimensions:** Initially, the overall dimensions of the lattice structure were set to $5 \times 5 \times 5 \text{ cm}^3$. This size was chosen to align with the material capacity of the printer while providing a sufficiently large sample for mechanical testing. However, upon testing the $5 \times 5 \times 5 \text{ cm}^3$ TPMS, we observed that the structure was too strong for the testing machine. It withstood the maximum load of 30 kN from the load cell without breaking or deforming. Consequently, to achieve measurable deformation and

failure, we reduced the size of the TPMS lattice to 1x1x1 cm³. This adjustment ensured that the samples were within the operational limits of the testing equipment and provided more relevant data on the mechanical performance of the lattice structure.

Generation with MatLab code

The TPMS structure were generated using MATLAB code (cfr. appendices) provided by Luca d'Andrea from the university Politecnico di Milano, which outputs a .TIFF file. A .TIFF file, or Tagged Image File Format, is widely used for storing high-quality images and graphics, representing images as a grid of pixels where each pixel contains color and intensity information.

The MATLAB code allows for the generation of different types of TPMS structures by inputting the algebraic formula corresponding to each cell structure. In this study, we focused on three specific types of TPMS: the diamond, the gyroid, and the IWP. Each of these structures can be represented by their algebraic equations.

- The **Diamond TPMS** is a complex, self-intersecting surface characterized by a repeating network of diamond-shaped cells. It has a high level of symmetry and minimal surface area. This structure is used in materials science and porous materials for its unique properties, including high surface area and structural strength. It is the most bending-dominated structure one among the 3 TPMS lattice [73].

$$f(x,y,z) = \cos(x)\cos(y)\cos(z) - \sin(x)\sin(y)\sin(z) + b$$

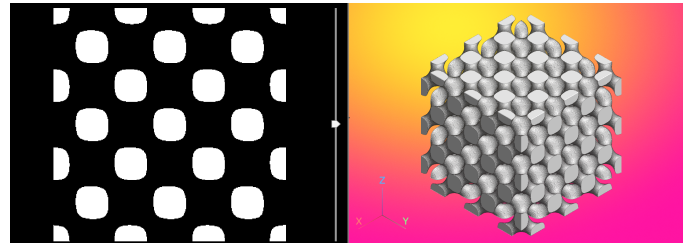


Figure 3.1 – Illustration of the XY cross sections and 3D volume of a diamond TPMS with 3 cells.

- The **Gyroid TPMS** is known for its intricate and interconnected labyrinthine structure. It forms a repeating pattern of interconnected, twisted shapes with minimal surface area. The Gyroid is often used in applications such as filtration, as it provides a high surface-to-volume ratio and is capable of efficiently separating fluids[73].

$$f(x,y,z) = \sin(x)\cos(x) + \sin(y)\cos(y) + \sin(z)\cos(z) + b$$

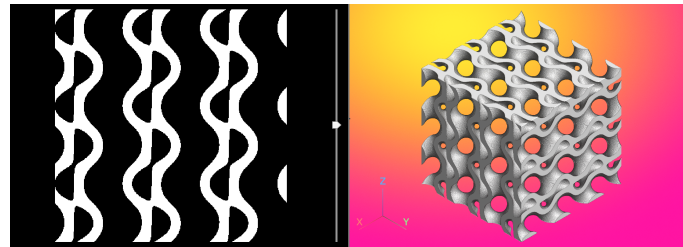


Figure 3.2 – Illustration of the XY cross sections and 3D volume of a gyroid TPMS with 3 cells.

- The **IWP (Inverse Schwarz P Surface) TPMS** is derived from the Schwarz P surface, but it is an inverted version. It features a repeating lattice of interconnected, curved, and tubular structures. The IWP is used in various scientific and engineering applications, including biomaterials and foams, due to its desirable properties, such as high surface area and mechanical stability [73].

$$f(x,y,z) = 2\cos(x)\cos(y) + 2\cos(y)\cos(z) + 2\cos(x)\cos(z) - \cos(2x) - \cos(2y) - \cos(2z) + b$$

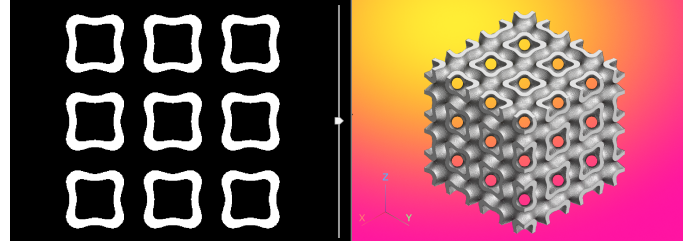


Figure 3.3 – Illustration of the XY cross section and 3D volume of a IWP TPMS with 3 cells.

In these equations, x , y and z represent the spatial coordinates. Each of these structure has its own value of b and Δ . The parameter b represents the porosity value. It measures the empty spaces in the structure and ranges from 0 to 1, where 0 means completely solid and 1 completely empty. The parameter Δ represents a threshold value. The conditions $f < \Delta$ and $f > -\Delta$ are used to determine whether a point in space corresponds to a solid region (1) or a void region (0).

The code generates a first 3D Matrix M representing a cubic space divided into small cubes. The function $f(x, y, z)$ is then evaluated for each point in this space, and based on whether the value is within the range $(-\Delta, \Delta)$, the corresponding entry in the matrix is set to 0 or 1, determining whether that region is considered solid or void. This first matrix (M) represents the original inner structure, the core.

Subsequently, the code constructs an exterior shell surrounding the TPMS structure. This is achieved by initializing a new matrix, $D1$, with the values from the original binary matrix M . A morphological dilation operation is then applied iteratively to $D1$ with a variable loop defining the number of times the dilatation is repeated. Each iteration adds pixels to the solid regions, thereby expanding the structure and creating an outer shell around the TPMS core. The number of iterations directly controls the thickness of this exterior shell. Finally, the code performs a boolean subtraction between the whole new dilated structure $D1$ and the original matrix M . This operation isolates the shell structure by removing the core, resulting in matrix $E1$, which exclusively represents the exterior shell of the TPMS structure. An example of all structures generated in .tiff files by the code, for a Gyroid TPMS is illustrated in the Figure 3.4 below.

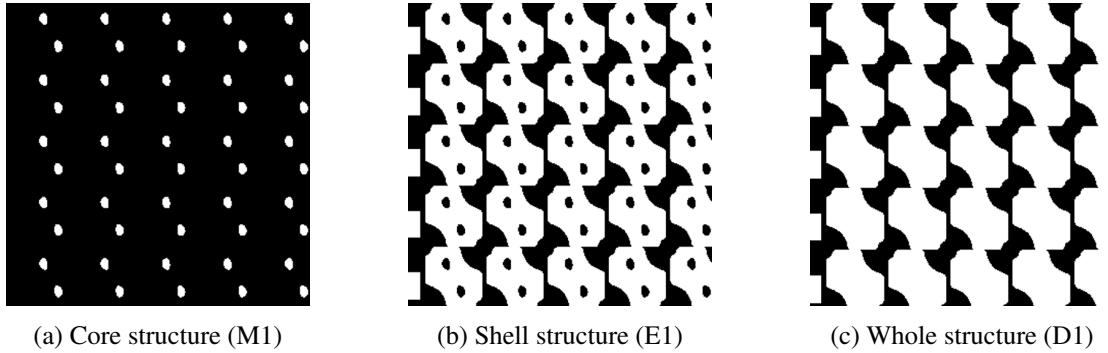


Figure 3.4 – Cross section of the Gyroid TPMS structure (.tiff files)

To achieve a core-to-strut thickness ratio of 0.2, the inner structure M must first be created with the smallest possible core thickness and the highest porosity. This involves generating a structure with the minimum volume fraction. Ibrahimi et al. [74], have identified the optimal parameters b and Δ for attaining the lowest volume fraction for each of the three TPMS types. Once the inner structure is created, the core thickness is measured using ImageJ software with the BoneJ plugin. Given that the structure is three-dimensional, measurements must be taken in all three spatial directions, which ImageJ facilitates. After determining the core thickness, the loop parameter in the code is adjusted to iteratively dilate the structure until the total thickness of the exterior shell (matrix $D1$) is five times the core thickness. The Trabecular Thickness function within the BoneJ plugin in ImageJ is then used to verify this thickness. Table 3.5 provides a summary for each TPMS structure, including: the parameters b and Δ used to generate the thinner inner core, as specified

in the study by Ibrahimi et al.[74] ; the loop parameter employed to create the exterior shell to achieve the desired core-to-strut thickness ratio; the resulting porosity of the entire volume for each TPMS; and the mean trabecular thickness of both the inner core and the whole structure, calculated in pixels using the BoneJ plugin.

	b	Δ	loop	Porosity	Volume Fraction (= 1 – porosity)	Core mean thickness	Volume mean thickness
Diamond	1	0.4	13	0.0307	0.9693	12.15 (erroded 3 times)	60.75
Gyroid	1.5	0.2	15	0.1559	0.8441	8.37	40.40
IWP	2	0.2	3	0.0596	0.9404	2	9.86

Figure 3.5 – Parameters used to generate the 3 TPMS structures: Diamond, Gyroid and IWP

All generated .TIFF files are then converted to .STL files using ImageJ for further processing.

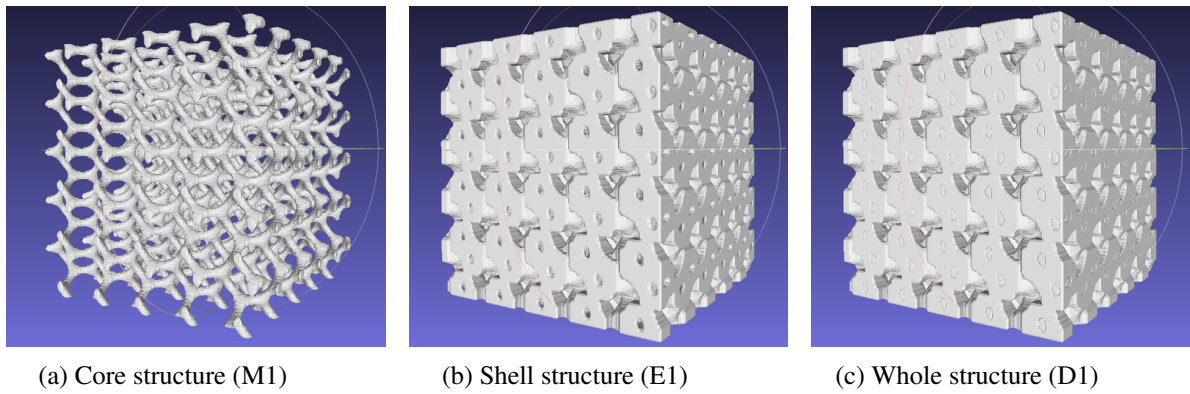


Figure 3.6 – 3D volume of the Gyroid TPMS structure (.stl files)

Finally, the .STL files are imported into Meshlab, where the pixel dimensions are scaled to real-world units for accurate representation.

Choice of the TPMS structure

Due to time and material constraints, only one type of TPMS was printed and tested. The diamond structure was selected initially because it is the most bending-dominated TPMS design, known for its effective energy absorption prior to fracturing. However, the lowest volume fraction achievable with the given parameters resulted in an inner structure thickness of 17 units, necessitating an overall thickness of 85 units. Since the voids between the beams of the inner structure are 33 units apart, an overall thickness of 85 units led to a nearly solid structure.

It was determined that the maximum allowable erosion of the inner structure, while maintaining connectivity, was to a thickness of 12 units. The inner structure with this thickness is depicted in Figure 3.7 (a). Despite this adjustment, the TPMS remained excessively bulky and exhibited very low porosity. Figure 3.7 (b) illustrates the overall exterior volume of the structure, which shows minimal porosity. Furthermore, closer examination of the interior, as shown in Figure 3.7, reveals small detached particles. These particles represent the remaining porosity, which is notably insufficient. This excessive bulk compromised the lightweight and porous properties typically associated with cellular solids. Although the diamond structure demonstrates favorable performance under compression, its substantial bulk and internal discontinuities reduced its suitability for the study.

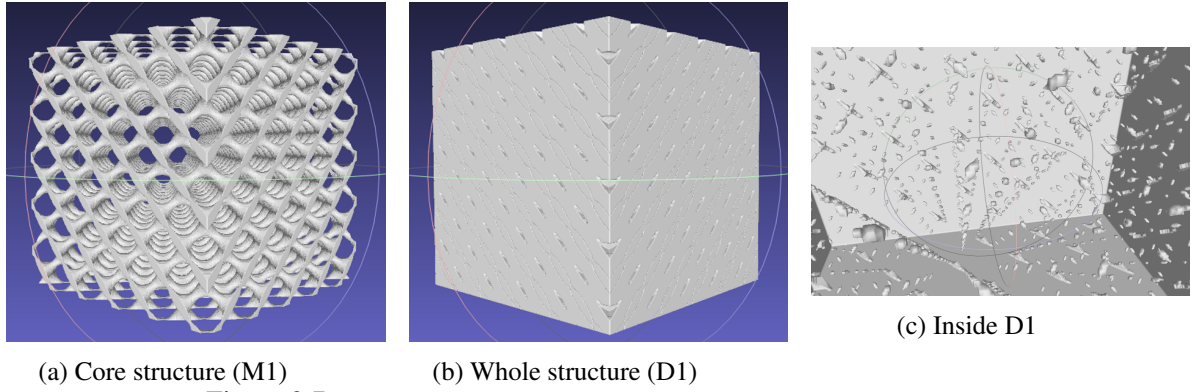


Figure 3.7 – 3D volume of the Diamond TPMS structure (.stl files)

As an alternative, the gyroid and IWP structures were generated. The IWP, although highly porous and visually similar to the previously tested sandwich panels, displayed discontinuities when produced with a smaller thickness. This issue is evident in Figure 3.8 (a) and (b), which depict the generated inner structure. The presence of non-continuous white lines indicates insufficient pixel resolution for the structure, a limitation imposed by the printer's parameters that could not be altered.

The gyroid structure, unlike the other TPMS designs, does not exhibit discontinuities or performance issues. Additionally, as detailed in Table 3.5, it demonstrates the highest porosity among the three TPMS structures after the IWP, with the Diamond structure exhibiting a higher volume fraction. Since a bending-dominated structure requires high porosity to effectively absorb energy, the gyroid structure emerges as the optimal choice. Its continuous and thinner design aligns well with the study's goals, making it a more suitable option for achieving the desired performance characteristics. Consequently, the gyroid structure was selected for its advantageous balance of structural continuity and porosity.

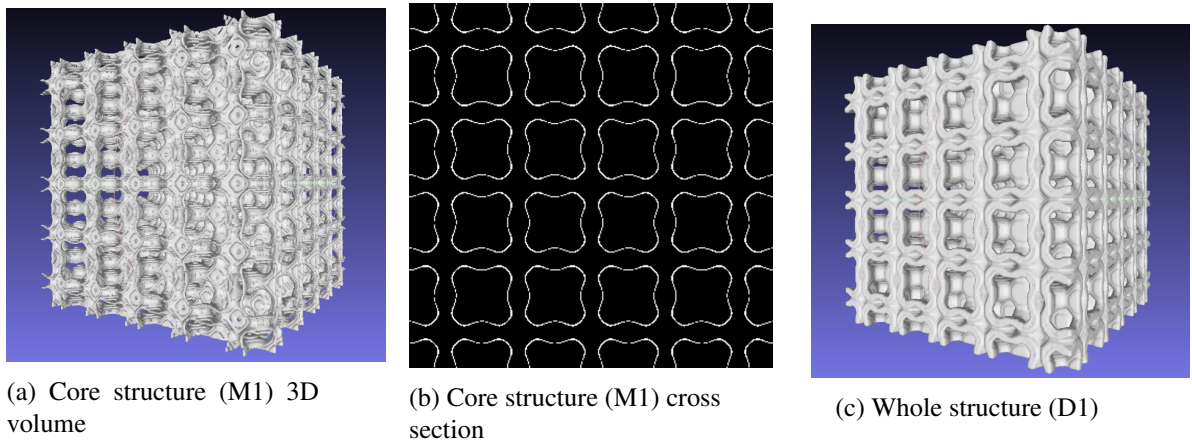


Figure 3.8 – 3D volume and cross section of the IWP TPMS structure

3D printing

The same printer and printing process used for the rectangular beam were also employed for the TPMS structures. In this case, the printing orientation is expected to have no effect on the final structure, as the TPMS consists of a cube with identical cells throughout.

Support material was applied to all surfaces but could not be completely removed, owing to the small size of the samples and their limited porosity and due to the lack of a suitable technique for its complete removal. It is assumed that the presence of the support material will have a minimal impact, given its significantly lower stiffness compared to the constituent materials. Additionally, due to the continuous nature of the support within the gyroid structure, rather than being isolated in 'pockets' that could be compressed, it is expected that the support material will be evacuated during testing.

Due to constraints related to time and the availability of materials, only a single sample was printed. Consequently, the statistical variability of the sample could not be assessed or analyzed.

Compression test

For the TPMS structures, we evaluated mechanical performance under compression using the same MTS machine as before. The testing was conducted with a compression rate of 2 mm/min, utilizing a 30 kN load cell, which is the maximum capacity available in our lab. The test was stopped approximately at 10mm of crosshead displacement for all samples. Similar to the three-point bending test, we recorded the crosshead displacement and reaction force. This data enabled us to construct load-displacement curves and calculate the energy absorbed by integrating the area under these curves.

3.2 Results and Discussion

The results of the load-displacement curves are illustrated in Figure 3.9. It is observed that the TPMS lattice of full Shore95 maintains its soft material behavior; as the crosshead displacement increases and load is applied, minimal load is supported due to significant deformation, with a maximum reaction load of approximately 1.5 [kN] reached by the end of the displacement. This behavior is consistent with previous results obtained for a single pure Shore 95 beam. For the pure VW+ gyroid, the initial portion of the curve displays a linear relationship between load and displacement until a stress point of 11 [kN] is reached. Beyond this point, as displacement continues, the reaction load increases in a non-linear manner with minor variations, entering the plastic region, eventually reaching the maximum capacity of the load cell, which is 30 [kN], without fracturing.

For the multi-material gyroid TPMS structure with a ratio of 0.2, the curves exhibit behavior similar to that of the VW+ curve. Despite the combination of compliant and stiff materials, the curves display a trend more characteristic of rigid materials. The response increases linearly up to a peak point of approximately 10 [kN] and continues to increase non-linearly, with values slightly lower than those observed for VW+.

Regarding energy absorption, as illustrated in Figure 3.10, it is noted that, in accordance with the load-displacement curve trends, the energy absorption of the multi-layer TPMS lattice is 12% lower than that of the gyroid made of the individual rigid constituent.

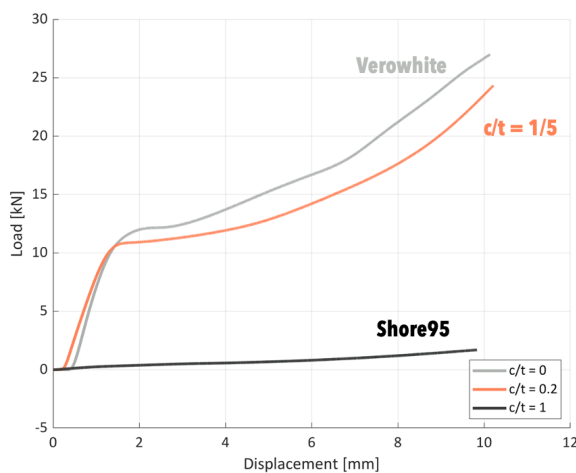


Figure 3.9 – Load [kN] vs Displacement [mm] curves for $c/t = 0, 0.2$ and 1.

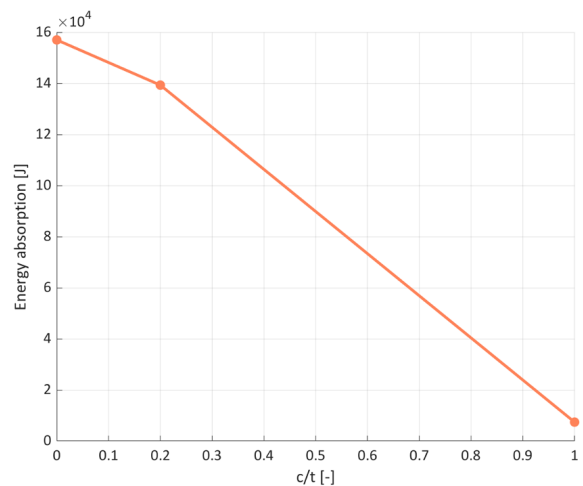


Figure 3.10 – Energy absorption versus ratios for $c/t = 0, 0.2$ and 1.

Examination of the pure VW+ lattice under compression, shown in Figure 3.11 reveals that, as displacement increases and the structure is compressed, the support material is expelled. This observation confirms the assumptions outlined in the method section, proving that keeping the support has little impact.

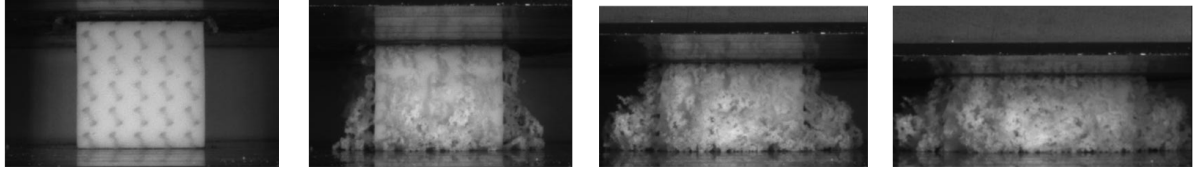


Figure 3.11 – Compression test of VeroWhitePlus gyroid with increasing displacement

Despite exhibiting similar mechanical properties during loading, the VW+ gyroid and the multi-material gyroid differ in their recovery behavior after unloading. As shown in Figure 3.12 (a) and (b), which represent the VW+ gyroid just before and immediately after unloading, the structure recovers partially but does not return completely to its original form. The same behavior is observed for the multi-material gyroid in Figure 3.13.

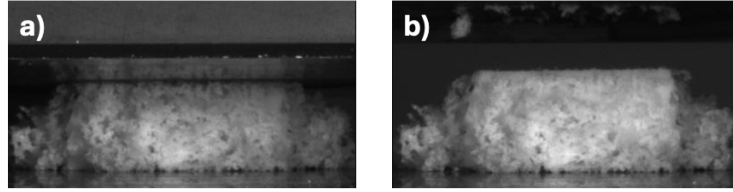


Figure 3.12 – Pure VeroWhitePlus gyroid during compression test a) just before unloading, b) just after unloading.

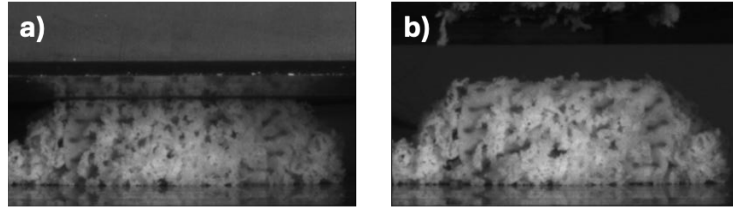


Figure 3.13 – Multi-layer gyroid with ratio $c/t = 2$ during compression test a) just before unloading, b) just after unloading.

However, one week after the experiments, significant differences in structural recovery are evident, as illustrated in Figure 3.14. While the Shore 95 gyroid fully returns to its original shape, both the VeroWhite and multi-material gyroids do not fully recover. Nevertheless, both structures show more recovery compared to their immediate post-experiment state, with the multi-material beam demonstrating a greater degree of recovery than the pure VW+ gyroid. A red line is traced in the figures to outline the gap between the original square form and the deformed structure of the VW+ and multi-material gyroids. This observation is particularly interesting because, despite similar loading behaviors, the multi-material gyroid returns closer to its original form compared to the rigid material. This suggests that the soft constituent of the multi-material gyroid contributes to its enhanced compliance, toughness while its strength is still reinforced by the rigid constituent.

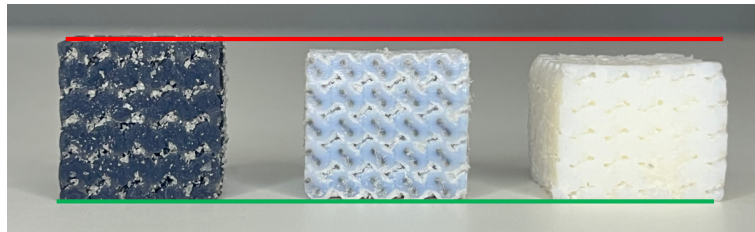


Figure 3.14 – Pure Shore95, multi-layer with $c/t = 0.2$ and pure VW+ gyroid structure, one week after the compression test

To better quantify the extent of post-damage deformation and recovery in VW+ and the multi-material TPMS, a relaxation test was conducted. The test involved initially loading the sample until a displacement

of 4[mm] was reached, followed by complete unloading, allowing the sample to relax. The sample was then reloaded until the same displacement of 4[mm] was attained. The load versus displacement curves during the loading phase and during the reloading phase after relaxation are presented in Figures 3.15 and 3.16, respectively.

Prior to relaxation, both load-displacement curves display a linear region, which is followed by entry into the plastic region characterized by a plateau. After this phase, compression of the structural particles occurs, leading to a slight increase in load as the structure begins to collapse internally. After relaxation, the VW+ and multi-material TPMS samples exhibit signs of permanent deformation, evidenced by the absence of a distinct plastic region.

The VW+ sample exhibits an initial plateau due to plastic deformation, with particles having already undergone crushing. As a result, the compression plate does not engage until a displacement of 2 [mm] is reached. In contrast, the multi-material TPMS begins to compress at a much lower strain, indicating a higher degree of recovery toward its original form compared to VW+.

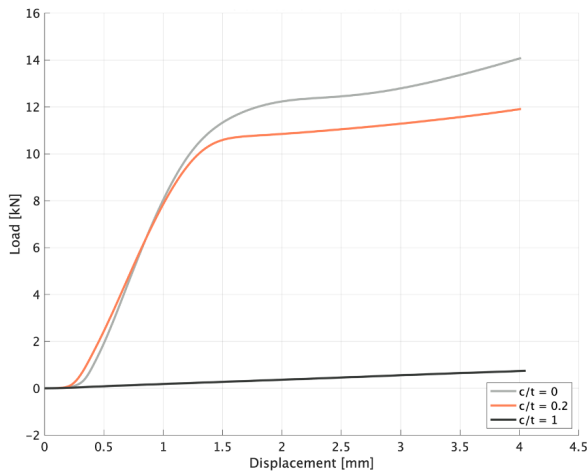


Figure 3.15 – Load [kN] vs Displacement [mm] curves for $c/t = 0, 0.2$ and 1 during loading.

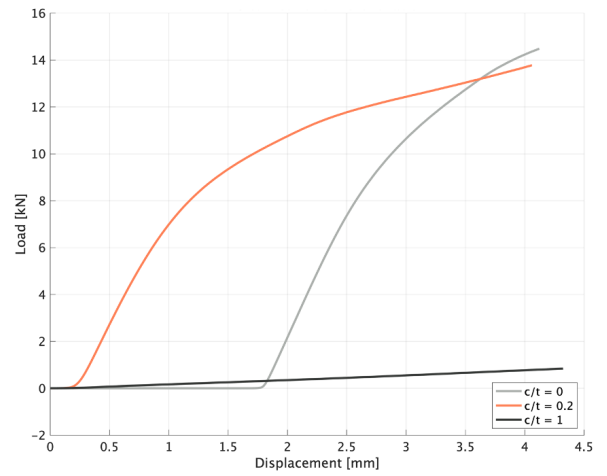


Figure 3.16 – Load [kN] vs Displacement [mm] curves for $c/t = 0, 0.2$ and 1 during reloading after relaxation.

This observation is further corroborated by the energy absorption curves shown in Figures 3.17 and 2.62. Initially, the pure VW+ TPMS absorbed more energy than the multi-material TPMS. However, after relaxation, the multi-material TPMS, having more effectively regained its shape and surface area, absorbs significantly more energy than the VW+ TPMS, which exhibits greater residual plasticity and damage post-deformation.

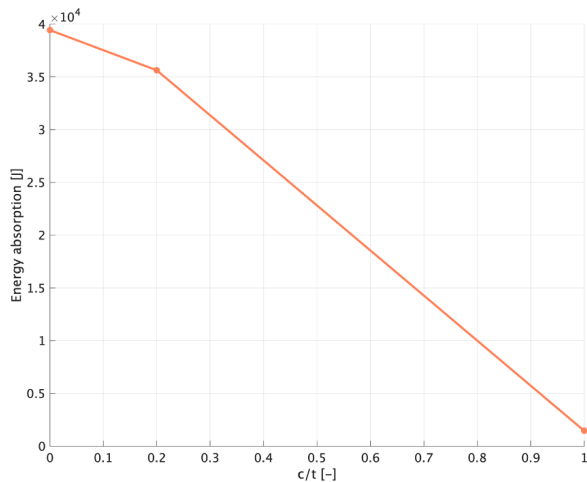


Figure 3.17 – Energy absorption versus ratios for $c/t = 0, 0.2$ and 1 during loading.

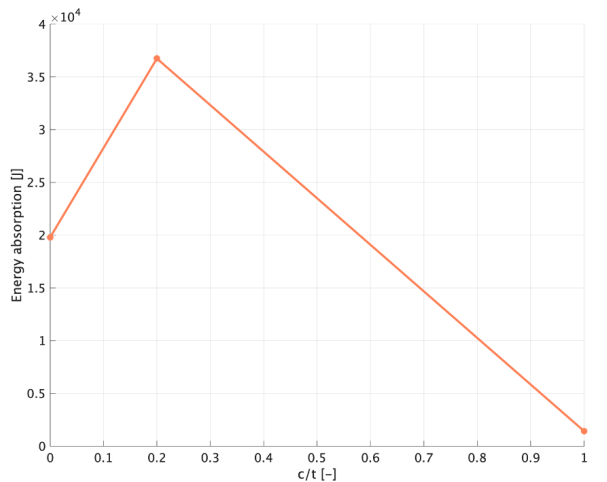


Figure 3.18 – Energy absorption versus ratios for $c/t = 0, 0.2$ and 1 during reloading after relaxation.

3.3 Conclusion

In summary, 3D multi-layer gyroid TPMS structures were designed and fabricated using PolyJet 3D printing. Three types of gyroids were printed: one with pure stiff material VeroWhitePlus ($c/t = 0$), one with pure compliant material Shore95 ($c/t = 1$), and one consisting of a multi-layer lattice struts with a rigid outer shell of VeroWhitePlus and a compliant core material with a Shore95, featuring a core-to-strut thickness ratio of 0.2. The compression behavior of these multi-material gyroids was investigated through in-plane compression tests.

While the flexural behavior of individual beams from these structures has been previously studied, demonstrating superior performance for a core-to-strut ratio of 0.2 compared to the individual constituents, this part of the study aimed to evaluate whether similar improvements could be achieved when applied to lattice structures, specifically TPMS (Triply Periodic Minimal Surface) structures used in a wide range of applications. The objective was to determine if these structures could simultaneously enhance strength and toughness, combining a strong material with compliant properties, and allowing for property tuning through varying core-to-strut thickness ratios. A particular focus was placed on assessing energy absorption capacity.

The results demonstrated that the TPMS gyroid with multi-material struts of ratio $c/t = 0.2$, which integrates both stiff and compliant materials, exhibits mechanical properties and behavior closely resembling those of its individual stiff constituent. However, it shows a significant 75% increase in energy absorption capacity due to its superior ability to recover its original shape after deformation compared to the stiff material alone. This smaller post-damage proves the effectiveness of the combination of materials within the composite structure. The rigid outer shell, made from VeroWhitePlus, provides strength and structural integrity, while the compliant core, composed of Shore95, contributes to the overall flexibility and ability to return to the original form after loading. This dual-material approach leverages the benefits of both components, resulting in enhanced mechanical performances.

The results of this study are quite different when compared to Yavas's findings [29], who examined multi-material honeycomb lattice structures. Yavas's research showed that multi-material lattices had an energy absorption capacity that was about 2 to 3 times greater than that of their individual components, regardless of the core-to-strut thickness ratios tested. Additionally, Yavas observed that while the fully PLA lattices failed in a semi-brittle manner, the multi-material lattices exhibited a progressive failure with multiple stress peaks during deformation, which enhanced their energy absorption capabilities.

These differences can be explained by variations in porosity between the studied structures. Although our gyroid lattices have higher porosity compared to some alternatives, their overall porosity is still relatively low when compared to the honeycomb structures analyzed by Yavas. The higher porosity of the honeycomb lattices allows them to deform more readily and absorb energy more efficiently, thanks to their enhanced bending properties, which allow for significant deformation without structural collapse. Conversely, the lower porosity of the gyroid structures restricts their energy absorption potential, as the denser configuration constrains their ability to undergo the same degree of deformation. Additionally, it is important to note that Yavas worked with 2D-extruded honeycomb lattices, whereas the structures studied here are fully 3D-printed.

3.3.1 Limitations

The primary objective was to achieve and maintain a core-to-strut thickness ratio of 0.2, a challenge that proved to be neither straightforward nor easy to achieve. Given this constraint, design flexibility was limited to adjusting the structure and porosity. Although the desired ratio was achieved, comparing the performance of different structures proved to be challenging due to variations in porosity. To facilitate a more accurate comparison, it would be necessary to evaluate all three structures under identical porosity conditions.

The complexity of the TPMS structures, coupled with constraints on file size, presented additional limitations. Initially, the diamond structure was selected; however, it was found that adhering to the ratio compromised its bending-dominated properties, resulting in reduced porosity. Additionally, due to insufficient pixel resolution given the size constraints, the IWP structure exhibited discontinuities.

3.3.2 Perspective

This thesis offers valuable insights into multi-material lattice structures, demonstrating that the combination of hard and soft constituents can effectively balance strength and toughness, thereby enhancing energy absorption. More importantly, the ratio of stiff to compliant materials can be adjusted to fine-tune these mechanical properties. While these observations were confirmed experimentally within the time constraints, future work could further validate these findings through numerical simulations.

Although this finding was limited to a single ratio, it paves the way for further research on other ratios, potentially leading to the creation of new materials with tunable mechanical properties. This opens up a broad range of possibilities for developing advanced materials tailored to specific performance requirements.

In the context of bone scaffolds, this thesis opens up new possibilities beyond simply choosing between stiff or compliant materials; it allows for the combination of both within a single TPMS structure. By integrating materials with varying stiffness levels, it is possible to design bone implants that effectively absorb impact and limit crack propagation. Our focus was on the material aspect, specifically enhancing mechanical performance. However, imposing the thickness of the bimaterial lattice struts presented challenges and limited our design flexibility. To further integrate these structures into the field of bone scaffolds, future research could explore optimizing porosity for bone integration and adjusting the Young's modulus of these structures to better match that of natural bone.

Beyond biomedical applications, the ability to create materials with tunable energy absorption capacity opens new avenues in industries that require lightweight and impact-absorbing structures, such as aerospace and automotive sectors. These materials could be employed as protective components, offering enhanced safety and performance in demanding environments.

In conclusion, this thesis lays a foundation for future research on multi-layer TPMS structures and their potential applications across diverse domains. The demonstrated improvements in mechanical properties and energy absorption open the door to significant advancements in designing materials tailored for complex and demanding environments.

List of Figures

1.1	The different types of cellular structures. [2]	2
1.2	Cellular solids in nature: (a) Wood; (b) Sponge; (c) Trabecular bone; (d) Carrot. [1]	3
1.3	Engineered cellular solids: (a) Honeycomb; (b) Open-cell foam; (c) Closed-cell foam. [1]	3
1.4	Applications of cellular solids:(a) Sandwich panel core [6]; (b) High-performance energy absorption helmet [7] and (c) Automobile bumper based on honeycomb structure [8].	3
1.5	Examples of lattice structures from unit cell to cellular network[10]	4
1.6	Design strategy for the multi-bionic metamaterial: (a) Concentric circle pattern inspired by bone structure; (b) FCC lattice arrangement; (c) Metamaterial featuring concentric rods alternating between soft and hard materials [19].	5
1.7	(a) Nacre and (b) Bone structure[24].	5
1.8	a) Coaxial printhead with core, interface, and shell ink reservoirs. b) Cross-sectional view of the C–S printhead. c) False-colored image of the C–S nozzle showing coextruded inks (core: red, interface: blue, shell: gray).d,e) End-on views of C–S nozzles with high-resolution retracted inner channels.[28]	7
1.9	Cracking behaviour of a) pure materials of shell and core beams, b) C-S beams, c) C-I-S beams and d) Sequence of crack propagation of C-I-S beam with increasing strain from left to right [28]	7
1.10	a) 3D schematic of multi-material FFF honeycomb printing. b) FFF-printed honeycomb lattice ($c/t = 1/3$) showing cell wall details. c) Schematics showing sample orientation relative to the printing bed.[29]	8
1.11	Flexural stress–strain curves of multi-layer strut with varying core-to-strut thickness ratios [29].	8
1.12	Nominal stress–strain curves of the multi-material honeycomb lattices with different c/t ratios [29].	8
1.13	Schematic of PolyJet printing process [37].	10
1.14	Schematic of photopolymerization process induced by UV light.	10
1.15	Diagram illustrating the PolyJet printing process for bimaterial samples produced in either horizontal or vertical orientations. These two printing methods result in the bimaterial interface being created either before or after UV curing.	11
1.16	Results from nanoindentation showing spatial variations in reduced elastic modulus across bimaterial interfaces. The data is presented for interfaces formed (A) after UV curing and (B) before UV curing.	12
1.17	Bone scaffolds use.	13
1.18	Equations, unit cells and models of TPMS-based structures. [52]	14
1.19	Examples of (a) Graded, (b) Heterogeneous and (c) multiscale TPMS.[52]	15
2.1	Overview of the base materials VeroWhitePlus (VW) and TangoBlackPlus (TB), the printable digital materials from these using the Stratasys Connex3 Objet500, and their study IDs. [42]	18
2.2	Design and materials of the 2 groups of specimen.	19
2.3	Stress-strain-curve of VeroWhite and fracture strain (figure adapted from [42]).	19
2.4	Dimensions of the sample beam.	20

2.5	Beam dimensions.	20
2.6	Illustration of the samples for all ratios.	20
2.7	Samples printing orientation.	21
2.8	Three-point bending test set up.	22
2.9	Flexural Modulus computation.	23
2.10	Yield strength computation.	23
2.11	Energy Absorption computation.	25
2.12	Energy Absorption Efficiency computation.	25
2.13	Principle of Digital Image Correlation.	26
2.14	1st sample not painted and 2nd and 3rd samples painted with speckle pattern.	26
2.15	Process of DIC.	27
2.16	DIC subsets theory (adapted from [72]).	27
2.17	DIC subsets option: subset radius and spacing.	28
2.18	DIC correct and incorrect seed placement procedure.	29
2.19	u -displacement map for C-S sample with $c/t = 1$.	29
2.20	v -displacement map for C-S sample with $c/t = 1$.	29
2.21	Strains distribution map on a deformed C-S sample with ratio $c/t = 0.1$	30
2.22	Stress-strain curve for CS sample of ratio $c/t = 0.05$ with point indicating current image for DIC.	30
2.23	Stress-strain curve for CS sample of ratio $c/t = 0.8$ with point indicating current image for DIC.	30
2.24	Stress [MPa] vs Strain [-] for $c/t = 0.$	32
2.25	Stress [MPa] vs Strain [-] for $c/t = 1$.	32
2.26	Stress [MPa] vs Strain [-] for $c/t = 0.05$.	32
2.27	Stress [MPa] vs Strain [-] for $c/t = 0.1$.	32
2.28	Sample 2 with $c/t = 0.05$ after fracture.	32
2.29	Sample 2 with $c/t = 0.1$ after fracture.	32
2.30	Stress [MPa] vs Strain [-] for $c/t = 0.2$.	33
2.31	Stress [MPa] vs Strain [-] for $c/t = 0.4$.	33
2.32	Delamination progress at increasing strain for sample 1 with $c/t = 0.2$.	33
2.33	Delamination progress at increasing strain for sample 1 with $c/t = 0.4$.	33
2.34	Fracture progress at different increasing strain for sample 2 (E) and sample 1 (D) and slipping of sample 3 (F) with $c/t = 0.2$.	34
2.35	Stress [MPa] vs Strain [-] for $c/t = 0.6$.	34
2.36	Stress [MPa] vs Strain [-] for $c/t = 0.8$.	34
2.37	Stress [MPa] vs Strain [-] for all ratios.	35
2.38	Stress [MPa] vs Strain [-] for all ratios.	36
2.39	Fracture progress at different increasing strain for sample with $c/t = 0.1$.	37
2.40	Sample 1 with $c/t = 0.05$ after fracture.	37
2.41	Sample 1 with $c/t = 0.1$ after fracture.	37
2.42	Fracture progress at different increasing strain for sample with $c/t = 0.2$.	37
2.43	Effective Modulus vs ratios from Yavas [29].	38
2.44	Effective Modulus [MPa] vs ratios.	38
2.45	Yield strength [MPa] vs ratios.	39
2.46	Energy Absorption [-] vs ratios.	40
2.47	Energy Absorption efficiency [-] vs ratios.	41
2.48	ϵ_{xx} strain map for ratios a) $c/t = 0$, b) $c/t = 0.05, 0.1$ and 0.2 for C-S configuration and c) $c/t = 0.05, 0.1$ and 0.2 for C-I-S configuration.	42
2.49	ϵ_{xx} strain map for ratios d) $c/t = 0.4, 0.6$ and 0.8 for C-S configuration, e) $c/t = 0.4, 0.6$ and 0.8 for C-I-S configuration and f) $c/t = 1$	42
2.50	ϵ_{xy} strain map for ratios a) $c/t = 0$, b) $c/t = 0.05, 0.1$ and 0.2 for C-S configuration and c) $c/t = 0.05, 0.1$ and 0.2 for C-I-S configuration.	43

2.51	ϵ_{xy} strain map for ratios d) $c/t = 0.4, 0.6$ and 0.8 for C-S configuration, e) $c/t = 0.4, 0.6$ and 0.8 for C-I-S configuration and f) $c/t = 1$	43
2.52	ϵ_{yy} strain map for ratios a) $c/t = 0$, b) $c/t = 0.05, 0.1$ and 0.2 for C-S configuration and c) $c/t = 0.05, 0.1$ and 0.2 for C-I-S configuration.	44
2.53	ϵ_{yy} strain map for ratios d) $c/t = 0.4, 0.6$ and 0.8 for C-S configuration, e) $c/t = 0.4, 0.6$ and 0.8 for C-I-S configuration and f) $c/t = 1$	44
2.54	Stress [MPa] vs Strain [-] curves for $c/t = 0$ and 1	45
2.55	Stress [MPa] vs Strain [-] curves for $c/t = 0.05$ and 0.1	45
2.56	Delamination for $c/t = 0.05$	46
2.57	Stress [MPa] vs Strain [-] curves for $c/t = 0.2$ and 0.4	46
2.58	Stress [MPa] vs Strain [-] curves for $c/t = 0.6$ and 0.8	46
2.59	Stress [MPa] vs Strain [-] curves for xy-oriented printed samples.	47
2.60	Stress [MPa] vs Strain [-] curves for xz-oriented printed samples.	47
2.61	Yield Strength [MPa] for all ratios.	47
2.62	Energy Absorption [MPa] for all ratios.	48
3.1	Illustration of the XY cross sections and 3D volume of a diamond TPMS with 3 cells.	54
3.2	Illustration of the XY cross sections and 3D volume of a gyroid TPMS with 3 cells.	54
3.3	Illustration of the XY cross section and 3D volume of a IWP TPMS with 3 cells.	55
3.4	Cross section of the Gyroid TPMS structure (.tiff files)	55
3.5	Parameters used to generate the 3 TPMS structures: Diamond, Gyroid and IWP	56
3.6	3D volume of the Gyroid TPMS structure (.stl files)	56
3.7	3D volume of the Diamond TPMS structure (.stl files)	57
3.8	3D volume and cross section of the IWP TPMS structure	57
3.9	Load [kN] vs Displacement [mm] curves for $c/t = 0, 0.2$ and 1	58
3.10	Energy absorption versus ratios for $c/t = 0, 0.2$ and 1	58
3.11	Compression test of VeroWhitePlus gyroid with increasing displacement	59
3.12	Pure VeroWhitePlus gyroid during compression test a) just before unloading, b) just after unloading.	59
3.13	Multi-layer gyroid with ratio $c/t = 2$ during compression test a) just before unloading, b) just after unloading.	59
3.14	Pure Shore95, multi-layer with $c/t = 0.2$ and pure VW+ gyroid structure, one week after the compression test	59
3.15	Load [kN] vs Displacement [mm] curves for $c/t = 0, 0.2$ and 1 during loading.	60
3.16	Load [kN] vs Displacement [mm] curves for $c/t = 0, 0.2$ and 1 during reloading after relaxation.	60
3.17	Energy absorption versus ratios for $c/t = 0, 0.2$ and 1 during loading.	60
3.18	Energy absorption versus ratios for $c/t = 0, 0.2$ and 1 during reloading after relaxation.	60
3.19	Load [N] vs Displacements [mm] for $c/t = 0$	67
3.20	Load [N] vs Displacements [mm] for $c/t = 1$	67
3.21	Load [N] vs Displacements [mm] for $c/t = 0.05$	67
3.22	Load [N] vs Displacements [mm] for $c/t = 0.1$	67
3.23	Load [N] vs Displacements [mm] for $c/t = 0.2$	68
3.24	Load [N] vs Displacements [mm] for $c/t = 0.4$	68
3.25	Load [N] vs Displacements [mm] for $c/t = 0.6$	68
3.26	Load [N] vs Displacements [mm] for $c/t = 0.8$	68
3.27	Load [N] vs Displacements [mm] for $c/t = 0.05$	68
3.28	Load [N] vs Displacements [mm] for $c/t = 0.1$	68
3.29	Load [N] vs Displacements [mm] for $c/t = 0.2$	69
3.30	Load [N] vs Displacements [mm] for $c/t = 0.4$	69
3.31	Load [N] vs Displacements [mm] for $c/t = 0.6$	69
3.32	Load [N] vs Displacements [mm] for $c/t = 0.8$	69
3.33	Stress [MPa] vs Strain [-] for $c/t = 0$	69

3.34 Stress [MPa] vs Strain [-] for $c/t = 1$.	69
3.35 Stress [MPa] vs Strain [-] for $c/t = 0.05$.	70
3.36 Stress [MPa] vs Strain [-] for $c/t = 0.1$.	70
3.37 Stress [MPa] vs Strain [-] for $c/t = 0.2$.	70
3.38 Stress [MPa] vs Strain [-] for $c/t = 0.4$.	70
3.39 Stress [MPa] vs Strain [-] for $c/t = 0.6$.	70
3.40 Stress [MPa] vs Strain [-] for $c/t = 0.8$.	70
3.41 Load-Displacement curves for C-S samples	71
3.42 Load-Displacement curves for C-I-S samples	71

Appendix

3.4 Load-Displacement curves of samples printed horizontally (along xy)

3.4.1 VeroWhite and Shore95

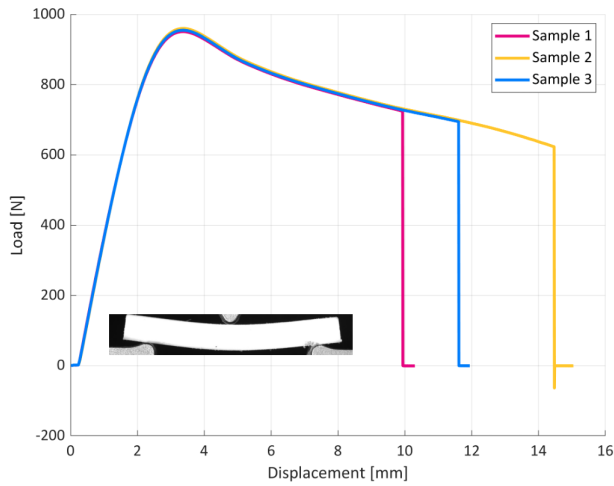


Figure 3.19 – Load [N] vs Displacements [mm] for $c/t = 0$.

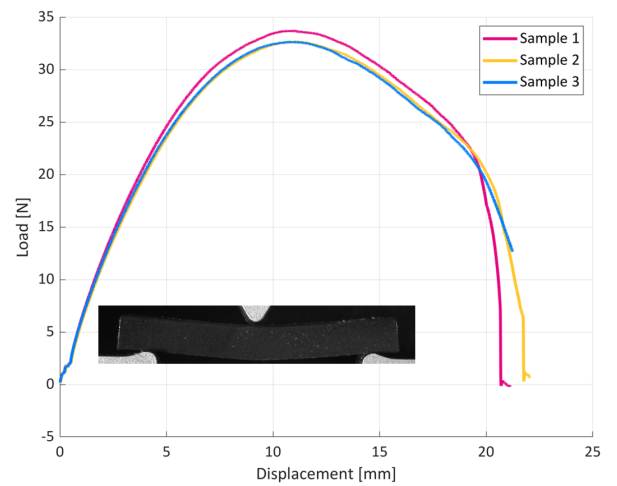


Figure 3.20 – Load [N] vs Displacements [mm] for $c/t = 1$.

3.4.2 Core-Shell configuration

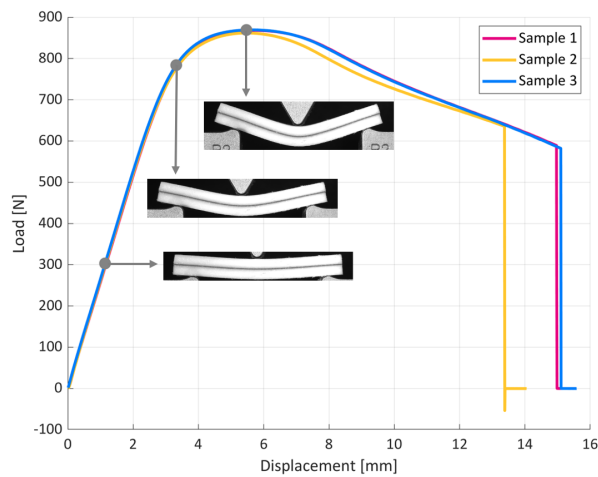


Figure 3.21 – Load [N] vs Displacements [mm] for $c/t = 0.05$.

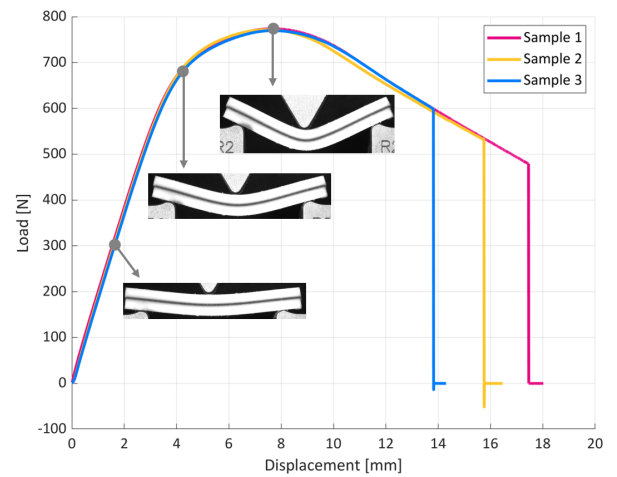


Figure 3.22 – Load [N] vs Displacements [mm] for $c/t = 0.1$.

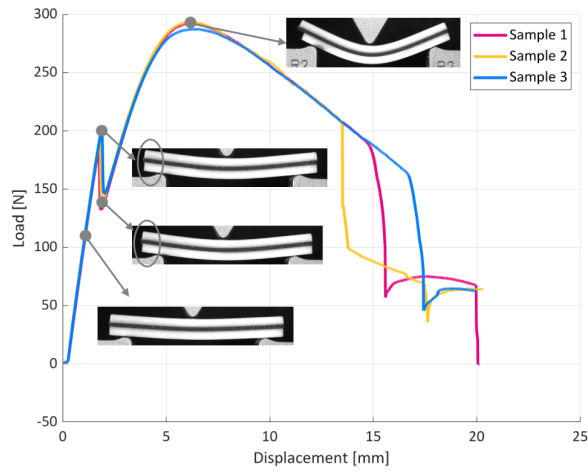


Figure 3.23 – Load [N] vs Displacements [mm] for $c/t = 0.2$.

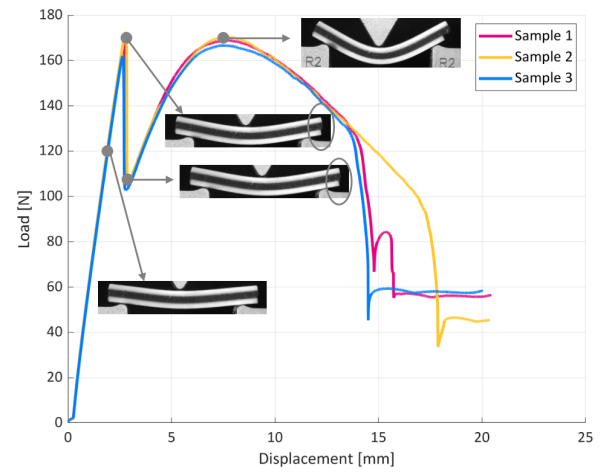


Figure 3.24 – Load [N] vs Displacements [mm] for $c/t = 0.4$.

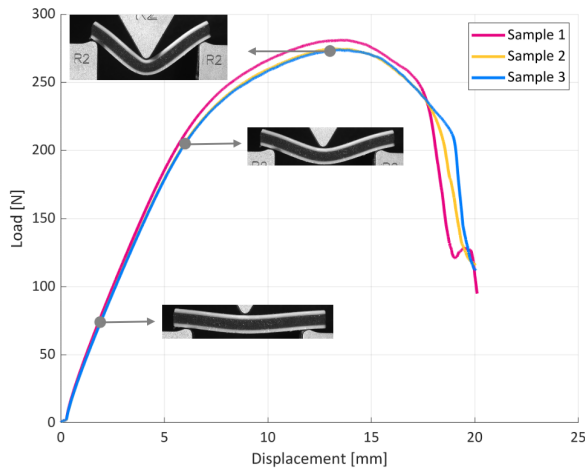


Figure 3.25 – Load [N] vs Displacements [mm] for $c/t = 0.6$.

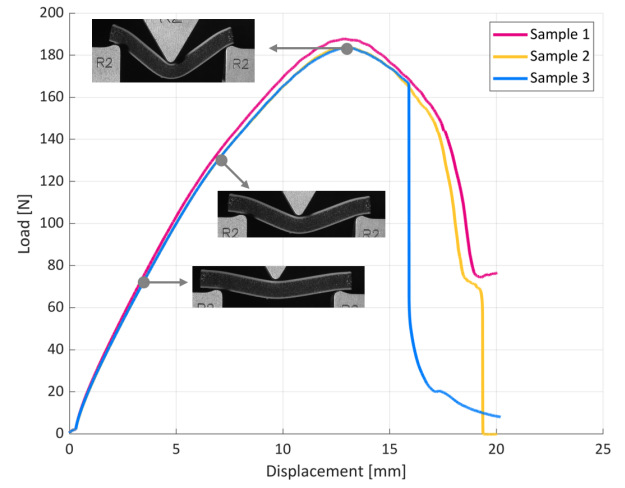


Figure 3.26 – Load [N] vs Displacements [mm] for $c/t = 0.8$.

3.5 Core - Interface - Shell configuration

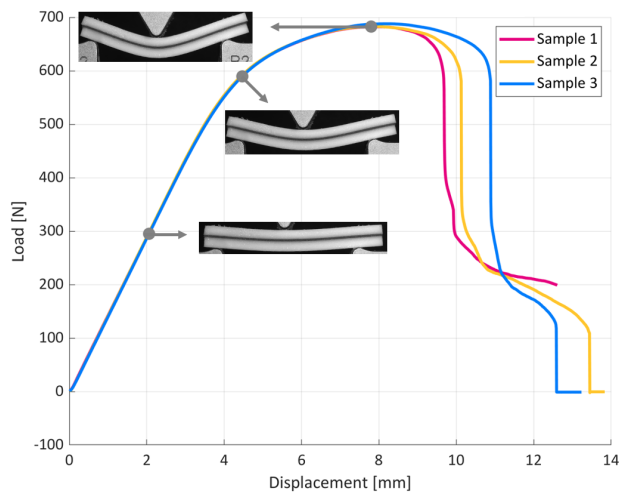


Figure 3.27 – Load [N] vs Displacements [mm] for $c/t = 0.05$.

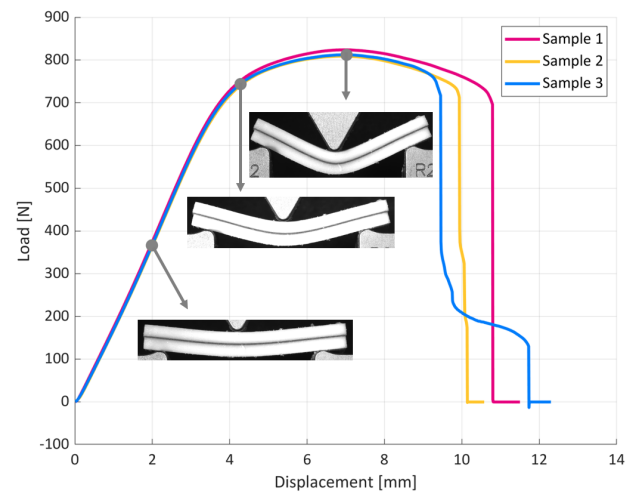


Figure 3.28 – Load [N] vs Displacements [mm] for $c/t = 0.1$.

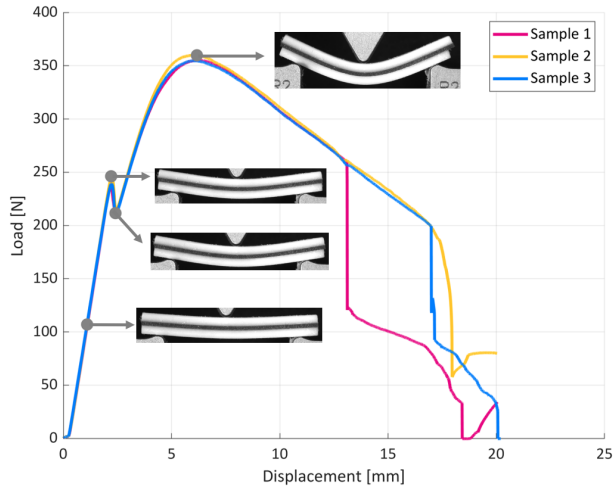


Figure 3.29 – Load [N] vs Displacements [mm] for $c/t = 0.2$.

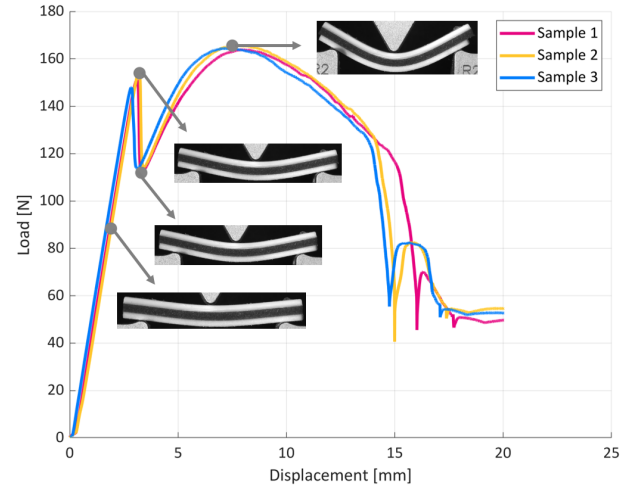


Figure 3.30 – Load [N] vs Displacements [mm] for $c/t = 0.4$.

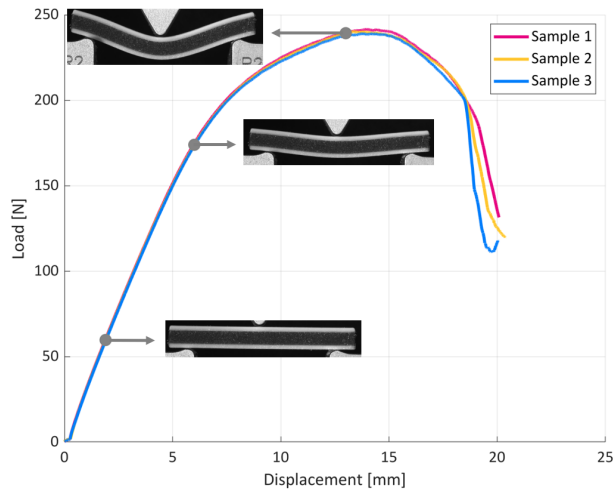


Figure 3.31 – Load [N] vs Displacements [mm] for $c/t = 0.6$.

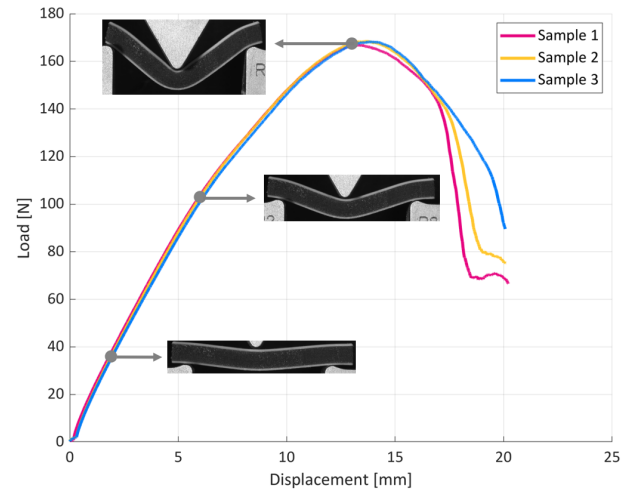


Figure 3.32 – Load [N] vs Displacements [mm] for $c/t = 0.8$.

3.6 Stress-strain curves of samples printed vertically (along xz)

3.6.1 VeroWhite and Shore95

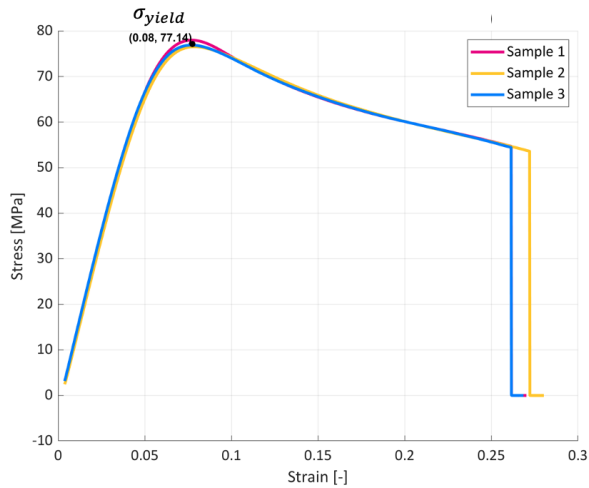


Figure 3.33 – Stress [MPa] vs Strain [-] for $c/t = 0$.

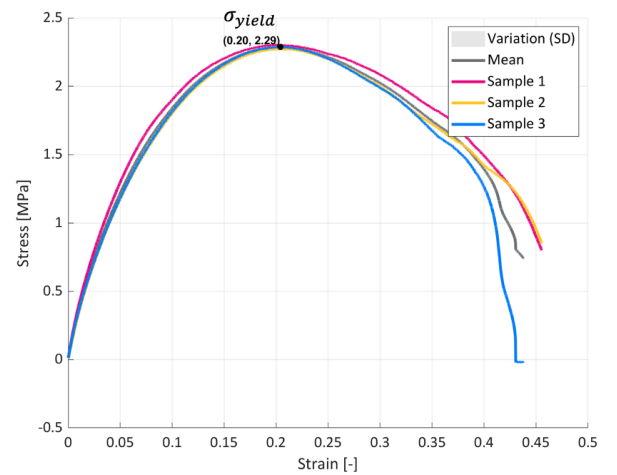


Figure 3.34 – Stress [MPa] vs Strain [-] for $c/t = 1$.

3.6.2 Core-Shell configuration

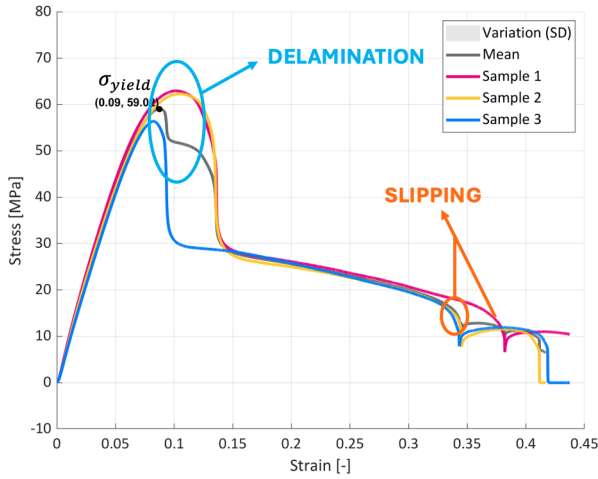


Figure 3.35 – Stress [MPa] vs Strain [-] for $c/t = 0.05$.

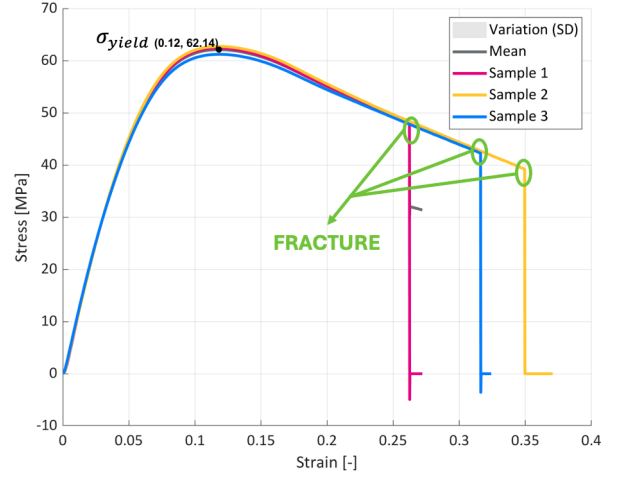


Figure 3.36 – Stress [MPa] vs Strain [-] for $c/t = 0.1$.

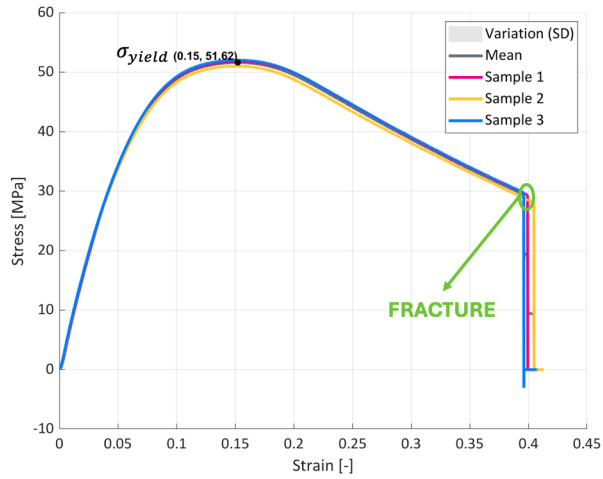


Figure 3.37 – Stress [MPa] vs Strain [-] for $c/t = 0.2$.

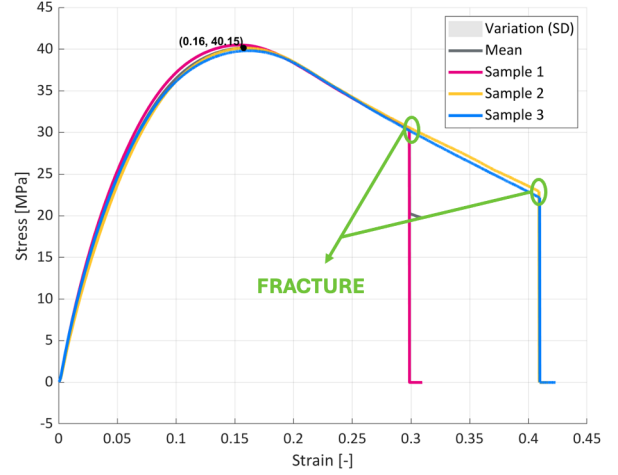


Figure 3.38 – Stress [MPa] vs Strain [-] for $c/t = 0.4$.

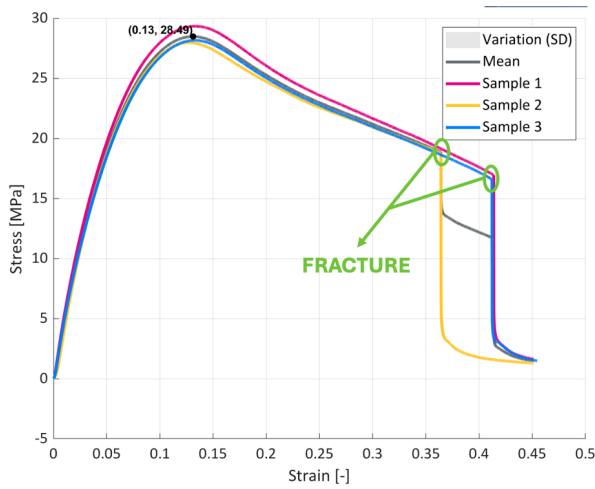


Figure 3.39 – Stress [MPa] vs Strain [-] for $c/t = 0.6$.

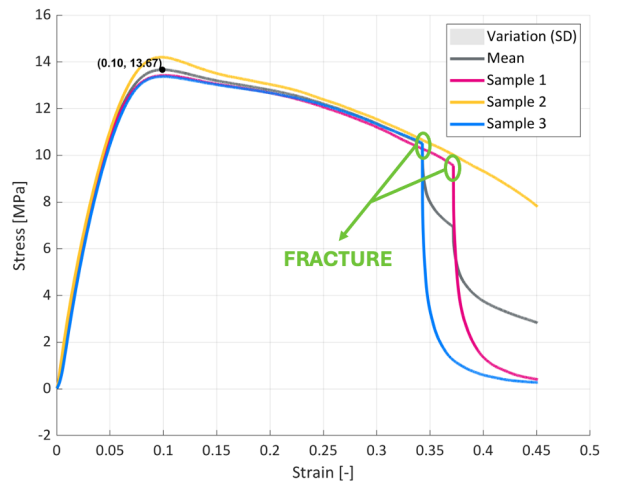


Figure 3.40 – Stress [MPa] vs Strain [-] for $c/t = 0.8$.

3.7 Load-Displacement curves with point where DIC was performed

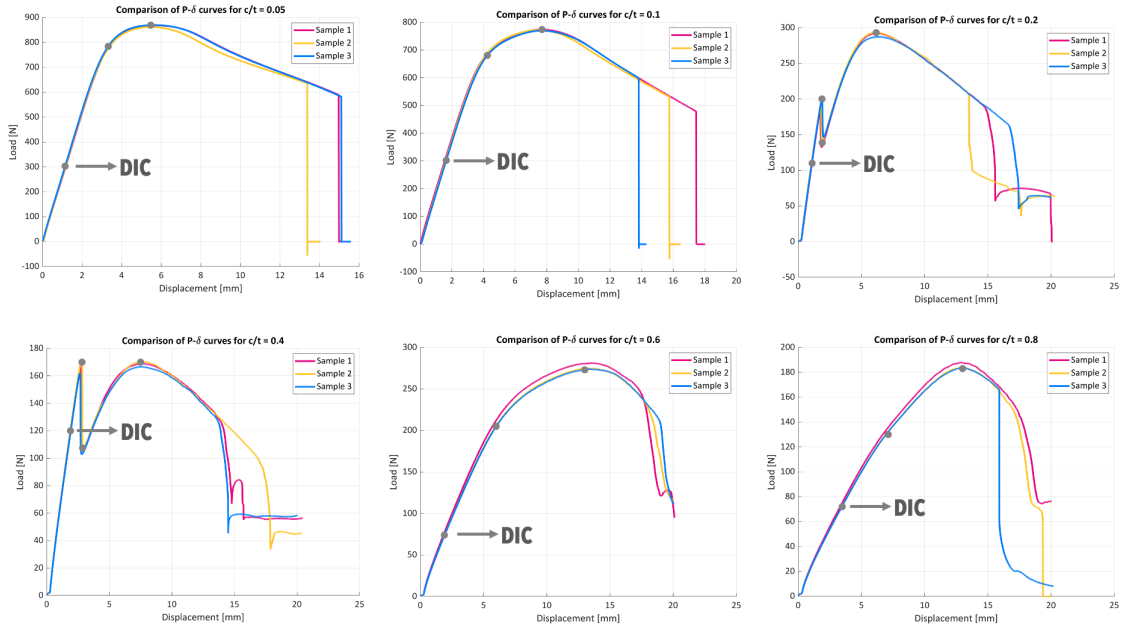


Figure 3.41 – Load-Displacement curves for C-S samples

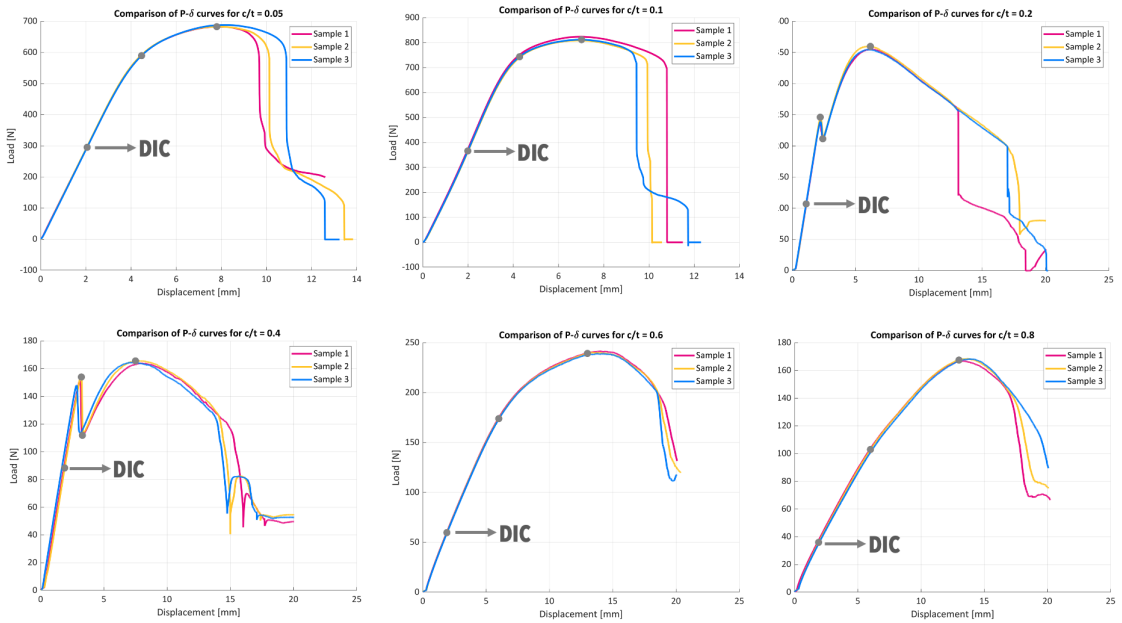


Figure 3.42 – Load-Displacement curves for C-I-S samples

3.8 MatLab Code for TPMS generation

```

%% Code to generate triple periodic structures
%% Generation of the inner core structure
clear all
clc

% Folder where I save the images
path = 'C:\Users\maureenle\Desktop';
% cd(path)

```

```

% Units for directions
c = 5;
% Number of elements for each direction
n = 401;

% Porosity value
b = 2;
% Value within which you want to accept the value as zero
delta = 0.2;
% Preparation of the matrix
ratio = 1;
M = zeros((n-1),(n-1),(n-1)*ratio);

%The cubic space is divided into as many small squares as indicated
%dimension n, for each of these the value at the point of is calculated
%coordinates 1,1,1, if the value is around zero defined as
%I(delta) then the corresponding cube is turned on, i.e. in the matrix
%M replaces the value 0 (empty) with the value 1 (full)

% Parameters to introduce anisotropy
s = 1.0;
t = 1.0;
u = 1.0;

index_tot = 1;
% image stack name
NewStack = sprintf('Tripli_%03d.tif',index_tot);

% F as to create a 0D (interstitial) defect
F = 1;

for z1 = 1:(n-1)*ratio
    for y1 = 1:(n-1)
        for x1 = 1:(n-1)
            x = s*x1;
            y = t*y1;
            z = u*z1;

            % Diamond
            %  $f(x1,y1,z1) = \cos(2\pi x^*c/n) \cos(2\pi y^*c/n) \cos(2\pi z^*c/n) - \sin(2\pi x^*c/n) \sin(2\pi y^*c/n) \sin(2\pi z^*c/n) + b$ ;

            % gyroid
            %  $f(x1,y1,z1) = \sin(2\pi x^*c/n) \cos(2\pi y^*c/n) + \sin(2\pi y^*c/n) \cos(2\pi z^*c/n) + \sin(2\pi z^*c/n) \cos(2\pi x^*c/n) + b$ ;

            % IWP
             $f(x1,y1,z1) = 2\cos(2\pi x^*c/n) \cos(2\pi y^*c/n) + 2\cos(2\pi y^*c/n) \cos(2\pi z^*c/n) + 2\cos(2\pi x^*c/n) \cos(2\pi z^*c/n) - \cos(4\pi x^*c/n) - \cos(4\pi y^*c/n) - \cos(4\pi z^*c/n)$ 

```

```

        /n) + b;

    if f(x1,y1,z1) < delta && f(x1,y1,z1) > (-1*delta)
        M(x1,y1,z1) = 1;
        M_q(x1,y1) = M(x1,y1,z1);
    else
        M(x1,y1,z1) = 0;
        M_q(x1,y1) = M(x1,y1,z1);
    end
end
end
end

porosity = 1-sum(sum(sum(M)))/size(M,1)^3;

%% Generation of the outer shell structure
se = ones(3, 3, 3);
loop = 15;
D1 = M;
for ii = 1:loop
    D1 = imdilate(D1,se);
end
E1 = D1 - M;

porosity_2 = 1-sum(sum(sum(D1)))/size(D1,1)^3;
porosity_3 = 1-sum(sum(sum(E1)))/size(E1,1)^3;

%% Saving the structure in a .tiff file

% in this loop I write the image stacks
% clear tripliC
% tripliC = scaffold;
% AA = uint8(double(tripliC.*255));

scaffold = uint8(double(D1.*255));
file_name = 'IWP_5_400_D1.tif';

for k = 1:size(scaffold,3)
    imwrite(uint8(scaffold(:, :, k)), file_name, 'WriteMode','append');
end

```

Bibliography

- [1] L.J. Gibson and M.F. Ashby. "Cellular solids: Structure and properties - Second edition." *Cambridge: Cambridge University Press*, 1997. <https://doi.org/10.1017/CB09781139878326>
- [2] K.M. Park, K.S. Min and Y.S. Roh. "Design Optimization of Lattice Structures under Compression: Study of Unit Cell Types and Cell Arrangements." *Materials*, 15: 97, 2022. <https://doi.org/10.3390/ma15010097>
- [3] F.W. Zok, H. Rathbun, M. He, E. Ferri, C. Mercer, R.M. McMeeking and A.G. Evans. "Structural performance of metallic sandwich panels with square honeycomb cores." *Philosophical Magazine*, 85(26–27):3207–3234, 2005. <https://doi.org/10.1080/14786430500073945>
- [4] C.I. Hammetter, R.G. Rinaldi, F.W. Zok. "Pyramidal Lattice Structures for High Strength and Energy Absorption." *ASME. J. Appl. Mech.*, 80(4):041015, 2013. <https://doi.org/10.1115/1.4007865>
- [5] Council NR. NASA space technology roadmaps and priorities: restoring NASA's technological edge and paving the way for a new era in space. 2012.
- [6] J. Tarpani and A. Portela. "Magnetic resonance imaging of contaminated and damaged core cells in polymer composite sandwich panels." *Journal of Sandwich Structures and Materials*, 20, 2017.
- [7] T. Decker and S. Kedziora. "Optimizing the Thickness of Functionally Graded Lattice Structures for High-Performance Energy Absorption: A Case Study Based on a Bicycle Helmet." *Appl. Sci.*, 14: 2788, 2024. <https://doi.org/10.3390/app14072788>
- [8] S. Gilakara. "Structural Optimization of Automobile Bumper Using Honeycomb Structure.", 2018.
- [9] N. A. Fleck, V. S. Deshpande and M. F. Ashby. "Micro-architected materials: past, present and future". *Proc. R. Soc. A.*, 466:2495–2516, 2010. <https://doi.org/10.1098/rspa.2010.0215>
- [10] M. Zhao, F. Liu, G. Fu, D.Z. Zhang, T. and H. Zhou. "Improved Mechanical Properties and Energy Absorption of BCC Lattice Structures with Triply Periodic Minimal Surfaces Fabricated by SLM." *Materials*, 11: 2411, 2018. <https://doi.org/10.3390/ma11122411>
- [11] L.R. Meza, S. Das and J.R. Greer. "Strong, lightweight, and recoverable three-dimensional ceramic nanolattices." *Science*, 345(6202):1322 -1326, 2014. DOI:10.1126/science.1255908
- [12] B.G. Compton and J A. Lewis. "3D-printing of lightweight cellular composites." *Adv Mater.*, 26(34):5930-5, 2014. doi:10.1002/adma.201401804
- [13] E.B. Duoss, T.H. Weisgraber, K. Hearon, C. Zhu, W. Small, T.R. Metz, J.J. Vericella, H.D. Barth, J.D. Kuntz and R.S. Maxwell. "Three-Dimensional Printing of Elastomeric, Cellular Architectures with Negative Stiffness." *Adv. Funct. Mater.*, 24(31): 4905-4913, 2014. <https://doi.org/10.1002/adfm.201400451>
- [14] R. Ritchie. "The conflicts between strength and toughness." *Nature Mater*, 10:817–822, 2011. <https://doi.org/10.1038/nmat3115>
- [15] "What's the difference between stiff, strong, and tough?" (n.d.). <https://blog.cambridgecoaching.com/whats-the-difference-between-stiff-strong-and-tough>

- [16] M. Williams, M. "Materials theory combines strength, stiffness and toughness of composites into a single design map." *Phys. Org.*, 2015. <https://phys.org/news/2015-03-materials-theory-combines-strength-stiffness.html>
- [17] Y. Jiang and Q. Wang. "Highly-stretchable 3D-architected mechanical metamaterials." *Sci. Rep.*, 6(1): 1-11, 2016. <https://doi.org/10.1038/srep34147>
- [18] N.S. Ha and G. Lu. "A review of recent research on bio-inspired structures and materials for energy absorption applications." *Compos. Part B Eng.*, 181:107496, 2020. <https://doi.org/10.1016/j.compositesb.2019.107496>
- [19] Y. Wei, Q. Yang, X. Liu and R. Tao. "Multi-bionic mechanical metamaterials: A composite of FCC lattice and bone structures." *International Journal of Mechanical Sciences*, 213: 106857, 2022. <https://doi.org/10.1016/j.ijmecsci.2021.106857>
- [20] R.Z. Wang and H.S. Gupta. "Deformation and fracture mechanisms of bone and nacre." *Annu. Rev. Mater. Res.*, 41:41–73, 2011. <https://doi.org/10.1146/annurev-matsci-062910-095806>
- [21] A.G. Evans, Z. Suo, R.Z. Wang, I.A. Aksay, M.Y. He and J.W. Hutchinson. "Model for the robust mechanical behavior of nacre." *Journal of Materials Research*, 16:2475–2484, 2001. <https://doi.org/10.1557/JMR.2001.0339>
- [22] A.P. Jackson, F.V. Vincent and R. M. Turner. "The mechanical design of nacre." *Proc. R. Soc. Lond. B.*, 234(1277): 415–440, 1988. <http://doi.org/10.1098/rspb.1988.0056>
- [23] K. Chen, B. Shi, Y. Yue, J. Qi and L. Guo. "Binary Synergy Strengthening and Toughening of Bio-Inspired Nacre-like Graphene Oxide/Sodium Alginate Composite Paper." *ACS Nano*, 9(8):8165–8175, 2015. <https://doi.org/10.1021/acs.nano.5b02333>
- [24] U.G. Wegst, H. Bai, E. Saiz, A.P. Tomsia and R.O. Ritchie. "Bioinspired structural materials." *Nat. Mater.*, 12:23-36, 2015. <https://doi.org/10.1038/nmat4089>
- [25] F. Libonati, G.X. Gu, Z. Qin, L. Vergani and M.J. Buehler. "Bone-Inspired Materials by Design: Toughness Amplification Observed Using 3D Printing and Testing." *Advanced Engineering Materials*, 18(8):1354-1363, 2016. [doi:10.1002/adem.201600143](https://doi.org/10.1002/adem.201600143)
- [26] K. Tai, M. Dao, S. Suresh, A. Palazoglu and C. Ortiz. "Nanoscale heterogeneity promotes energy dissipation in bone." *Nat. Mater.*, 6(6):454-62, 2007. [doi:10.1038/nmat1911](https://doi.org/10.1038/nmat1911)
- [27] Z. Hu, K. Thiagarajan, A. Bhusal, T. Letcher, Q. Fan, Q. Liu and D. Salem. "Design of ultralightweight and high-strength cellular structural composites inspired by biomimetics." *Composites Part B*, 121:108-12, 2017. <http://dx.doi.org/10.1016/j.compositesb.2017.03.033>
- [28] J. Mueller, J.R. Raney, K. Shea and J.A. Lewis. "Architected lattices with high stiffness and toughness via multicore-shell 3D printing." *Adv. Mat.*, 30(12):1705001, 2018. <https://doi.org/10.1002/adma.201705001>
- [29] D. Yavas, Q. Liu, Z. Zhang and D. Wu. "Design and fabrication of architected multi-material lattices with tunable stiffness, strength, and energy absorption." *Materials and Design*, 217:110613, 2022. <https://doi.org/10.1016/j.matdes.2022.110613>
- [30] M.F. Ashby. "Materials Selection in Mechanical Design (5th edition)." *Butterworth-Heinemann*, 2011.
- [31] T.D. Ngo, A. Kashani, G. Imbalzano, K.T. Nguyen and D. Hui. "Additive manufacturing (3D printing): a review of materials, methods, applications and challenges." *Compos. Part B: Eng.*, 143: 172–196, 2018. <https://doi.org/10.1016/j.compositesb.2018.02.012>
- [32] F. Liu, T. Li, X. Jiang, Z. Jia, Z. Xu and L. Wang. "The effect of material mixing on interfacial stiffness and strength of multi-material additive manufacturing." *Additive Manufacturing*, 36: 101502, 2020. <https://doi.org/10.1016/j.addma.2020.101502>

- [33] A. Bandyopadhyay and B. Heer."Additive manufacturing of multi-material structures." *Material Science & Engineering*, 129: 1-16, 2018.<https://doi.org/10.1016/j.mser.2018.04.001>
- [34] 3DSourced."Material Jetting (PolyJet) 3D Printing: Everything You Need To Know", 2020. <https://www.3dsourced.com/guides/polyjet/>
- [35] Stratasys."PolyJet technology", 2018. <http://www.stratasys.com/de/polyjet-technology>
- [36] J. Mueller, K. Shea and C."Daraio. Mechanical properties of parts fabricated with inkjet 3D printing through efficient experimental design." *Materials and Design*, 86: 902–912, 2015. <https://doi.org/10.1016/j.mtcomm.2018.08.013>
- [37] F.I. Ulu, R.T.S. Tomar and R.V. Mohan."Investigation of digital CAD assembly and tessellation effects on digital ABS part quality in PolyJet 3D additive printing." *SAMPE Technical Conference*, Long Beach, CA, p.16, 2018.
- [38] Stratasys.VeroVivid Material Safety Data Sheet (MSDS), <https://www.stratasys.com/siteassets/materials/materials-catalog/polyjet-materials/verovivid/>
- [39] Stratasys.Tango Material Safety Data Sheet (MSDS), <https://www.stratasys.com/siteassets/materials/materials-catalog/polyjet-materials/tango/>
- [40] J. Hiller and H. Lipson. "Tunable digital material properties for 3D voxel printers." *Rapid Prototyping Journal*, 16(4): 241-247, 2010. DOI10.1108/13552541011049252
- [41] F. Liu, T. Li, X. Jiang, Z. Jia, Z. Xu and L. Wang. "The effect of material mixing on interfacial stiffness and strength of multi-material additive manufacturing." *Additive Manufacturing*, 36: 101502, 2020.<https://doi.org/10.1016/j.addma.2020.101502>
- [42] T.S. Lumpe, J. Mueller and K. Shea."Tensile properties of multi-material interfaces in 3D printed part." *Materials and Design*, 162: 1-9, 2019. <https://doi.org/10.1016/j.matdes.2018.11.024>
- [43] J.P. Moore and C.B. Williams."Fatigue properties of parts printed by PolyJet material jetting." *Rapid Prototyp. J.*, 21: 675-685, 2015. <https://doi.org/10.1108/Rpj-03-2014-0031>
- [44] J. Mueller, D. Courty, M. Spielhofer, R. Spolenak and K. Shea. "Mechanical properties of interfaces in inkjet 3D printed single- and multi-material parts, 3D Print." *Addit. Manuf.*, 4: 193–199, 2017. <https://doi.org/10.1089/3dp.2017.0038>
- [45] F.P. Melchels, A.M. Barradas, C.A. van Blitterswijk, J. de Boer, J. Feijen and D.W. Grijpma. "Effects of the architecture of tissue engineering scaffolds on cell seeding and culturing." *Acta Biomater.*, 6(11):4208-17, 2010. <https://doi.org/10.1016/j.actbio.2010.06.012>
- [46] U. Ripamonti, L.C. Roden and L.F. Renton. "Osteoinductive hydroxyapatite-coated titanium implants.", *Biomaterials*, 33(15): 3813-3823, 2012.<https://doi.org/10.1016/j.biomaterials.2012.01.050>
- [47] S.S. Lee, X. Du, I. Kim and S.J. Ferguson. "Scaffolds for bone-tissue engineering.", *Matter*, 5: 2722-2759, 2022.
- [48] T. Ghassemi, A. Shahroodi, M.H.Ebrahimzadeh, A. Mousavian, J. Movaffagh and A. Moradi. "Current Concepts in Scaffolding for Bone Tissue Engineering." *Arch Bone Jt Surg*, 6(2): 90-99, 2018.
- [49] P.F. Egan."Integrated Design Approaches for 3D Printed Tissue Scaffolds: Review and Outlook." *Materials*, 12: 2355, 2019. <https://doi.org/10.3390/ma12152355>
- [50] K.J. Burg, S. Porter and J.F. Kellam."Biomaterial developments for bone tissue engineering." *Biomaterials*, 21(3):2347-2359, 2000. [https://doi.org/10.1016/S0142-9612\(00\)00102-2](https://doi.org/10.1016/S0142-9612(00)00102-2)
- [51] M. Wang. "Developing bioactive composite materials for tissue replacement." *Biomaterials*, 24(13): 2133-2151, 2003. [https://doi.org/10.1016/S0142-9612\(03\)00037-1](https://doi.org/10.1016/S0142-9612(03)00037-1)

- [52] J. Feng, J. Fu, X. Yao and Y. He. "Triply periodic minimal surface (TPMS) porous structures: from multi-scale design, precise additive manufacturing to multidisciplinary applications." *Int. J. Manuf.*, 4, 2022. <https://doi.org/10.1088/2631-7990/ac5be6>
- [53] Z. Dong and X. Zhao. "Application of TPMS structure in bone regeneration." *Engineered Regeneration*, 2: 154-162, 2021. <https://doi.org/10.1016/j.engreg.2021.09.004>
- [54] F. Liu, Q. Ran, M. Zhao, T. Zhang, D.Z. Zhang and Z. Su. "Additively Manufactured Continuous Cell-Size Gradient Porous Scaffolds: Pore Characteristics, Mechanical Properties and Biological Responses In Vitro." *Materials (Basel)*, 13(11): 2589, 2020 <https://doi.org/10.3390/ma13112589>
- [55] M. Elsheikh, R. Kishida, K. Hayashi, A. Tsuchiya, M. Shimabukuro and K. Ishikawa. "Effects of pore interconnectivity on bone regeneration in carbonate apatite blocks." *Regen Biomater.*, 9(1), 2022. <https://doi.org/10.1093/rb/rbac010>
- [56] P. Xia and Y. "Luo. Vascularization in tissue engineering: The architecture cues of pores in scaffolds." *J Biomed Mater Res B Appl Biomater.*, 110(5):1206-1214, 2022. <https://doi.org/10.1002/jbm.b.34979>
- [57] E.M.Sanchez. "Superficies minimales. Historia, desarrollo y aplicaciones a otras ciencias" *Universidad Complutense de Madrid*, 2015.
- [58] B. Hanks, J. Berthel, M. Frecker and T. W. Simpson. "Mechanical properties of additively manufactured metal lattice structures: Data review and design interface." *Additive Manufacturing*, 35: 101301, 2020. <https://doi.org/10.1016/j.addma.2020.101301>
- [59] D. W. Abueidda, R.K. Abu Al-Rub, A.S. Dalaq, D. Lee, K.A. Khan and I. Iwona. "Effective conductivities and elastic moduli of novel foams with triply periodic minimal surfaces." *Mechanics of Materials*, 95: 102-115, 2016. <https://doi.org/10.1016/j.mechmat.2016.01.004>
- [60] S.N. Khaderi, V.S. Deshpande and N.A. Fleck. "The stiffness and strength of the gyroid lattice." *International Journal of Solids and Structures*, 51(23-24): 3866-3877, 2014. <https://doi.org/10.1016/j.ijsolstr.2014.06.024>
- [61] Z Liu, M. Tamaddon, S.M. Chen, H. Wang, V. San Cheong, F. Gang, X. Sun and C. Liu. "Determination of an Initial Stage of the Bone Tissue Ingrowth Into Titanium Matrix by Cell Adhesion Model." *Front Bioeng Biotechnol*, 9:736063, 2021. <https://doi.org/10.3389/fbioe.2021.736063>
- [62] J. Santos J, T. Pires, B.P. Gouveia, et al. "On the permeability of TPMS scaffolds." *J Mech Behav Biomed Mater*, 110:103932, 2020 [doi:10.1016/j.jmbbm.2020.103932](https://doi.org/10.1016/j.jmbbm.2020.103932)
- [63] A. Diez-Escudero, H. Harlin, P. Isaksson P, et al. "Porous polylactic acid scaffolds for bone regeneration: A study of additively manufactured triply periodic minimal surfaces and their osteogenic potential." *J Tissue Eng*, 11, 2020. [doi:10.1177/2041731420956541](https://doi.org/10.1177/2041731420956541)
- [64] N. Kladovasilakis, K. Tsongas, I. Kostavelis, et al. "Effective mechanical properties of additive manufactured triply periodic minimal surfaces: Experimental and finite element study." *Int J Adv Manuf Technol*, 121:7169–7189, 2022. [doi:10.1007/s00170-022-09651-w](https://doi.org/10.1007/s00170-022-09651-w)
- [65] I. Maskery, L. Sturm, A.O. Aremu, et al. "Insights into the mechanical properties of several triply periodic minimal surface lattice structures made by polymer additive manufacturing." *Polymer*, 152:62–71, 2018. [doi:10.1016/j.polymer.2017.11.049](https://doi.org/10.1016/j.polymer.2017.11.049)
- [66] A.P.G. Castro, J. Santos, T. Pires, et al. "Micromechanical behavior of TPMS scaffolds for bone tissue engineering." *Macromol Mater Eng*, 305:2000487, 2020. [doi:10.1002/mame.202000487](https://doi.org/10.1002/mame.202000487)
- [67] X. Pei, L. Wu, C. Zhou, et al. "3D printed titanium scaffolds with homogeneous diamond-like structures mimicking that of the osteocyte microenvironment and its bone regeneration study." *Biofabrication*, 13:015008, 2021. [doi:10.1088/1758-5090/abc060](https://doi.org/10.1088/1758-5090/abc060)

- [68] L. Zorzetto, L. Andena, F. Briatico-Vangosa et al. " Properties and role of interfaces in multimaterial 3D printed composites." *Sci Rep*, 10:22285, 2020. <https://doi.org/10.1038/s41598-020-79230-0>
- [69] J. Blaber and A. Antoniou. "Instruction Manual." *Ncorr*, version 1.2.2, 2017.
- [70] J. Blaber, A. Antoniou. and B. Adair. " Ncorr: Open-Source 2D Digital Image Correlation Matlab Software." *Experimental Mechanics*, 2015. DOI10.1007/s11340-015-0009-1
- [71] R. Harilal and M. Ramji."Adaptation of Open Source 2D DIC Software Ncorr for Solid Mechanics Applications." *9th International Symposium on Advanced Science and Technology in Experimental Mechanics*, 2014.
- [72] Digitalimagecorrelation.org. digitalimagecorrelation.org. (n.d.). <https://digitalimagecorrelation.org/>
- [73] S. Restrepo et al."Mechanical properties of ceramic structures based on Triply Periodic Minimal Surface (TMPS) processed by 3D printing." *J. Phys.: Conf. Ser.*, 935: 012036, 2017. doi:10.1088/1742-6596/935/1/012036.
- [74] S. Ibrahimi, L. D’Andrea; D. Gastaldi, M.W. Rivolta and P. Vena. "Machine Learning approaches for the design of biomechanically compatible bone tissue engineering scaffolds." *Computer Methods in Applied Mechanics and Engineering*, 423: 116842, 2024. <https://doi.org/10.1038/s41598-020-79230-0>